Fabrication of two-dimensional materials/polyimide composites by covalent bonding strategies

共有結合による２次元材料／ポリイミド複合材料の創出

March 2024

CHENG YIKAI

The Graduate School of Natural Science and Technology

(Doctor Course)

Okayama University

GENERAL INTRODUCTION

With the rapid advancement of technology, the demand for materials with exceptional chemical and physical properties such as mechanical strength, thermal conductivity, electrical conductivity, and low dielectric constant has increased significantly. Polyimide (PI) possesses several favourable characteristics, making it an indispensable material in electronic products. However, with the rapid development of wearable electronic products and battery technology in recent years, the performance and application of PI gradually fail to meet the needs of products. In order to enhance the performance and applicability of PI, adding materials with good physical properties to PI to form a composite material is a very potential choice. However, the requirements for the additive material of PI are extremely stringent, such as the dispersion of the filler material in the PI, the size of the material, and the amount of additive, etc. If the filler material is not well matched, the PI will not be suitable for the application. Failure to match these requirements will result in a decline in the physical properties of the composite material or cause unavoidable defects. Conventional filler materials such as carbon black, fullerene, and carbon nanotubes are known to be effective in enhancing the physical properties of PI composites. However, due to the performance and structural problems of the filler materials, the desired properties and applications could not be achieved.

In 2004, A. Geim and K. Novoselov first obtained monolayer graphene through mechanical exfoliation, overturning thermodynamically unstable theories. This discovery, which won the Nobel Prize in Physics in 2010, marked the beginning of an era exploring two-dimensional materials. Since then, various two-dimensional (2D) materials such as boron nitride (BN), transition metal dichalcogenides (TMDS), molybdenum disulfide (MOS_2), and MXenes. Quaternary materials have special structure and excellent physical properties, such as excellent mechanical properties, thermal conductivity, electrical conductivity and electronic transfer. In this context, 2D materials have great

potential to enhance the chemical and physical properties of PI composites and to expand their applications.

This thesis is divided into two parts. The first part summarizes the information about the properties of graphene and boron nitride, the synthesis routes, and the fabrication and application of PI composites. The second part describes in detail the experimental studies conducted.

The first part introduces the various synthesis routes of graphene and boron nitride. At the same time, PI synthesis, characterization and applications are discussed, and the applications and future of PI composites with the addition of 2D material are introduced.

The second part describes the scientific progress achieved through this blog paper; the first part introduces the fabrication of complex 2D materials with PI composite films; the second part introduces the results of controlling the functional total amount of h-BN on PI composite films; the last part introduces the PI nanowalls grown on GO surfaces to form tertiary carbonaceous materials by heating, and unlocks the excellent properties of LIBs.

The third part presents the conclusion and future prospects.

Chapter 1 focuses on a comprehensive literature review of graphene and h-BN. The synthesis methods of graphene and h-BN are introduced: mechanical exfoliation, ultrasonic exfoliation, oxidative reduction, and chemical vapor deposition.

Chapter 2 presents a comprehensive literature review on polyimide. Such as, the synthesis, characterization and application. Then, based on the shortcomings of PI properties, the addition of 2D materials is used to further enhance the physical properties of PI and to expand the applications.

Chapter 3 introduces the effect of complex 2D- materials on the mechanical properties of PI. The 2D material are GO and h-BN, which are effectively dispersed in organic solvents, chemically modified by ball milling method, and then added with a certain proportion of GO, which are mixed to produce PI composite films with good mechanical properties. This study can provide a better development for the future application of PI composite films for plural-quadratic material interactions.

Chapter 4, the total number of functional groups by controlling the h-BN surface is presented. A list of their properties such as crystallinity, total number of functional groups is given. In this experiment, we control the total amount of functional groups on h-BN surface by ball milling method and get the agreement with the actual ball milling result by using mathematical simulation. Then, we formed a composite film with PI and analyzed its properties. The effect of the total amount of functional groups on the mechanical properties of the composite film is investigated.

Chapter 5, the three-dimensional nanocarbon structure of PI and GO was fabricated by simple fabrication, and this structure was utilized to have good performance in lithium-ion batteries. In this study, we grew PI nanowalls structures vertically on the surface of graphene oxide, and fabricated different 3D nanocarbon material through different reaction times and heating temperatures. The prepared 3D nanocarbon material were applied to lithium-ion batteries and showed excellent performance.

Chapter 6 presents the conclusion and future prospects.

Chapters 7 and 8 present the list of publication and acknowledgement.

Contents

CHAPTER 1
Current progress of two-dimensional (2D) materials

I. INTRODUCTION

I.1 2D materials

In 2004, scientists in Manchester successfully isolated single-layer graphene from graphite using a repeated tape exfoliation method, demonstrating the existence of stable single-layer graphene. Its unique structure and excellent physical properties sparked a wave of graphene research,[1] which caused A.K. Geim and K.S. Novoselov to be awarded the Nobel Prize in Physics in 2010 for their groundbreaking discoveries in the field.

Since then, researchers have discovered other 2D materials different from graphene,[1,2] such as transition metal dichalcogenides (TMDCs),[3,4] magnetic 2D materials,[5–7] MXenes,[8,9] hexagonal boron nitride (h-BN),[10,11] etc. The special structure of 2D materials contributes to their excellent thermal, electrical, and mechanical properties. For example, they possess ultrahigh theoretical specific surface area, electrical and thermal conductivities, and directional mechanical properties.[12–15] These materials hold great potential for applications in water filtration membranes,[16–18] nanocomposites,[19–21] energy storage device electrodes,[22–24] and semiconductors.[25–28] However, the difficulties encountered for large-scale production of 2D materials hinders their widespread application in everyday products.[29,30]

The inherent attractiveness of 2D materials has led scientists to further explore their physical properties by incorporating them into other materials. In particular, the addition of small amounts of 2D materials to polymers has shown significant improvements in their physical properties, including mechanical properties, thermal conductivity, electrical conductivity, and hydrophobicity. [29–32] These results highlight the enormous potential of composite materials obtained by combining 2D materials and polymers. However, there are several difficulties when producing these materials, especially related to the difficulty to achieve homogeneous dispersions of 2D materials in organic solvents, as it is the poor dispersion the materials exhibit which leads to defects in the material structure and the subsequent deterioration of the physical properties of polymer composites. To effectively improve the dispersion of 2D materials in organic solvents, surface functionalization is performed. Furthermore,

scientists have discovered that specific functionalization on the surface of 2D materials helps to establish stronger connections between 2D materials and polymers, thereby enhancing the physical properties of polymer composites.[33–35] However, surface modification of 2D materials alone is not sufficient, as their dispersion in polymer composites tends to be random. To introduce anisotropic dispersion of 2D materials in polymer composites, functionalization is carried out around the 2D materials, ensuring their uniform dispersion in a specific direction within the polymer composite.[33–35] This can help to elucidate the mechanism in which 2D materials are able to modify the physical properties of polymers through different functionalization approaches, effectively creating polymer composites tailored to specific functionalities that can adapt the materials for diverse applications.

I.2 Graphene

Graphene is a 2D material with a planar structure composed of a single layer of carbon atoms. Prior to the discovery of graphene, it was generally believed that 2D crystal structures would only exist in absolute zero temperatures according to the thermodynamic theory. However, in 2004, a research team of scientists in Manchester successfully isolated graphene from graphite using a simple method known as the "scotch tape" technique.[1,2] The discovery of single-layer graphene overturned many previously held notions in physics and demonstrated that graphene possesses a 2D honeycomb lattice structure with sp^2 covalent bonds (Fig 1).

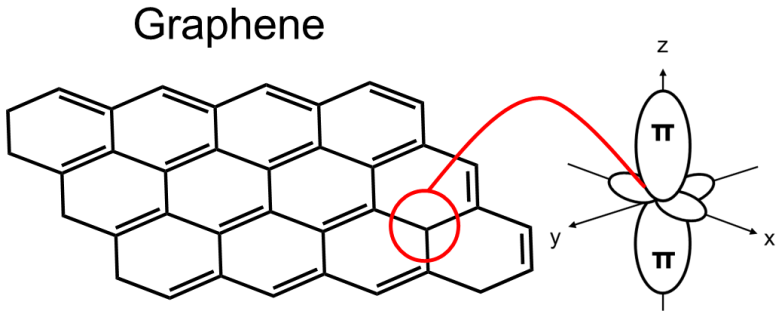

Fig. 1 Structure of graphene showing the sp2 carbon atoms bounded in hexagonal rings.

The carbon-carbon bond length in graphene is typically 1.42 Å, and the connections between individual carbon atoms are exceptionally strong, making it one of the toughest materials known

(Tensile strength and Young's modulus of approximately 130 GPa and 1 TPa, respectively).[36–38] Additionally, graphene exhibits a highly stable crystalline structure and possesses excellent thermal conductivity (~4000 $Wm^{-1} K^{-1}$).[39–41] The thickness of a single layer of graphene is approximately 0.34 nm,[42,43] resulting in an extremely high theoretical surface area of 2630 $m^2 g^{-1}$.[43] Due to the presence of delocalized π electrons along the Z-axis of graphene, electronic motion within its orbitals is not affected by lattice defects or impurities, leading to its exceptionally high intrinsic mobility (200000 $cm^2 v^{-1} s^{-1}$)[44,45] and conductivity (approximately 200000 S/cm).[46–48] Moreover, graphene can give rise to allotropes through structural variations, such as fullerenes, carbon nanotubes, and graphite (Figure 2).[49]

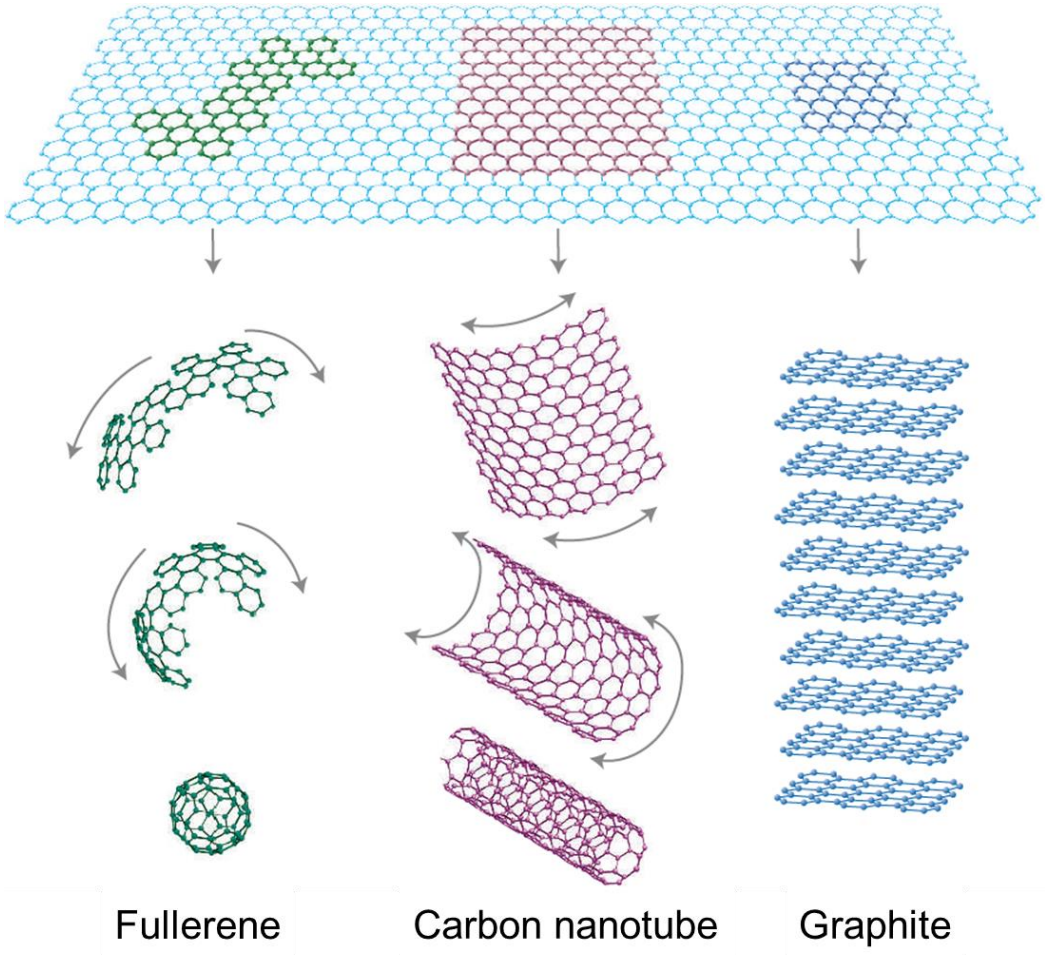

Fig. 2 Graphene is a 2D building material for carbon materials of all other dimensionalities. It can be wrapped up into 0D fullerene, rolled into 1D nanotubes or stacked as in 3D graphite found in nature Reprinted with permission from Science.[49]

Due to the extremely high theoretical surface area of graphene, its surface functional groups can be easily modified by chemical modification, which is helpful for its successful dispersion in organic solvents. The application of modified graphene to the preparation of polymer nanocomposites can effectively improve the mechanical properties, electrical conductivity, and thermal conductivity of polymer materials.[33–35]

I.2.1 Synthesis of graphene

Typically, graphene fabrication methods can be broadly classified into two categories: "bottom-up" and "top-down" approaches, which encompass both physical and chemical preparation methods. The top-down approach involves the exfoliation or delamination of graphite, and commonly employed techniques consist in oxidation-reduction methods,[50,51] electrochemical reduction methods,[52,53] ultrasonic exfoliation.[54,55] The bottom-up approach involves the rearrangement of carbon-hydrogen compounds or aromatic compounds, such as chemical vapor deposition and epitaxy.[56] Selection of the synthesis method can influence the properties and applications of the resulting graphene materials, including their crystallinity, conductivity, surface characteristics, and physical properties.[44–46,49]

Among the various production methods mentioned above, the oxidation-reduction method is fast, simple, and can produce graphene in large quantities at a relatively low cost. However, the structural quality of graphene produced by the oxidation-reduction method is poor, because its pristine surface becomes decorated with many oxygen-containing functional groups. The appearance of these functionalities, deteriorates the crystalline structure of graphene, as well as its mechanical properties, including electrical and thermal conductivities.[44–46,49] Although the graphene-derived materials obtained by the redox method possess many disadvantages, the oxygen-containing functional groups on the surface can serve to efficiently introduce other functionalities for secondary modifications, which in turn may help to improve dispersion in organic solvents which open up new horizons for future applications.[57–59]

I.2.1.1 The scotch-tape method

This method primarily involves the mechanical separation of graphene from graphite using mechanical forces. In 2004, a research team led by A.K. Geim and K.S. Novoselov at the University of Manchester in the UK developed a simple method for producing graphene.[1,2] They adhered graphite to adhesive tape, folded the tape, and then peeled it off repeatedly. With each iteration, the graphite flakes became thinner. Subsequently, the flakes were transferred onto a silicon substrate, resulting in the successful discovery of graphene with a thickness of only one atomic layer, with maximum widths reaching approximately 10 micrometers (Fig. 3). Furthermore, it was also discovered that graphene exhibited an excellent chemical stability and maintained crystalline structure at room temperature. However, this method has drawbacks in terms of controlling the thickness and size of graphene. During the exfoliation process, numerous graphite fragments are generated, making it challenging to transfer intact graphene flakes onto a silicon substrate, posing significant challenges for its future applications in semiconductors and electronic devices.

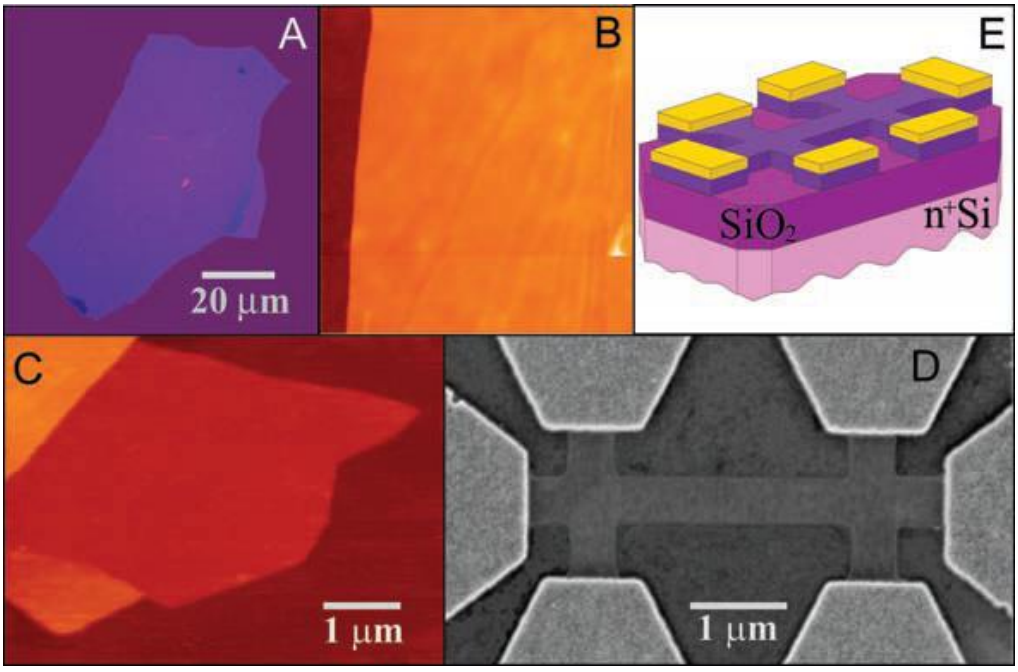

Fig. 3 Graphene films. Reprinted with permission from Science.[1]

I.2.1.2 Liquid-phase exfoliation of graphite

Liquid-phase exfoliation is a relatively simple preparation method that involves dispersing graphite in a suitable solvent, subjecting it to ultrasonic treatment, and then separating graphene from graphite through centrifugation, as shown in Fig. 4. This phenomenon was initially proposed by Hernandez et al., and according to the literature, graphene concentrations of up to 0.01 mg/ml can be achieved in N-methylpyrrolidone (NMP) solutions.[60] Alberto Mariani's research team successfully achieved to obtain a more concentrated graphene dispersion of 2.21 mg/ml in NMP by controlling the ultrasonic treatment parameters.[54,55] Although this method effectively disperses graphene in specific organic solvents, it requires careful selection of the solvent and ultrasonic parameters to succeed. Additionally, the use of ultrasonic treatment can lead to variations in graphene sheet sizes, again, posing further challenges for practical applications in semiconductors and electronic devices.

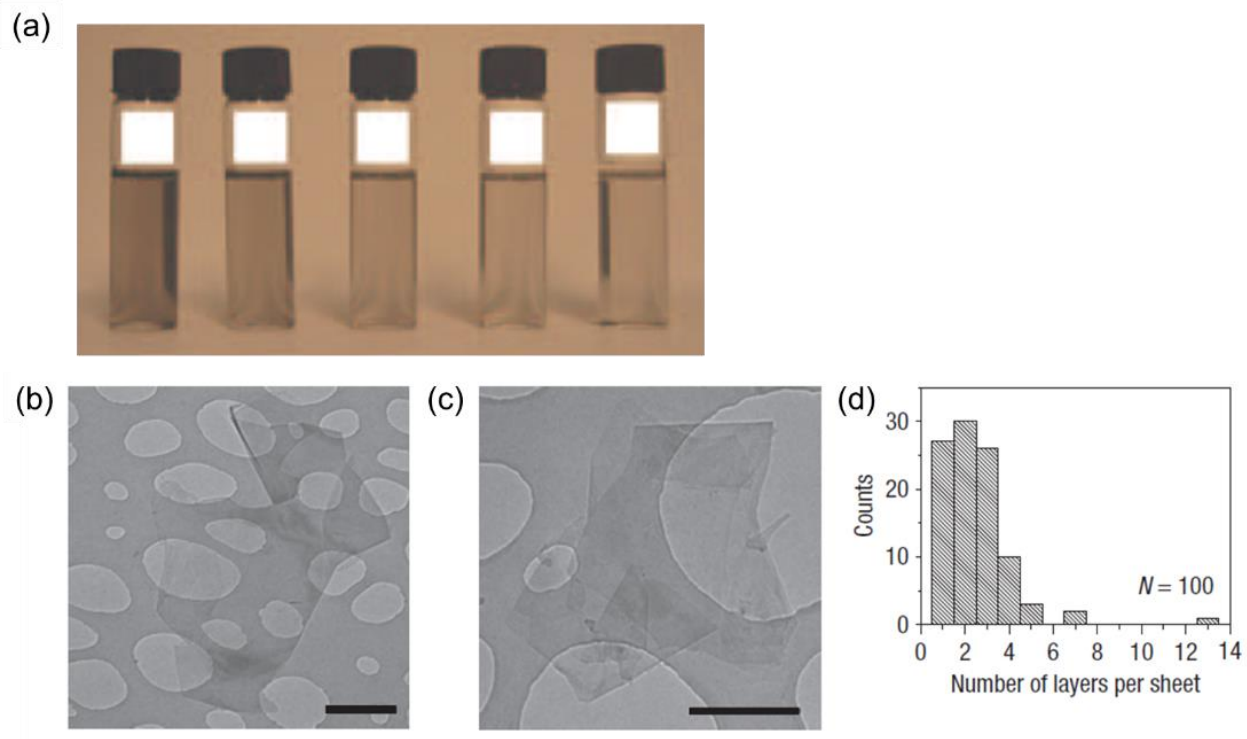

Fig. 4 (a) Dispersions of graphite flakes in NMP, at a range of concentrations ranging from 6 mg m^{-1}, (b-c) Bright-field TEM images of a folded graphene sheet and multilayer graphene, both deposited from NMP (scale bars: 500 nm)., (d) Histogram of the number of visual observations of flakes as a function of the number of monolayers per flake for NMP dispersions. reprinted with permission from nature nanotechnology.[60]

I.2.1.3 Unzipping of carbon nanotubes

This method involves the cutting of multi-walled carbon nanotubes through the action of potassium permanganate and sulfuric acid, resulting in the formation of graphene nanoribbons (GNRs), as shown in Fig. 5.[61] This method was first developed by Melinda Y. Han's research team.[62] According to the literature, the bandgap of GNRs varies depending on their width (from 0.2 to 1.5 eV), making them a significant breakthrough in the development of future semiconductors compared to graphene (which has a bandgap of 0). However, this method faces challenges not only when controlling the size and width of graphene nanoribbons, but also during the fabrication process, since GNRs are prone to oxidation, which leads to a decrease in crystallinity and changes in their physical properties.

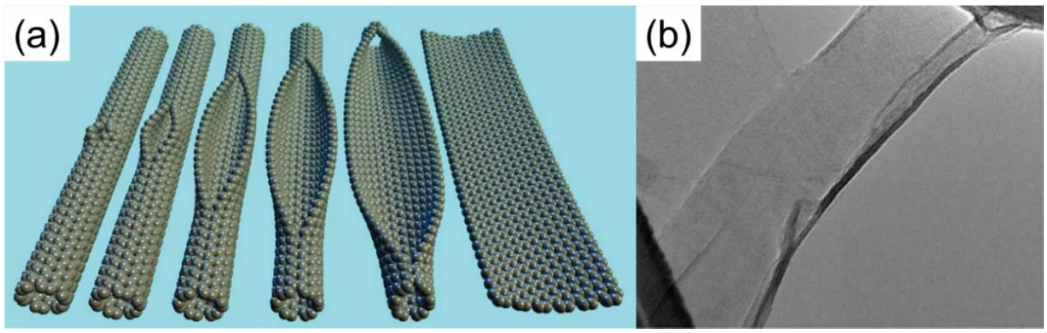

Fig. 5 (a) Representation of the gradual unzipping of one wall of a carbon nanotube to form a nanoribbon. (b) TEM images depicting the transformation of oxidized nanoribbons (right). Reprinted with permission from Nature[61]

I.2.1.4 Chemical vapor deposition (CVD)

CVD is a method used to prepare high-quality graphene on metal surfaces through chemical vapor deposition. Different metals such as ruthenium (Ru), cobalt (Co), platinum (Pt), copper (Cu), and nickel (Ni) are commonly employed in this approach.[63–67] Carbon-hydrogen compounds, such as methane, acetylene, or ethylene, serve as the carbon source and react with the metal surface at high temperatures to decompose and form a graphene layer (Fig. 6). The advantages of this method include large-scale production capability, high surface flatness, and high specific surface area. However, its disadvantages include high production costs, low productivity, and the risk of explosions during high-temperature reactions.

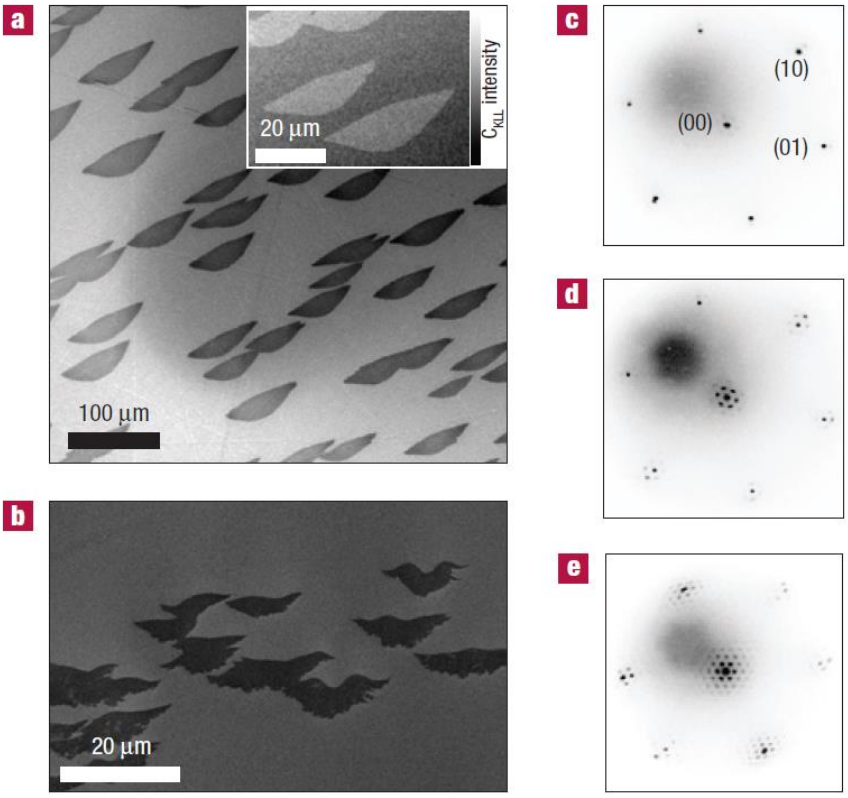

Fig. 6 Morphology of epitaxial graphene on Ru (0001). (a) UHV-SEM image of a large area of the Ru (0001) surface after first-layer graphene growth. Inset: Carbon KLL (260.6 eV) UHV scanning Auger microscopy image, obtained on this sample. (b) UHV-SEM image of a group of second-layer graphene islands. (c) Selected-area low-energy electron diffraction (electron energy: 45.4 eV) pattern of the Ru (0001) substrate. (d) Diffraction pattern of one-layer epitaxial graphene on Ru (0001) (52.2 eV). (e) Diffraction pattern of two-layer epitaxial graphene (39.1 eV). Reprinted with permission from Nature material.[66]

I.2.1.5 Epitaxial growth on silicon carbide surfaces

This fabrication method involves heating the (001) surface of a single-crystal silicon carbide substrate in ultra-high vacuum conditions, maintaining a constant temperature of approximately 1250°C to 1450°C for 1 to 20 minutes.[68–70] This process causes silicon sublimation and decarburization, resulting in the formation of a graphene film (Fig. 7). Graphene produced through this method is more uniform compared to that obtained through CVD. However, synthesizing graphene with a specific thickness over a large area using this method still remains challenging.

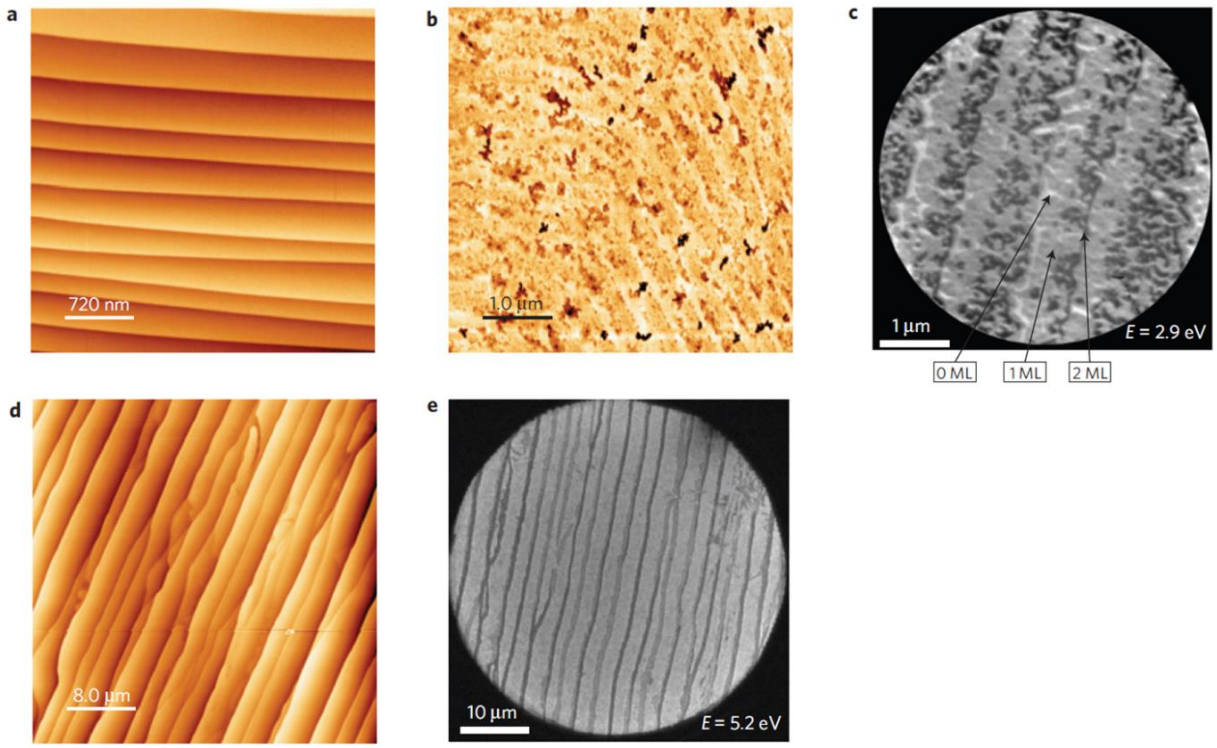

Fig. 7 **Morphological changes of 6H–SiC(0001) during graphene growth.** (a) Initial surface after H-etching imaged by AFM. The step height is 15 Å. (b), AFM image of graphene on 6H-SiC(0001) with a nominal thickness of 1ML formed by annealing in UHV at a temperature of about 1,280 °C. (c) LEEM image of a UHV-grown graphene film on SiC(0001) with a nominal thickness of 1.2 monolayers. The image contrast is due to the locally different layer thickness. Light, medium and dark grey correspond to a local thickness of 0, 1 and 2 ML, respectively. (d) AFM image of graphene on 6H-SiC(0001) with a nominal thickness of 1.2ML formed by annealing in Ar (*p*D900 mbar, *T* D1,650 °C). **e**, LEEM image of a sample equivalent to that of **d** revealing macro-terraces covered with graphene up to 50 µm long and at least 1 µm wide. Reprinted with permission from Nature material.[69]

I.2.2 Graphene oxide (GO) reduction method

I.2.2.1 Preparation of GO

Before the discovery of graphene, GO was commonly referred to as oxidized graphene or graphite acid.[71] The first successful production of GO was accomplished by Brodie through the action of nitric acid and potassium chlorate, resulting in the formation of graphene oxide flakes with a thickness of 0.05 mm. In 1957, Hummers and Offerman developed a safe and fast process known as the Hummers' method, by using a mixture of sulfuric acid, sodium nitrate, and potassium permanganate. This method is still widely used and has undergone numerous modifications over time, as shown in Fig. 8.

The resulting GO prepared by using this method contains various oxygen-containing functional groups on its surface, such as C=O, -OH, and -COOH.[72–74] The presence of these oxygen-containing groups on the surface facilitates its dispersion in water. According to the literature, GO can be successfully dispersed in specific organic solvents such as NMP, N,N-dimethylformamide (DMF), and tetrahydrofuran (THF) polar solvents. [75,76] Due to these properties, GO can be effectively dispersed in polymer materials. Furthermore, additional chemical modifications can be introduced to GO, enabling further enhancements in solvent dispersibility and widen the range of potential applications. Table 1 summarizes the advantages, disadvantages, application prospects, and physical properties of graphene and GO. Various methods, including thermal reduction, microwave reduction, and chemical reduction, can be employed to convert GO back into graphene.

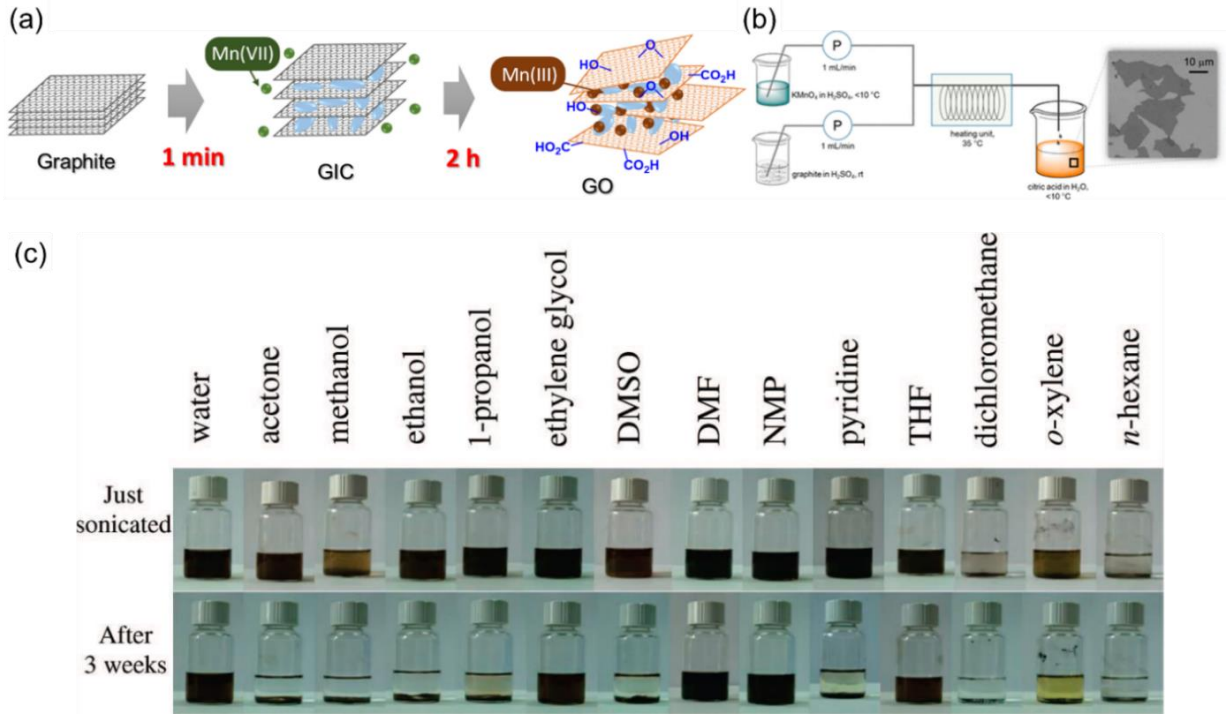

Fig. 8 (a) Summary of various Hummers' methods used to oxidize graphite to GO. (b) (left) Basic design of a continuous-flow system used to synthesize GO. (right) SEM image of a flake of GO obtained from the continuous flow system after exfoliation by sonication. (c) GO dispersed in water and 13 organic solvents through bath ultrasonication. Reprinted with permission from Chemistry of Materials and Langmuir.[74,76]

Table 1 Comparison of the advantages and disadvantages of graphene and GO.

Material	Advantage[36,39,49,56–59,74,76]	Disadvantage[44–46,49]
Graphene	* High electrical and thermal conductivities * High Mechanical properties * High control on functionalization	* High cost * Small production * Difficult workability
Graphene oxide (GO)	* Water dispersibility * Polar functionalization * Low cost * Easy workability	* Lower electrical and thermal conductivities * Surface random functionalization

I.2.2.2 Thermal reduction of GO

The thermal reduction method involves high-temperature reduction of oxygen-containing functional groups on the surface of GO to form carbon-carbon double bonds, effectively producing multi-layer graphene flakes.[77] However, this method requires precise control of the heating temperature and rate of temperature increase to ensure consistent reduction and crystallinity of graphene oxide. In 2006, Schniepp et al. studied the synthesis of graphene through the thermal reduction of GO. When GO is heated to 1050 °C in an inert gas for 30 seconds, it undergoes layer exfoliation and reduction.[77] Layer exfoliation occurs when the temperature exceeds 600 °C, causing the carboxyl groups (COOH) and OH present on the GO surface to vaporize, producing carbon dioxide (CO_2).[78] When the pressure from CO_2 exceeds the van der Waals forces between the GO layers, exfoliation of GO occurs. The graphene produced through this method is known as thermally reduced graphene oxide (TRGO). The advantage of this method is that reduction and exfoliation can be simultaneously achieved in a single step. However, the physical properties of the reduced graphene oxide can vary at different temperatures.[79] In 2018, Sengupta et al. observed that the specific surface area of GO varied with different reduction temperatures, with the achievement of a maximum surface area of 437.62 m^2/g after reduction at 350 °C (Fig. 9), thus highlighting the importance of temperature control during the reduction process of GO.[80]

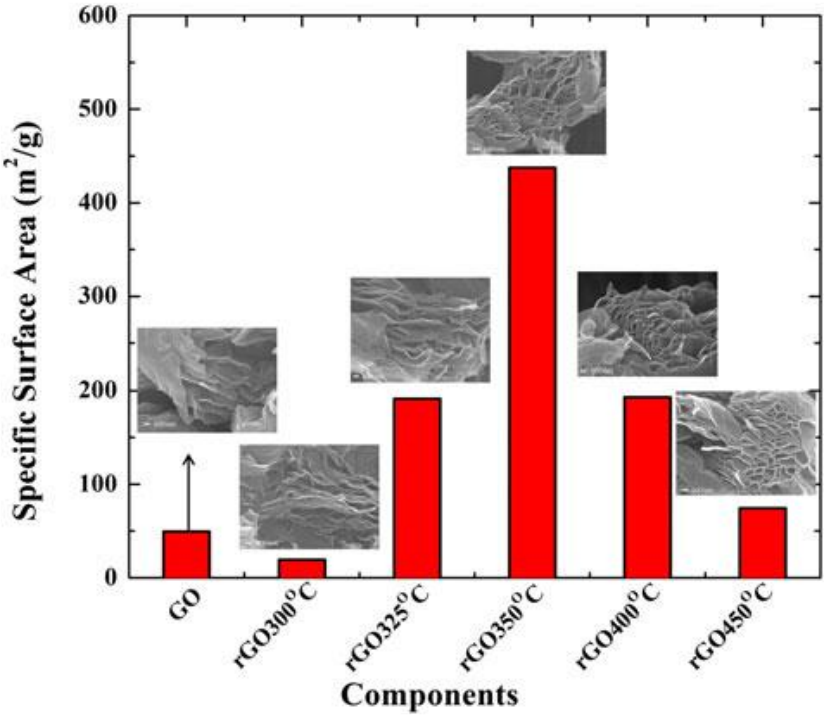

Fig. 9 Specific surface area of GO and rGO specimens. Reproduced with permission from [80]

I.2.2.3 Microwave reduction of GO

The microwave reduction method involves a rapid temperature increase by agitating free electrons, leading to the decomposition of functional groups on the surface of GO and reduction achievement.[81] This method offers rapid and uniform heating, resulting in the successful exfoliation of GO. In 2010, Rodney S. Ruoff and his research team, by microwave rapid heating of GO, demonstrated that the specific surface area of GO would increase to 463 m^2 / g (original 7 ~ 9 times) (Fig. 10), and the battery and capacitor obtained by this material exhibit good performance.[82] In 2016, Vioy et al. found that GO could be reduced to graphene within a few seconds by using a simple microwave oven, and Raman analysis showed that the crystallinity of the reduced GO was comparable to that of graphene produced through CVD.[83]

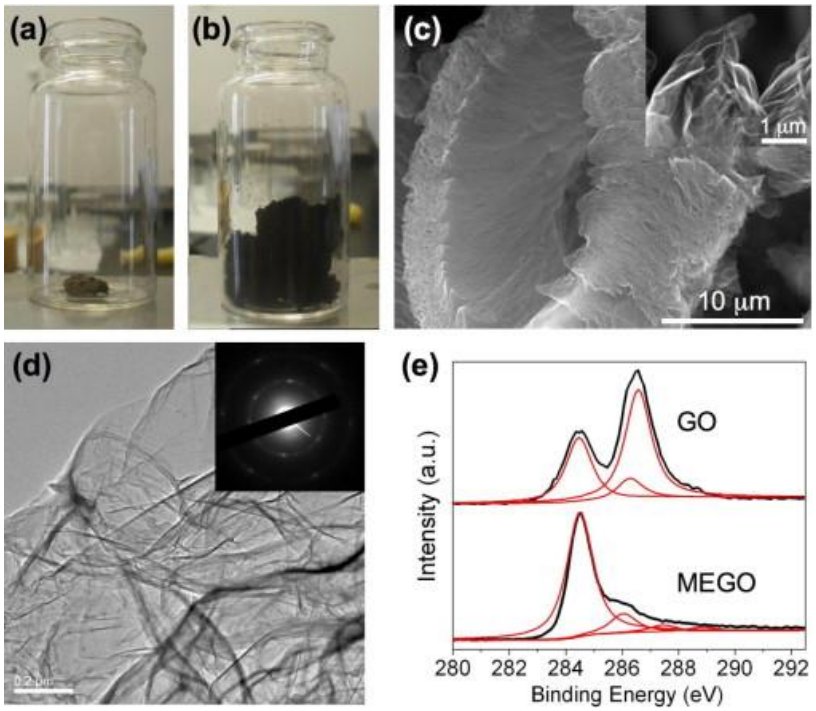

Fig. 10 Optical photos of GO before (a) and after (b) treatment in a microwave oven for 1 min. (c) Typical SEM image of as-prepared MEGO by microwave irradiation with a high magnification SEM image in the inset showing the crumpled MEGO sheets. (d) Typical TEM image of the MEGO and the corresponding electron diffraction pattern. (e) XPS C1s spectra of GO and MEGO. Reproduced with permission from Carbon.[83]

I.2.2.4 Chemical reaction of GO

We have previously stated that GO possesses numerous oxygen-containing functional groups on its surface, leading to a high density of crystalline defects. Therefore, a strong reducing agent is required to effectively reduce and eliminate these functional groups. The initial research by Sasha Stankovich's team used hydrazine, leading to the successful reduction of GO to graphene.[84,85] The study showed a decrease in the C-O and C=O peaks on the surface of hydrazine-reduced GO, indicating that the reduction of oxygen-containing functional groups was successful. The reduced GO exhibited improved thermal stability when compared to pristine GO. Although hydrazine can effectively reduce GO, it is an expensive material which in addition is harmful to the environment. Subsequent studies have identified alternative chemical reducing agents for GO, such as sodium borohydride,[86,87] hexamethylenetetramine,[88,89] Vitamin C[90,91] and ascorbic acid.[92]

I.3 Boron nitride (BN)

Boron nitride is an artificially synthesized inorganic compound, primarily composed of boron (B) and nitrogen (N) atoms. Due to differences in crystal structures, it can be classified into cubic boron nitride (c-BN),[93] wurtzite boron nitride (w-BN),[94] and hexagonal boron nitride (h-BN).[95,96] The structure of h-BN consists of boron and nitrogen atoms alternately arranged in an SP^2 hexagonal honeycomb structure and stacked with boron on top of nitrogen and vice versa (AAA-stacking) (Fig. 11). The structure is similar to that of graphite and because of its white color, it is commonly referred to as "white graphite". A single layer of BN is also termed "white graphene".[97,98]

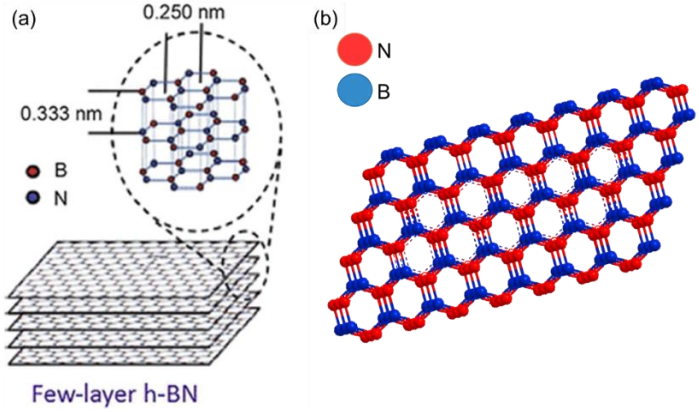

Fig. 11 (a) The structure of h-BN nanosheets. Reproduced with permission from 2016 Elsevier Inc.[96] (b) The lattice of h-BN with an AAA stacking.

The thermal and chemical stability of h-BN typically leads to its application in high-temperature equipment components. BN has relatively weak interlayer bonding, making its layers to easily slide when shear forces are applied. For this reason, h-BN is frequently used in bearings and lubricants. Recent research has shown that h-BN, with its unique electrical insulating properties and a wide band gap of 5.9 eV,[11,99] coupled with a hexagonal atomic structure, exhibits minimal lattice mismatch and high uniformity with graphene. This makes h-BN an effective substrate for graphene, proving beneficial for future semiconductor applications.[99,100] Owing to h-BN exhibiting commendable mechanical properties, thermal conductivity, lubricity, and corrosion resistance, its application in polymer composite materials has been gradually increasing in recent years.[35,101,102]

I.3.1 Preparation of hexagonal boron nitride (h-BN)

The synthesis of h-BN is achieved by the reaction of boron trioxide or boric acid with ammonia or urea under a nitrogen atmosphere, low temperature and pressure. When h-BN is subjected to high temperature and high pressure, it transforms into c-BN or w-BN. The variation in crystal structure (Fig. 12)[103] results in different physical properties such as thermal conductivity, electrical characteristics, mechanical properties, and density. The Table 2 below compares the physical properties of c-BN, h-BN, and w-BN.

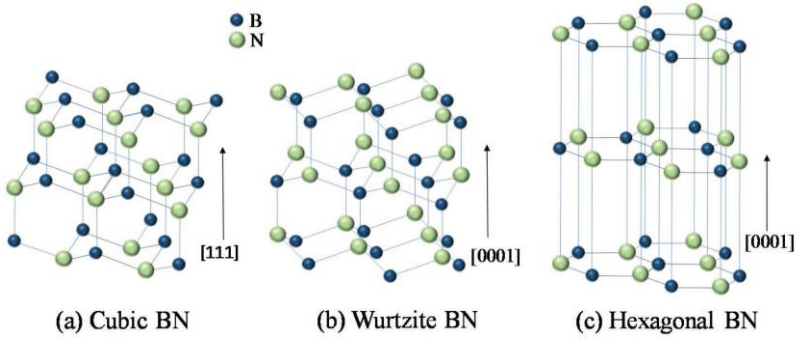

Fig. 12 Crystal structures of (a) cubic, (b) wurtzite, and (c) hexagonal BN. Reproduced with permission from Advanced Electronic Materials.[103]

Table 2 Literature data on the physical properties of various BN polymorphs.[93–95,103,104]

Type	c-BN	w-BN	h-BN
Lattice constant (A)	a=3.62	a=2.53 c=4.2	a=2.49 c=6.66
Density (g/cm^3)	3.45	3.49	2.27
Melting point (°C)	2973	-	3000
Energy gap (eV)	~6.4	4.5-5.5	5.2
Electrical resistance (Ω cm)	10^2-10^{10}	-	10^{10}
Dielectric constant	4.5	-	3.29-3.76
Tensile strength (GPa)	65.2	-	70.5
Young modulus (TPa)	1.07	-	0.865
Thermal conductivity (W/m K)	1.3	-	~550

I.3.2 Preparation of boron nitride nanosheets (BNNS)

lkI.3.2.1 Mechanical exfoliation

I.3.2.1.1 Tape exfoliation

This method utilizes mechanical force to overcome the van der Waals forces between BN layers, yielding boron nitride nanosheets. D. Pacilé and colleagues employed adhesive tape to peel off BN layers from powdered h-BN and then press them onto a target substrate, thus isolating BN nanosheets (BNNS). Through a repeated exfoliation-pressing process, BNNS can be exfoliated down to a single-layer level. While large-area h-BN sheets with an average crystal size of about 10 μm have been obtained, these sheets present an uneven surface; the thinnest regions are approximately 3.5 nm, while the thickest are around 80 nm (Fig. 13).[105,106] Structurally complete layer less BNNS prepared in this mothed is fascinating. However, this method is inefficient, and the lateral size of BNNS is constrained by that of commercial h-BN powder.

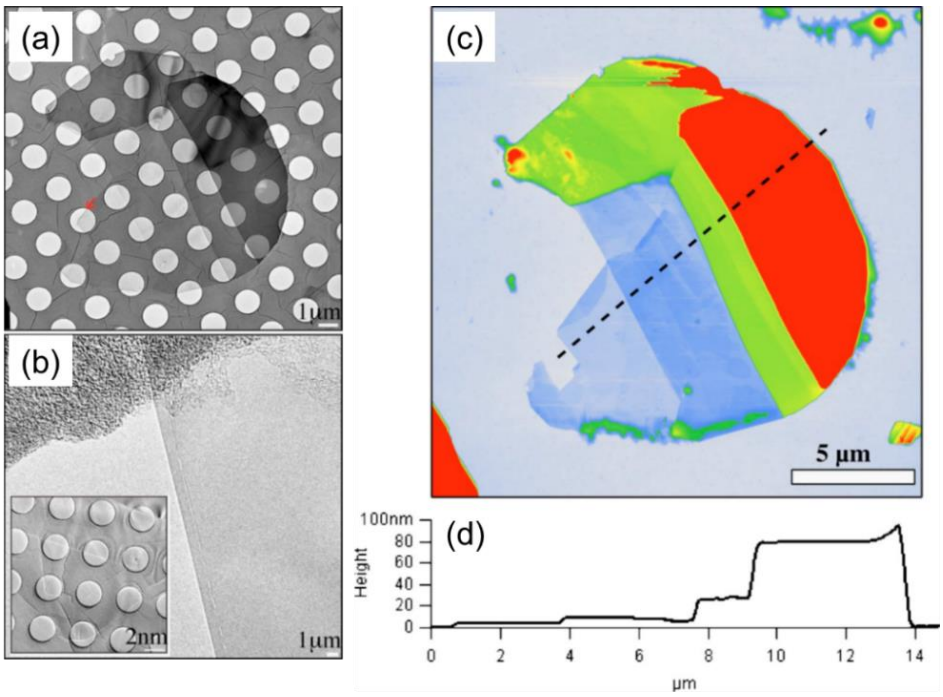

Fig. 13 TEM and AFM images of BN. (a) TEM overview performed at low magnification and large defocus. (b) The folding indicated by red arrow in the overview image. (c) AFM tapping mode topography image of boron nitride. (d) The dashed lines indicate the position of the line profile. Reproduced with permission from Applied Physics Letters.[105]

I.3.2.1.2 Ball milling

Due to the extremely low efficiency of the tape method, its current production only meets laboratory requirements. To enhance scalability, shear force methodologies have been explored. Ball milling is one of the most common mechanical exfoliation methods. There are two approaches within ball milling: dry ball milling and wet ball milling. Previous research suggests that with the dry ball milling method, the lateral size of particles can be reduced from 394-607 nm to 90-214 nm. Wet ball milling involves the use of aqueous solutions. Past studies have shown that under a NaOH solution, shear can be reduced, and h-BN nanosheets can be successfully cut (Fig. 14a).[107] Moreover, h-BN easily reacts with amine ions, resulting in slightly damaged amino-functionalized BN nanosheets (NH_2-BNNs) (Fig. 14b-f).[108,109] Despite ball milling being a scalable method, a significant drawback consists in how easily surface defects can occur in BNNS as well as the uneven size distribution, presenting challenges for future technological applications.

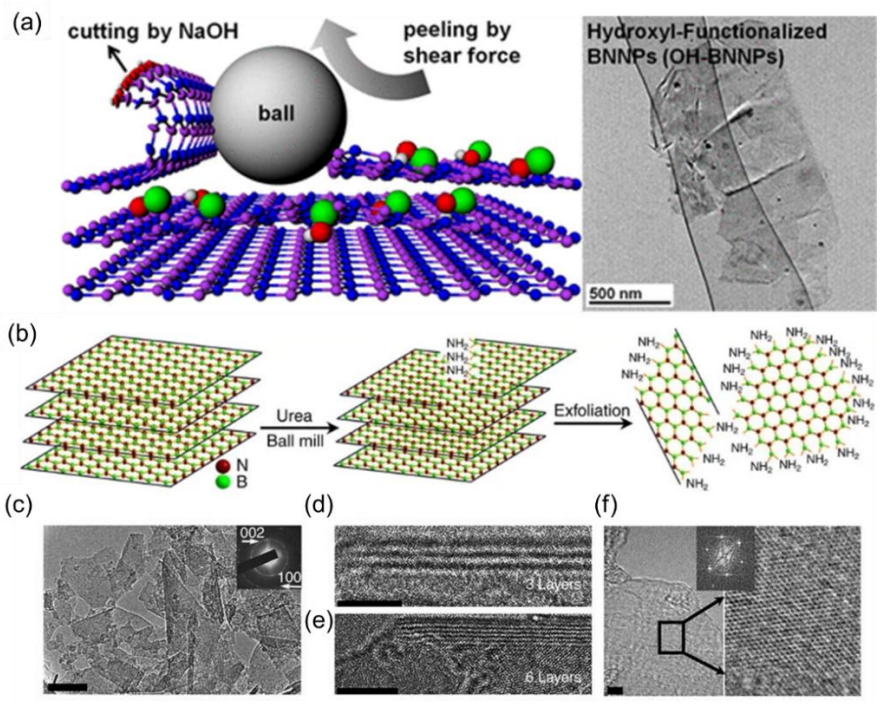

Fig. 14 (a) Schematic diagram and corresponding SEM images of the exfoliation mechanism of h-BN. Reproduced with permission from Nano Lett.[107] (d) TEM image of few-layer BN (d,e) HRTEM images of the edge folding of two few-layer BN sheets with three and six BN layers, respectively. Scale bars, (d) 2 nm and (e) 5 nm. (f) HRTEM and the fast Fourier transform images of a few-layer BN sheet. Scale bar, 2 nm Reproduced with permission from nature communications.[108]

I.3.2.1.3 Fluid shearing

Fluid shearing is a newer method for producing BNNs. As previously mentioned, h-BN powder can be dispersed in an organic solvent by using a stabilizing surfactant to enhance dispersion and prevent h-BN clumping. As shown in Fig. 15 the solution containing h-BN is then rapidly rotated through a 45-degree angled glass tube, creating a parabolic flow, which facilitates the shearing of the h-BN dispersed in the solution, producing some BNNs.[110] Some recent research indicates that high-pressure microflows can produce few-layer BNNs on a large scale. In this case, h-BN is dispersed in a DMF organic solvent and pressured through a pump, reaching speeds of up to 400 m/s through a narrow channel. The shear force produced by the pressure difference in the solution is used to successfully exfoliate h-BN into BNNs.[111] While this method is effective, meticulous parameter control is required to ensure the integrity and uniformity of the BNNs.

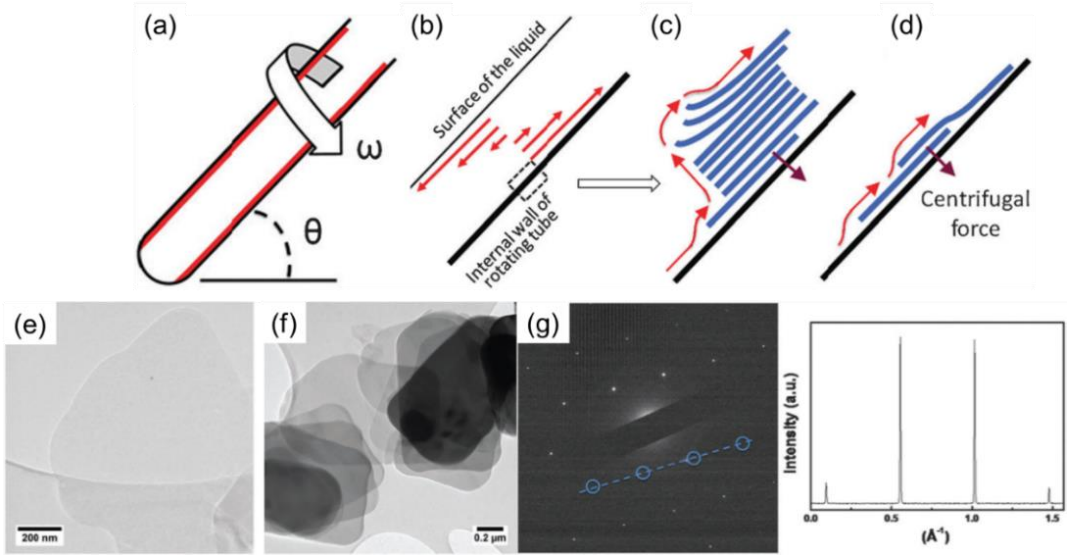

Fig. 15 (a) Schematic of the vortex fluidic device. (b) the microfluidic flow velocity indicted by red arrows for a section of the rotating tube and (c) the exfoliation process, and (d) slippage on the inner surface of the tube (e) TEM of monolayer BN. (f) TEM of adjacent BN layers with the same size and shape. (g) SAED pattern of the boron nitride. Reproduced with permission from Chemical Communications.[110]

I.3.2.1.4 Ultrasonic exfoliation

In essence, this exfoliation method aligns with the liquid-phase exfoliation of graphene. It primarily involves sonication of the material in water or polar organic solvent solutions, disrupting the van der

Waals forces between the BN layers to obtain BNNs. Prior studies have indicated that small amounts of OH-BNNs can be effectively dispersed in water by using this method (Fig. 16).[112,113] Although simple and rapid, this method cannot efficiently control the size of the BNNs flakes.

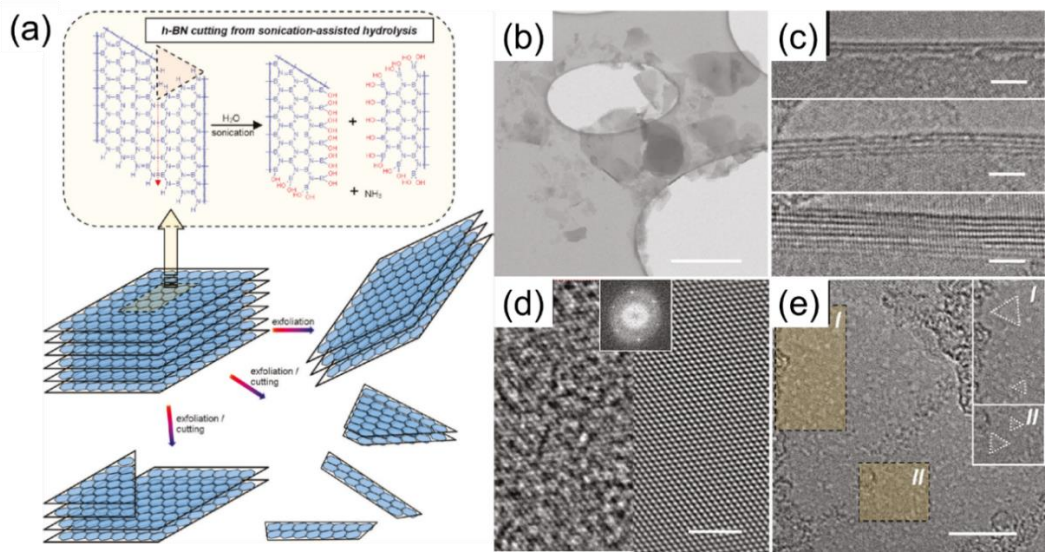

Fig. 16 (a) An example scheme shown on the top is the cutting started from a nitrogen-edged hole defect site (marked with triangle) with the arrow as the cutting direction.(b) a typical low-magnification TEM image. (c) HR-TEM images of the folded edges of several nanosheets (d) an HR-TEM image of a nanosheet and the corresponding simulated image from inverse FFT. (e) An HR-TEM image of a few-layered nanosheet from aqueous dispersion. Reproduced with permission from J. Phys. Chem. C [112]

I.3.2.2 Chemical functionalization of h-BN

I.3.2.2.1 Unzipping BN nanotubes (BNNTs)

This method involves plasma etching to incise and cut multi-layered BNNTs into BN nanoribbons (BNNR), as depicted in Fig. 17,[114] the method was originally developed by the Haibo Zeng research group.[115] Literature suggests that BNNRs exhibit excellent conductivity and carrier mobility. Due to the jagged edges and vacancy defects of BNNRs, it has been proven to be a semiconductor. This represents not only a significant breakthrough for the future development of semiconductors but also a solution for various challenges and applications in electronic and spintronic devices. However, the high cost and limited yield of this method mean that significant improvements are still needed for future applications.[114,116]

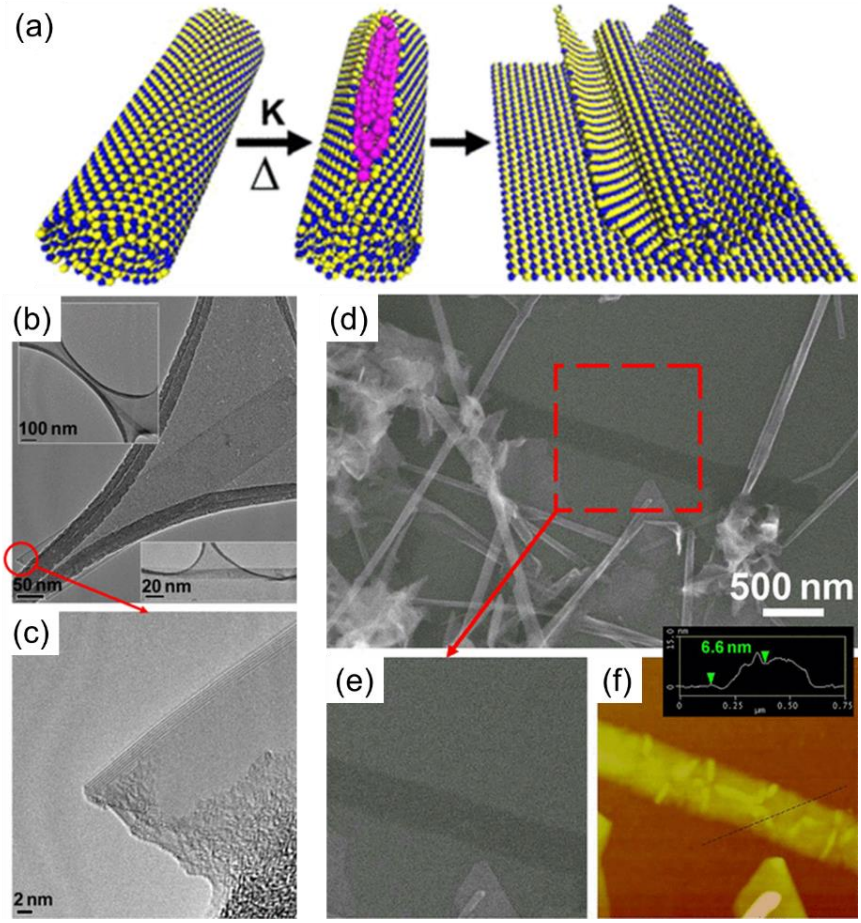

Fig. 17 (a) Scheme of the unzipping of BNNTs to form BNNRs. (b) TEM images of three representative BNNRs. (c) High-resolution TEM image of the edge of a ribbon shown in the center of panel (b). (d) SEM image of a BNNR sample showing a long straight ribbon in the center (e) SEM and (f) AFM. [114]

I.3.2.2.2 Chemical vapour deposition (CVD)

In 1981, Takehiko Takahashi's research team at Nagoya University made strides in producing h-BN thin films on carbon steel substrates using CVD.[117] However, the excessive thickness of the films and their imperfect crystallization limited their application in electronic devices. Addressing the h-BN crystallinity issue, the National Institute for Materials Science (NIMS) in Japan, in 2004, managed to fabricate single-crystalline h-BNs with thicknesses ranging between 10-100 nm, employing high pressures (4.0-5.5 GPa) and elevated temperatures (1500-1750 °C).[11] Despite this, a significant challenge still remained: the h-BN surfaces produced were irregular, and necessitated the manual extraction of individual layers to achieve monolayer-structured BNNs. The resultant h-BN sheets also

lacked uniformity in size, making commercial-scale applications challenging. While the successful fabrication of single-layer BNNs on molten gold surfaces was achieved in 2018,[118] the commercial viability of this method remains limited due to the prohibitive cost of molten gold. In a significant advancement in 2020, Taiwan Semiconductor Manufacturing Company (TSMC) research team pioneered the fabrication of single-layer BNNs on Cu (111) using low-pressure chemical deposition (as depicted in Fig. 18).[119] When transferring these BNNs onto 2-inch Si wafers, they achieved an electron mobility enhancement of over 100%. This breakthrough underpins the viability of the CVD process in producing large-area BNNs, marking a pivotal step for the prospective integration of these materials for semiconductor advancement.

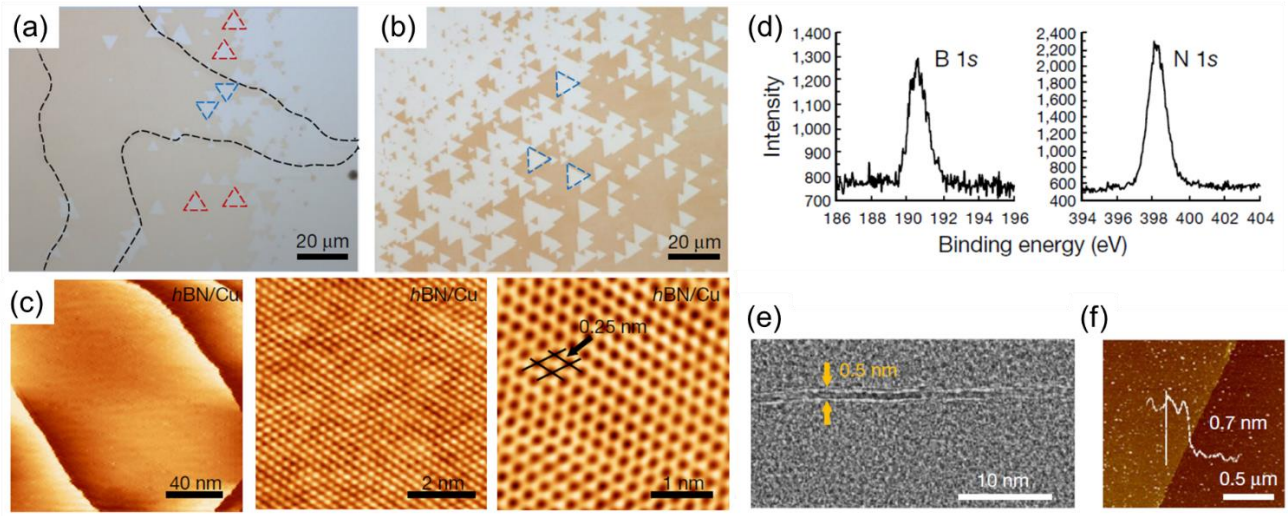

Fig. 18 (a) Optical microscope image of h-BN grown on different Cu (111) grains. (b) Oppositely oriented flakes are marked by red and blue dashed triangles. (c) Mono-oriented h-BN flakes on single-crystal Cu (111) films. (d) Raman spectrum of a transferred h-BN film (e) Cross-sectional TEM image of a monolayer h-BN transferred onto SiO_2/Si, where the thickness of h-BN is around 0.5 nm (f) AFM image of a single-crystal h-BN film transferred onto a SiO_2/Si substrate. Reproduced with permission from nature[119].

II CONCLUSIONS

The above describes a lot about the production of 2D material. Although 2D materials have very good physical properties, these are based on the condition of high crystallinity in order to effectively perform. In order to expand the application of 2D material, mixing with polymer materials to make composite materials is a very potential choice. Especially in recent years, due to the rapid development of 5G communication, the thermal stability, high strength, and low dielectric coefficient polyimide materials have attracted a lot of attention. Therefore, the development, characterization and application of polyimide and 2D material will be discussed in Chapter 2.

REFERENCES

1. Novoselov, K. S. *et al.* Electric Field Effect in Atomically Thin Carbon Films. *Science.* **306**, 666–669 (2004).
2. Geim, A. K. & MacDonald, A. H. Graphene: Exploring carbon flatland. *Phys. Today* **60**, 35–41 (2007).
3. Chiu, M.-H. *et al.* Determination of band alignment in the single-layer MoS2/WSe2 heterojunction. *Nat. Commun.* **6**, 7666 (2015).
4. Eftekhari, A. Tungsten dichalcogenides (WS 2 , WSe 2 , and WTe 2): materials chemistry and applications. *J. Mater. Chem. A* **5**, 18299–18325 (2017).
5. Gong, C. *et al.* Discovery of intrinsic ferromagnetism in two-dimensional van der Waals crystals. *Nature* **546**, 265–269 (2017).
6. Huang, B. *et al.* Layer-dependent ferromagnetism in a van der Waals crystal down to the monolayer limit. *Nature* **546**, 270–273 (2017).
7. Samarth, N. Condensed-matter physics: Magnetism in flatland. *Nature* vol. 546 216–218 (2017).
8. Naguib, M., Mochalin, V. N., Barsoum, M. W. & Gogotsi, Y. 25th Anniversary Article: MXenes: A New Family of Two-Dimensional Materials. *Adv. Mater.* **26**, 992–1005 (2014).
9. Naguib, M. *et al.* Two-Dimensional Nanocrystals Produced by Exfoliation of Ti3AlC2. *Adv. Mater.* **23**, 4248–4253 (2011).
10. Park, J.-H. *et al.* Large-Area Monolayer Hexagonal Boron Nitride on Pt Foil. *ACS Nano* **8**, 8520–8528 (2014).
11. Watanabe, K., Taniguchi, T. & Kanda, H. Direct-bandgap properties and evidence for ultraviolet lasing of hexagonal boron nitride single crystal. *Nature Materials* vol. 3 404–409 (2004).
12. Jariwala, D. *et al.* Control of emergent properties at a correlated oxide interface with graphene. *Nano Letters* vol. 15 170–181 (2015).
13. Novoselov, K. S., Mishchenko, A., Carvalho, A. & Castro Neto, A. H. 2D materials and van der Waals heterostructures. *Science.* **353**, (2016).
14. Butler, S. Z. *et al.* Progress, Challenges, and Opportunities in Two-Dimensional Materials Beyond Graphene. *ACS Nano* **7**, 2898–2926 (2013).
15. Bhimanapati, G. R. *et al.* Recent Advances in Two-Dimensional Materials beyond Graphene. *ACS Nano* **9**, 11509–11539 (2015).
16. Yeh, C. N., Raidongia, K., Shao, J., Yang, Q. H. & Huang, J. On the origin of the stability of graphene oxide membranes in water. *Nature Chemistry* vol. 7 166–170 (2015).
17. Ding, L. *et al.* A Two-Dimensional Lamellar Membrane: MXene Nanosheet Stacks. *Angew. Chemie Int. Ed.* **56**, 1825–1829 (2017).

18. Liu, G., Jin, W. & Xu, N. Two-Dimensional-Material Membranes: A New Family of High-Performance Separation Membranes. *Angew. Chemie Int. Ed.* **55**, 13384–13397 (2016).
19. Peng, J., Chen, X., Ong, W.-J., Zhao, X. & Li, N. Surface and Heterointerface Engineering of 2D MXenes and Their Nanocomposites: Insights into Electro- and Photocatalysis. *Chem* **5**, 18–50 (2019).
20. Tian, W. *et al.* Multifunctional Nanocomposites with High Strength and Capacitance Using 2D MXene and 1D Nanocellulose. *Adv. Mater.* **31**, 1902977 (2019).
21. Pan, F. *et al.* Improved synergistic effect for achieving ultrathin microwave absorber of 1D Co nanochains/2D carbide MXene nanocomposite. *Carbon.* **172**, 506–515 (2021).
22. Reddy, A. L. M. *et al.* Synthesis Of Nitrogen-Doped Graphene Films For Lithium Battery Application. *ACS Nano* **4**, 6337–6342 (2010).
23. Anasori, B., Lukatskaya, M. R. & Gogotsi, Y. 2D metal carbides and nitrides (MXenes) for energy storage. *Nature Reviews Materials* vol. 2 (2017).
24. Mashtalir, O., Lukatskaya, M. R., Zhao, M.-Q., Barsoum, M. W. & Gogotsi, Y. Amine-Assisted Delamination of Nb 2 C MXene for Li-Ion Energy Storage Devices. *Adv. Mater.* **27**, 3501–3506 (2015).
25. Chen, T. A. *et al.* Wafer-scale single-crystal hexagonal boron nitride monolayers on Cu (111). *Nature* vol. 579 219–223 (2020).
26. Shen, P. C. *et al.* Ultralow contact resistance between semimetal and monolayer semiconductors. *Nature* vol. 593 211–217 (2021).
27. Wan, Y. *et al.* Low-defect-density WS2 by hydroxide vapor phase deposition. *Nat. Commun.* **13**, 4149 (2022).
28. Wu, F. *et al.* Vertical MoS2 transistors with sub-1-nm gate lengths. *Nature* vol. 603 259–264 (2022).
29. Gür, T. M. Review of electrical energy storage technologies, materials and systems: challenges and prospects for large-scale grid storage. *Energy Environ. Sci.* **11**, 2696–2767 (2018).
30. Yan, X. *et al.* 2D Organic Materials: Status and Challenges. *Adv. Sci.* **10**, (2023).
31. Zhao, Z. *et al.* N-Doped Carbon–WS 2 Nanosheet Composites for Lithium-Ion Storage. *ACS Appl. Nano Mater.* **4**, 7781–7787 (2021).
32. Gao, L. *et al.* MXene/Polymer Membranes: Synthesis, Properties, and Emerging Applications. *Chem. Mater.* **32**, 1703–1747 (2020).
33. Liao, W.-H. *et al.* Effect of Molecular Chain Length on the Mechanical and Thermal Properties of Amine-Functionalized Graphene Oxide/Polyimide Composite Films Prepared by In Situ Polymerization. *ACS Appl. Mater. Interfaces* **5**, 869–877 (2013).
34. Zhu, Y. *et al.* Graphene–Carbon Composite Films as Thermal Management Materials. *ACS Appl. Nano Mater.* **3**, 9076–9087 (2020).

35. Wang, Y. *et al.* Functionalized Boron Nitride Nanosheets: A Thermally Rearranged Polymer Nanocomposite Membrane for Hydrogen Separation. *Angew. Chemie Int. Ed.* **57**, 16056–16061 (2018).
36. Zandiatashbar, A. *et al.* Effect of defects on the intrinsic strength and stiffness of graphene. *Nat. Commun.* **5**, 3186 (2014).
37. Scarpa, F., Adhikari, S. & Srikantha Phani, A. Effective elastic mechanical properties of single layer graphene sheets. *Nanotechnology* **20**, 065709 (2009).
38. King, A., Johnson, G., Engelberg, D., Ludwig, W. & Marrow, J. Observations of Intergranular Stress Corrosion Cracking in a Grain-Mapped Polycrystal. *Science.* **321**, 382–385 (2008).
39. Balandin, A. A. Thermal properties of graphene and nanostructured carbon materials. *Nat. Mater.* **10**, 569–581 (2011).
40. Chen, S. *et al.* Raman Measurements of Thermal Transport in Suspended Monolayer Graphene of Variable Sizes in Vacuum and Gaseous Environments. *ACS Nano* **5**, 321–328 (2011).
41. Balandin, A. A. *et al.* Superior Thermal Conductivity of Single-Layer Graphene. *Nano Lett.* **8**, 902–907 (2008).
42. Ni, Z. H. *et al.* Graphene Thickness Determination Using Reflection and Contrast Spectroscopy. *Nano Lett.* **7**, 2758–2763 (2007).
43 huang, Y., Wu, J. & Hwang, K. C. Thickness of graphene and single-wall carbon nanotubes. *Phys. Rev. B* **74**, 245413 (2006).
44. Bolotin, K. I. *et al.* Ultrahigh electron mobility in suspended graphene. *Solid State Communications* vol. 146 351–355 (2008).
45. Orlita, M. *et al.* Approaching the Dirac Point in High-Mobility Multilayer Epitaxial Graphene. *Phys. Rev. Lett.* **101**, 267601 (2008).
46. Wang, X., Zhi, L. & Müllen, K. Transparent, Conductive Graphene Electrodes for Dye-Sensitized Solar Cells. *Nano Lett.* **8**, 323–327 (2008).
47. Morozov, S. V. *et al.* Giant intrinsic carrier mobilities in graphene and its bilayer. *Physical Review Letters* vol. 100 (2008).
48. Gómez-Navarro, C. *et al.* Electronic Transport Properties of Individual Chemically Reduced Graphene Oxide Sheets. *Nano Lett.* **7**, 3499–3503 (2007).
49. GEIM, A. K. & NOVOSELOV, K. S. The rise of graphene. in *Nanoscience and Technology* 11–19 (Co-Published with Macmillan Publishers Ltd, UK, 2009). doi:10.1142/9789814287005_0002.
50. Tour, J. M. Top-Down versus Bottom-Up Fabrication of Graphene-Based Electronics. *Chem. Mater.* **26**, 163–171 (2014).
51. Allen, M. J., Tung, V. C. & Kaner, R. B. Honeycomb Carbon: A Review of Graphene. *Chem. Rev.* **110**, 132–145 (2010).
52. Campéon, B. D. L. *et al.* Non-destructive, uniform, and scalable electrochemical functionalization and exfoliation of graphite. *Carbon.* **158**, 356–363 (2020).

53 hung, Y.-F., Cheng, C., Huang, C.-K., Yang, C.-R. & Tseng, S.-F. Investigation of electrochemical reduction effects on graphene oxide powders for high-performance supercapacitors. *Int. J. Adv. Manuf. Technol.* **113**, 1203–1213 (2021).

54. Nuvoli, D. *et al.* High concentration few-layer graphene sheets obtained by liquid phase exfoliation of graphite in ionic liquid. *J. Mater. Chem.* **21**, 3428–3431 (2011).

55. Alzari, V. *et al.* Graphene-containing thermoresponsive nanocomposite hydrogels of poly(N-isopropylacrylamide) prepared by frontal polymerization. *J. Mater. Chem.* **21**, 8727 (2011).

56. Berger, C. *et al.* Electronic Confinement and Coherence in Patterned Epitaxial Graphene. *Science.* **312**, 1191–1196 (2006).

57. Joshi, R. K., Alwarappan, S., Yoshimura, M., Sahajwalla, V. & Nishina, Y. Graphene oxide: the new membrane material. *Appl. Mater. Today* **1**, 1–12 (2015).

58. Su, C. & Loh, K. P. Carbocatalysts: Graphene Oxide and Its Derivatives. *Acc. Chem. Res.* **46**, 2275–2285 (2013).

59. Zou, T. *et al.* High-speed femtosecond laser plasmonic lithography and reduction of graphene oxide for anisotropic photoresponse. *Light Sci. Appl.* **9**, 69 (2020).

60. Hernandez, Y. *et al.* High-yield production of graphene by liquid-phase exfoliation of graphite. *Nature Nanotechnology* vol. 3 563–568 (2008).

61. Kosynkin, D. V. *et al.* Longitudinal unzipping of carbon nanotubes to form graphene nanoribbons. *Nature* **458**, 872–876 (2009).

62. Han, M. Y., Özyilmaz, B., Zhang, Y. & Kim, P. Energy Band-Gap Engineering of Graphene Nanoribbons. *Phys. Rev. Lett.* **98**, 206805 (2007).

63. Bhaviripudi, S., Jia, X., Dresselhaus, M. S. & Kong, J. Role of Kinetic Factors in Chemical Vapor Deposition Synthesis of Uniform Large Area Graphene Using Copper Catalyst. *Nano Lett.* **10**, 4128–4133 (2010).

64. Ago, H. *et al.* Epitaxial Chemical Vapor Deposition Growth of Single-Layer Graphene over Cobalt Film Crystallized on Sapphire. *ACS Nano* **4**, 7407–7414 (2010).

65. Kang, B. J., Mun, J. H., Hwang, C. Y. & Cho, B. J. Monolayer graphene growth on sputtered thin film platinum. *J. Appl. Phys.* **106**, (2009).

66. Sutter, P. W., Flege, J. I. & Sutter, E. A. Epitaxial graphene on ruthenium. *Nature Materials* vol. 7 406–411 (2008).

67. Li, X. *et al.* Large-Area Synthesis of High-Quality and Uniform Graphene Films on Copper Foils. *Science.* **324**, 1312–1314 (2009).

68. Huang, H., Chen, S., Wee, A. T. S. & Chen, W. Epitaxial growth of graphene on silicon carbide (SiC). in *Graphene* 3–26 (Elsevier, 2014). doi:10.1533/9780857099334.1.3.

69. Emtsev, K. V. *et al.* Towards wafer-size graphene layers by atmospheric pressure graphitization of silicon carbide. *Nature Materials* vol. 8 203–207 (2009).

70. Lauffer, P. *et al.* Atomic and electronic structure of few-layer graphene on SiC(0001) studied with scanning tunneling microscopy and spectroscopy. *Physical Review B - Condensed Matter and Materials Physics* vol. 77 (2008).
71hummers, W. S. & Offeman, R. E. Preparation of Graphitic Oxide. *J. Am. Chem. Soc.* **80**, 1339 (1958).
72. Zaaba, N. I. *et al.* Synthesis of Graphene Oxide using Modified Hummers Method: Solvent Influence. *Procedia Eng.* **184**, 469–477 (2017).
73 hummers, W. S. & Offeman, R. E. Preparation of Graphitic Oxide. *J. Am. Chem. Soc.* **80**, 1339–1339 (1958).
74. Morimoto, N. *et al.* Real-Time, in Situ Monitoring of the Oxidation of Graphite: Lessons Learned. *Chem. Mater.* **29**, 2150–2156 (2017).
75. Konios, D., Stylianakis, M. M., Stratakis, E. & Kymakis, E. Dispersion behaviour of graphene oxide and reduced graphene oxide. *J. Colloid Interface Sci.* **430**, 108–112 (2014).
76. Paredes, J. I., Villar-Rodil, S., Martínez-Alonso, A. & Tascón, J. M. D. Graphene Oxide Dispersions in Organic Solvents. *Langmuir* **24**, 10560–10564 (2008).
77. Schniepp, H. C. *et al.* Functionalized Single Graphene Sheets Derived from Splitting Graphite Oxide. *J. Phys. Chem. B* **110**, 8535–8539 (2006).
78. Chen, W., Yan, L. & Bangal, P. R. Preparation of graphene by the rapid and mild thermal reduction of graphene oxide induced by microwaves. *Carbon.* **48**, 1146–1152 (2010).
79. Alam, S. N., Sharma, N. & Kumar, L. Synthesis of Graphene Oxide (GO) by Modified Hummers Method and Its Thermal Reduction to Obtain Reduced Graphene Oxide (rGO)*. *Graphene* **06**, 1–18 (2017).
80. Sengupta, I., Chakraborty, S., Talukdar, M., Pal, S. K. & Chakraborty, S. Thermal reduction of graphene oxide: How temperature influences purity. *J. Mater. Res.* **33**, 4113–4122 (2018).
81. Li, Z. *et al.* Ultrafast, dry microwave synthesis of graphene sheets. *J. Mater. Chem.* **20**, 4781 (2010).
82. 1-s2.0-S0008622309007726-main.pdf.
83. Voiry, D. *et al.* High-quality graphene via microwave reduction of solution-exfoliated graphene oxide. *Science.* **353**, 1413–1416 (2016).
84. Gao, W., Alemany, L. B., Ci, L. & Ajayan, P. M. New insights into the structure and reduction of graphite oxide. *Nature Chemistry* vol. 1 403–408 (2009).
85. Stankovich, S. *et al.* Synthesis of graphene-based nanosheets via chemical reduction of exfoliated graphite oxide. *Carbon* vol. 45 1558–1565 (2007).
86. Chen, C., Kong, W., Duan, H.-M. & Zhang, J. Theoretical simulation of reduction mechanism of graphene oxide in sodium hydroxide solution. *Phys. Chem. Chem. Phys.* **16**, 12858 (2014).
87. Zhou, T. *et al.* A simple and efficient method to prepare graphene by reduction of graphite oxide with sodium hydrosulfite. *Nanotechnology* **22**, 045704 (2011).

88. Lee, J. W., Ko, J. M. & Kim, J.-D. Hydrothermal preparation of nitrogen-doped graphene sheets via hexamethylenetetramine for application as supercapacitor electrodes. *Electrochim. Acta* **85**, 459–466 (2012).
89. Shen, X. *et al.* Stable aqueous dispersions of graphene prepared with hexamethylenetetramine as a reductant. *J. Colloid Interface Sci.* **354**, 493–497 (2011).
90. Ding, H. *et al.* Reduction of graphene oxide at room temperature with vitamin C for RGO–TiO2 photoanodes in dye-sensitized solar cell. *Thin Solid Films* **584**, 29–36 (2015).
91. Fernández-Merino, M. J. *et al.* Vitamin C Is an Ideal Substitute for Hydrazine in the Reduction of Graphene Oxide Suspensions. *J. Phys. Chem. C* **114**, 6426–6432 (2010).
92. Zhang, J. *et al.* Reduction of graphene oxide via-ascorbic acid. *Chem. Commun.* **46**, 1112–1114 (2010).
93. Wentorf, R. H. Preparation of Semiconducting Cubic Boron Nitride. *J. Chem. Phys.* **36**, 1990–1991 (1962).
94. Sōma, T., Sawaoka, A. & Saito, S. Characterization of wurtzite type boron nitride synthesized by shock compression. *Mater. Res. Bull.* **9**, 755–762 (1974).
95. Bundy, F. P. & Wentorf, R. H. Direct Transformation of Hexagonal Boron Nitride to Denser Forms. *J. Chem. Phys.* **38**, 1144–1149 (1963).
96. Bhimanapati, G. R., Glavin, N. R. & Robinson, J. A. 2D Boron Nitride. in *Concise Encyclopedia of Self-Propagating High-Temperature Synthesis: History, Theory, Technology, and Products* 101–147 (2016). doi:10.1016/bs.semsem.2016.04.004.
97. Kim, G. *et al.* Growth of High-Crystalline, Single-Layer Hexagonal Boron Nitride on Recyclable Platinum Foil. *Nano Lett.* **13**, 1834–1839 (2013).
98. Pierucci, D. *et al.* Van der Waals epitaxy of two-dimensional single-layer h-BN on graphite by molecular beam epitaxy: Electronic properties and band structure. *Appl. Phys. Lett.* **112**, (2018).
99. Dean, C. R. *et al.* Boron nitride substrates for high-quality graphene electronics. *Nat. Nanotechnol.* **5**, 722–726 (2010).
100. Meng, J. H. *et al.* Synthesis of in-plane and stacked graphene/hexagonal boron nitride heterostructures by combining with ion beam sputtering deposition and chemical vapor deposition. *Nanoscale* **7**, 16046–16053 (2015).
101. Gul, S. *et al.* Design of Highly Thermally Conductive Hexagonal Boron Nitride-Reinforced PEEK Composites with Tailored Heat Conduction Through-Plane and Rheological Behaviors by a Scalable Extrusion. *ACS Appl. Polym. Mater.* **5**, 329–341 (2023).
102. Joy, J., George, E., Haritha, P., Thomas, S. & Anas, S. An overview of boron nitride based polymer nanocomposites. *J. Polym. Sci.* **58**, 3115–3141 (2020).
103. Izyumskaya, N. *et al.* Recent Development of Boron Nitride towards Electronic Applications. *Adv. Electron. Mater.* **3**, 125208–125208 (2017).
104. Xu, Y. N. & Ching, W. Y. Calculation of ground-state and optical properties of boron nitrides in the hexagonal, cubic, and wurtzite structures. *Physical Review B* vol. 44 7787–7798 (1991).

105. Pacilé, D., Meyer, J. C., Girit, Ç. Ö. & Zettl, A. The two-dimensional phase of boron nitride: Few-atomic-layer sheets and suspended membranes. *Appl. Phys. Lett.* **92**, (2008).
106. Alem, N. *et al.* Atomically thin hexagonal boron nitride probed by ultrahigh-resolution transmission electron microscopy. *Physical Review B - Condensed Matter and Materials Physics* vol. 80 (2009).
107. Lee, D. *et al.* Scalable Exfoliation Process for Highly Soluble Boron Nitride Nanoplatelets by Hydroxide-Assisted Ball Milling. *Nano Lett.* **15**, 1238–1244 (2015).
108. Lei, W. *et al.* Boron nitride colloidal solutions, ultralight aerogels and freestanding membranes through one-step exfoliation and functionalization. *Nat. Commun.* **6**, 1–8 (2015).
109. Chen, C. *et al.* Functionalized boron nitride membranes with ultrafast solvent transport performance for molecular separation. *Nat. Commun.* **9**, (2018).
110. Chen, X., Dobson, J. F. & Raston, C. L. Vortex fluidic exfoliation of graphite and boron nitride. *Chem. Commun.* **48**, 3703 (2012).
111. Yurdakul, H. *et al.* Nanoscopic characterization of two-dimensional (2D) boron nitride nanosheets (BNNSs) produced by microfluidization. *Ceram. Int.* **38**, 2187–2193 (2012).
112. Lin, Y. *et al.* Aqueous Dispersions of Few-Layered and Monolayered Hexagonal Boron Nitride Nanosheets from Sonication-Assisted Hydrolysis: Critical Role of Water. *J. Phys. Chem. C* **115**, 2679–2685 (2011).
113. Mittal, N., Kedawat, G., Kanika, Gupta, S. & Kumar Gupta, B. An Innovative Method for Large-Scale Synthesis of Hexagonal Boron Nitride Nanosheets by Liquid Phase Exfoliation. *ChemistrySelect* **5**, 12564–12569 (2020).
114. Sinitskii, A. *et al.* High-Yield Synthesis of Boron Nitride Nanoribbons via Longitudinal Splitting of Boron Nitride Nanotubes by Potassium Vapor. *ACS Nano* **8**, 9867–9873 (2014).
115. Zeng, H. *et al.* 'White graphenes': Boron nitride nanoribbons via boron nitride nanotube unwrapping. *Nano Letters* vol. 10 5049–5055 (2010).
116. Erickson, K. J. *et al.* Longitudinal Splitting of Boron Nitride Nanotubes for the Facile Synthesis of High Quality Boron Nitride Nanoribbons. *Nano Lett.* **11**, 3221–3226 (2011).
117. Takahashi, T., Itoh, H. & Kuroda, M. Structure and properties of CVD-BN thick film prepared on carbon steel substrate. *J. Cryst. Growth* **53**, 418–422 (1981).
118. Lee, J. S. *et al.* Wafer-scale single-crystal hexagonal boron nitride film via self-collimated grain formation. *Science.* **362**, 817–821 (2018).
119. Wang, L. *et al.* Epitaxial growth of a 100-square-centimetre single-crystal hexagonal boron nitride monolayer on copper. *Nature* vol. 570 91–95 (2019).

CHAPTER 2
Polyimide (PI) and PI composites : properties and applications

I. Introduction of polyimide

I.1history

PI is a polymer containing imide groups. It is primarily composed of polycondensed polymers derived from diamines and dianhydrides, which contain cyclic imide functional groups in the main chain. The typical structure is represented in Fig.1.

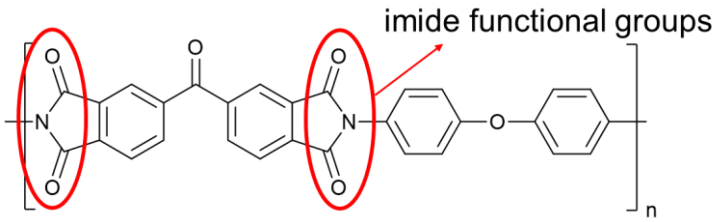

Fig. 1 The structures of polyimide. Circled in red are imide functional groups

PI was first discovered by Bogart and Renshaw in 1908.[1] They observed that the structure of 4-aminophthalic anhydride wouldn't melt when heated. Instead, it would undergo a dehydration reaction to produce PI. The reaction process is depicted in Fig. 2. The significance of PI grew in the 1950s during the space race. With the rapid advancements in aerospace science and technology, components needed heat-resistant properties.[2–4] This surge in aerospace technology created a demand for heat-resistant polymers, prompting significant investments in research and development of new polyimides.

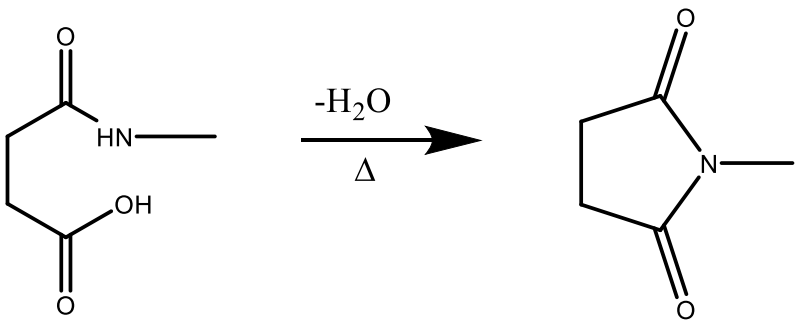

Fig. 2 Formation of imide functional group by amide-acid dehydration reactions

The all-aromatic PI was first successfully developed by E. I. du Pont de Nemours and Company (DuPont). Their approach primarily used aromatic diamines and aromatic dianhydrides as monomers, reacting in NMP polar solvents to obtain poly (amic acid) (PAA), the precursor of PI. This precursor

was then transformed into PI either through heating or chemical reactions. This method remains the dominant approach for producing most PIs to this day. Numerous studies have attested to PI's outstanding mechanical properties, high-temperature resistance, chemical resilience, and radiation resistance. Owing to these properties, PI is now extensively used in aviation equipment, battery protection films, heat-resistant films[2–4] for precision electronic instruments,[5–7] and other applications.

I.2 Type of PI

I.2.1 Condensed PI

Condensed PI synthesis primarily involves two stages. In the initial stage, bis anhydride compounds are polymerized in a polar organic solvent. Over time, this leads to the formation of a PI precursor known as PAA. In the subsequent stage, PAA undergoes dehydration to PI either by heat treatment or a chemical method.[8,9] The most notable PI produced this way is Kapton, manufactured by DuPont in the U.S.A., as illustrated in Fig. 3.

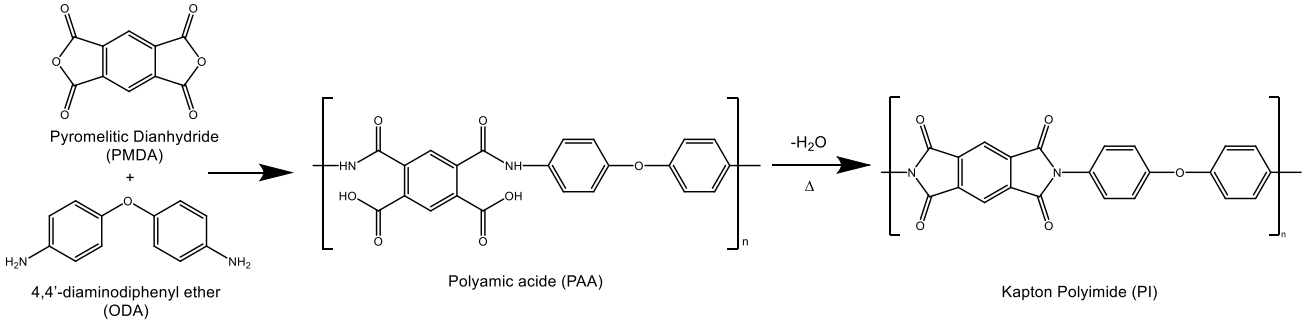

Fig. 3 The production of Kapton polyimide.

I.2.2 Addition of PI

Addition of polyimide is mainly produced through a two-stage synthesis method, which differs from the condensation type in that it consists of the polymerization of diamines, dianhydrides, and amine or anhydride compounds that contain double or reference bonds to produce a low molecular weight PAA, which is then imidated in the second step by heating or chemical method to form an imide polymer.[10–12] This method does not produce by-products such as moisture during hardening of the polyimide resin, making it easier to process and produce thicker products. However, since a mesh structure is formed

during the manufacturing process, the toughness of the polyimide resin is not as good as that of the shrinkage type. This production method is generally used in adhesives, printed circuit boards

I.2.3 Modified PI

Modified polyimides are chiefly crafted by inducing chemical changes to tailor specific applications or introduce novel functionalities. For instance, aliphatic groups can be integrated into the PI molecular chain to enhance the polymer's flexibility and solubility.[13–15] In 2019, Prof. Hayakawa's team successfully fabricated PI films averaging 19 nm nanopores by grafting other polymers following low-temperature heating (Fig. 4), paving the way for future innovative applications.[16]

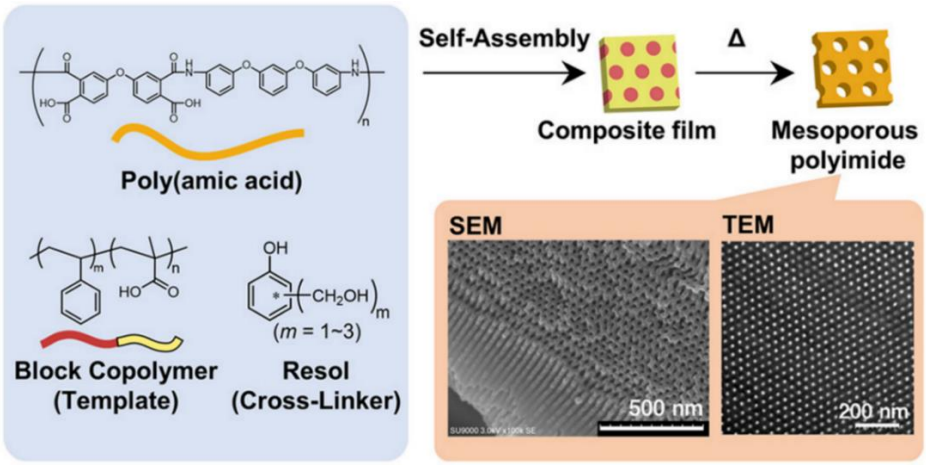

Fig. 4 Schematic illustration of the screening of PAAs synthesized from various monomers for PAA/F127 composite films and SEM image and TEM image. Reproduced with permission from Polymers for ACS Applied Polymer Materials[16]

In summary, condensed PI is the most straightforward to produce and enables commendable mechanical properties and heat resistance, its high melting temperature exceeds its structural decomposition temperature. Given its robust chemical resistance, most polyimides resist dissolution in conventional organic solvents, leading to processability challenges. Such complications can hamper applications. As a result, many opt to utilize PAA solutions to produce the desired products. However, owing to its structure, PAA is inherently unstable, necessitating moisture-proof storage at temperatures below 0 °C. During heating, temperatures between 250 and 350 °C are essential for complete

imidization.[8,9] This process releases moisture, inducing voids in the material, which can compromise the product's quality and application.

I.3 Characteristics of PI

PI is a material characterized by exceptional dimensional stability, maintaining a very low rate of dimensional change even within a temperature range of -25°C to 250°C. [17,18] Due to its excellent heat resistance properties, it remains functional in high temperature environments reaching up to 300 degrees. Additionally, PI possesses excellent insulating properties,[19,20] high mechanical properties,[21,22] low dielectric constant [5–7] and chemical resistance,[23–25] (Table 1 and Table 2). These attributes have increasingly led to its application in electronic products requiring signal transmission, such as circuit boards, heat-resistant gloves, aerogels, and semiconductor packaging materials.

Table 1 Literature data on the physical properties of PI

Items	Unit	Value
Thermal expansion coefficient[17,18]	ppm/°C	30~60
Decomposition temperature[2–4]	°C	400~500
Electrical resistance	Ω cm	10^{15}~10^{16}
Dielectric constant[5–7]	-	3~4
Tensile strength[21,22]	MPa	~89
Young modulus[21,22]	GPa	~2.1
Thermal conductivity[26,27]	W/m K	0.1

Table 2 Chemical properties of PI

Chemical resistance	Retention of strength (%)	Retention of elongation (%)	Retention of elastic modulus (%)	Test conditions
10% NaOH	85	80	105	5 days at 25 ℃
Glacial acetic acid	110	105	115	5 weeks at 110 ℃
p-Cresol	55	140	50	3 weeks at 200 ℃
Water PH = 1.0	100	90	110	2 weeks at 100 ℃
Water PH = 4.2	100	85	115	2 weeks at 100 ℃
Water PH = 8.9	105	90	115	2 weeks at 100 ℃
Water PH = 10.0	105	95	115	4 days at 100 ℃

I.4 Application of polyimide

I.4.1 Gas separation membranes

Over the past nearly 100 years, the explosive consumption of fossil fuel has led to global warming. This warming is primarily due to an excess of greenhouse gases, which continually absorb radiant heat from the sun, resulting in a consistent rise in global temperatures. Major greenhouse gases include H_2O, CO_2, CH_4, O_3, and N_2O.[28,29] The effective separation and subsequent recycling of specific gases have become crucial. Many studies have shown that the unique structure (dianhydride and diamine) of polyimide (PI) films results in much better separation compared to traditional membranes. By controlling the components of dianhydride and diamine, the permeability and gas selectivity can be altered (Fig. 5).[30,31] However, controlling the molecular composition and the way they intertwine is challenging, and the length of the molecular chain connections can compromise inherent physical properties such as mechanical strength, heat resistance, and chemical resistance. New methods are still needed to develop films that do not compromise these properties.

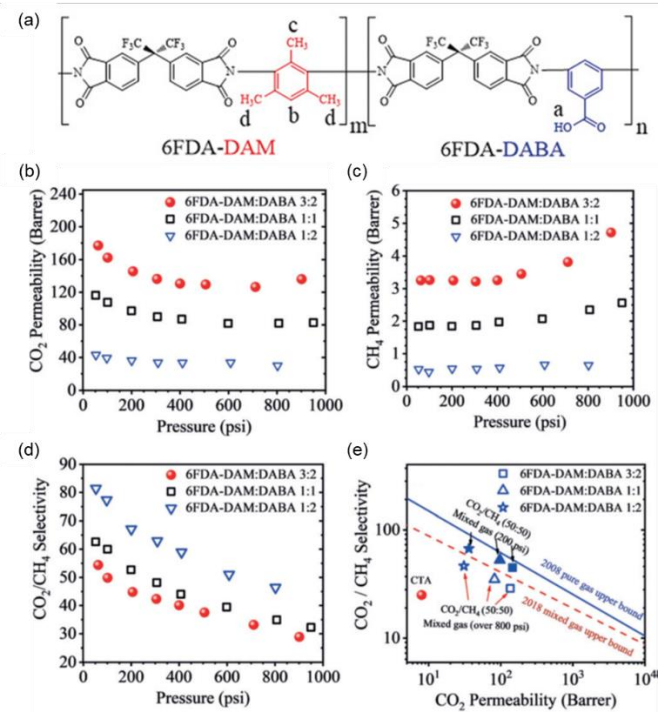

Fig. 5 (a) The structure of polyimide membranes. (b) CO_2 permeability (c) CH_4 permeability. (d) permeability of 6FDA-DAM:-DABA membranes for 50/50 CO_2/CH_4. (e) CO_2/CH_4 separation performance comparison of 6FDA-DAM:DABA membranes. Reproduced with permission from Angewandte Chemie.[30]

I.4.2 Battery separators

Due to the over-reliance on petroleum energy in recent years, there has been significant emission of greenhouse gases and harmful gases, leading to increasingly severe global climatic and environmental issues. To reduce reliance on petroleum energy, the challenge of energy storage and reuse arises. To date, lithium-ion batteries are the most popular and efficient, but as their energy density increases, safety concerns become paramount. Therefore, the separators between the electrodes need to have high heat resistance, good mechanical properties, and electrochemical stability. Previous research indicates that polyimide films are effective, and after a simple alkaline hydrolysis reaction on the PI surface, the ionic transport performance can be effectively improved, [32–34] further enhancing the battery capacity (Fig. 6).[35] However, due to the production costs of PI, it has not yet been widely adopted.

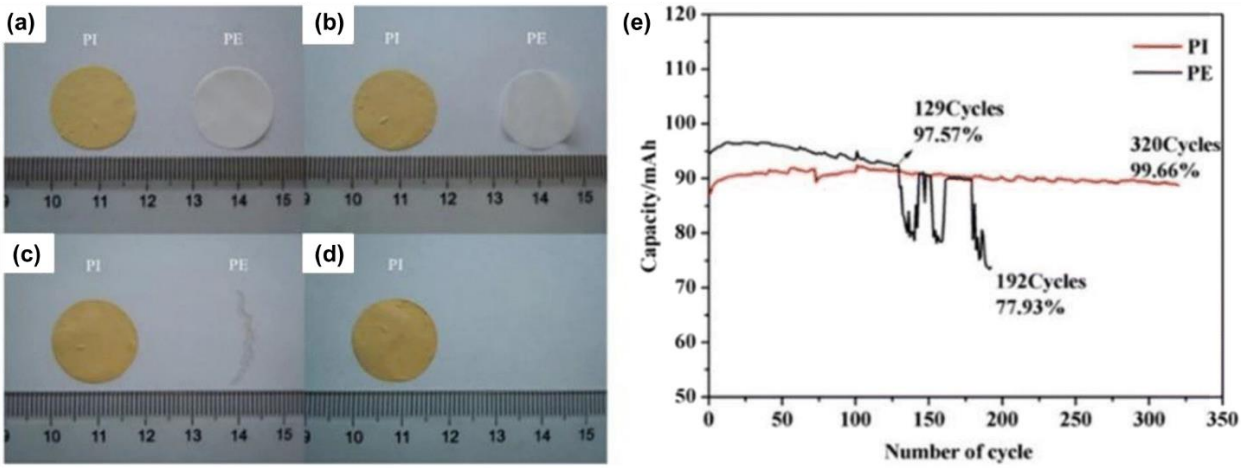

Fig. 6 (a-d) Thermal stability test of PE and PI separator. (a) Before heating. (b)150 °C. (c) 250 °C. (d) 500 °C. (e) Cycle test at 5C. Reproduced with permission from Journal of Electroanalytical Chemistry[35]

I.4.3 Aerogels

During the space race in the 1950s, various satellites and space stations were launched. These satellites have greatly assisted in communication and location tracking for humans. However, many tiny particles orbit rapidly around the Earth in space. When these particles collide with satellite instruments, they can cause immeasurable damage, potentially destroying the equipment. To prevent such damage, aerogels are used to block these tiny space particles. Aerogels have properties including extremely low density, excellent heat resistance, and remarkable insulation character.[36,37] Currently, aerogels are mainly composed of silica dioxide and metal oxides.[38] In the recent years, polymer materials have been explored as a potential alternative, indeed, PI has good mechanical properties and thermal stability, which makes it a very promising choice. In 2011, Mary Ann B. Meadorm team's successfully produced PI aerogel by supercritical drying (Fig. 7a). It has a low density (0.14g cm^{-1}) and very good heat resistance (decomposition above 600 °C) (Fig. 7b and c). However, supercritical drying is very complicated and takes a long time to produce.[39] In 2019, Wang and her team used freezing water to form a porous structure within PAA. They then transformed the PAA frozen gel fibers into PI aerogel fibers through heat imidization.[40] The aerogels produced by this method have larger pore sizes, resulting in a higher surface area and conductivity coefficient than regular aerogels.

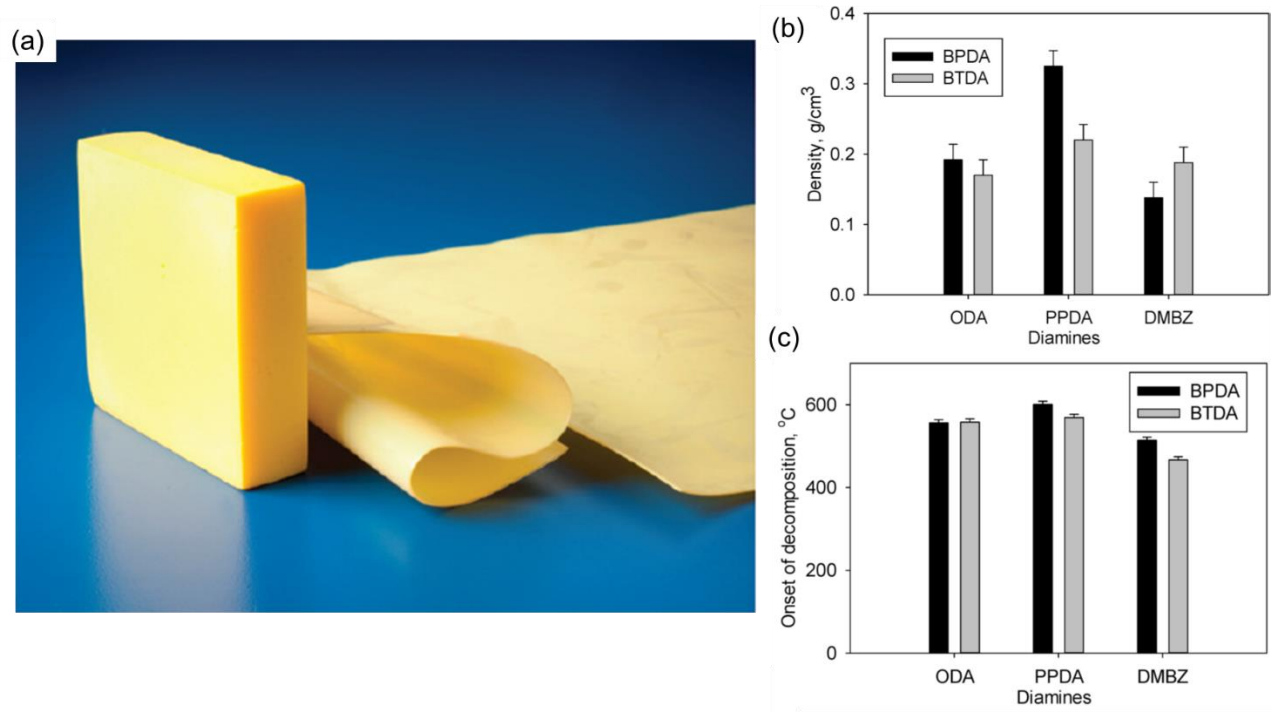

Fig. 7 (a)Polyimide aerogels. (b)Polyimide aerogels average density. (c)Average onset of decomposition as measured by TGA in nitrogen. Reproduced with permission from ACS Applied Materials & Interfaces.[39]

I.5 Application of PI/2D materials composites

Owing to the excellent properties and special structure of PI, there are many applications, but the performance of using polyimide alone or modifying the molecular structure of polyimide is still insufficient for some applications. In order to enhance the properties of polyimide, people began to add nano fillers to polyimide. Currently, the common filler materials are black carbon, nanocarbon tubes, fuller's glass, graphene oxide, and so on. In recent years, due to the special structure and physical properties of 2D materials, as long as a small amount is added to polyimide, the physical properties will be improved. For example, mechanical properties, thermal conductivity, electrical conductivity, dielectric coefficient, etc. Therefore, the following chapter will focus on the application of PI/GO and PI/BN composites.

I.6 Application of PI/GO

I.6.1 Gas separation membranes

In the aforementioned applications of PI, it is noted that gas separation can be controlled by manipulating molecular structures. However, controlling molecular composition and intertwining patterns is challenging, leading to a decline in the inherent physical properties. Due to GO ability to separate CO_2 and N_2,[41] attempts have been made to enhance membrane gas separation by incorporating GO into PI. In 2015, studies indicated that increasing the oxidation level of GO enhances the permeability and selectivity of composite membranes. However, these properties decrease with higher amounts of added GO. When the GO content reaches 1 wt%, maximum permeability and selectivity increase to 14.3 times and 4.2 times, respectively (Fig. 8).[42] Yet, this method is complex, challenging to control, and can reduce the active surface area. In 2018, Bao-Sheng Ge's research team synthesized amidated GO through the reaction of GO with ethylenediamine (EDA) and added it to PI films. GO-EDA amino groups interact with CO_2, enhancing permeability and selectivity. With a 3 wt% addition, CO_2/N_2 selectivity reaches 38.56 (Table 1).[43]

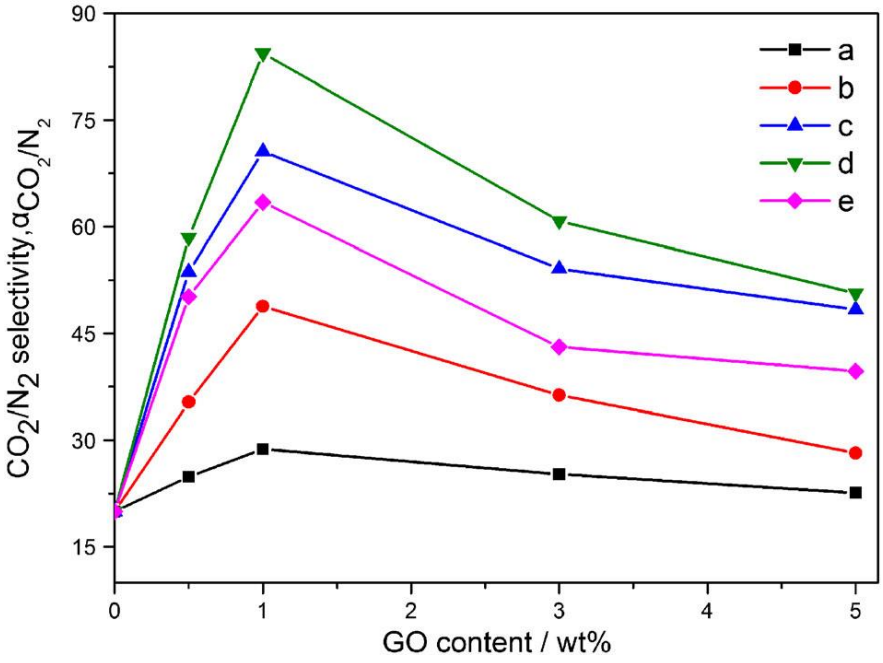

Fig. 8 Permeation selectivity of GO/PI mixed matrix membranes for CO_2/N_2 gas mixture: a GO/PI-1, b GO/PI-2, c GO/PI-3, d GO/PI-4, and e GO/PI-5. Reproduced with permission from Polymers for Advanced Technologies[42]

Table 1 Permeability of pure gases and CO_2/N_2 ideal selectivity through PI/GO MMMs at T = 15°C, feed pressure = 0.1 MPa. Reproduced with permission from Polymers for Advanced Technologies[43]

Type of Membrane	GO Content, wt%	Permeability, Barrer		Selectivity
		CO_2	N_2	CO_2/N_2
PI/GO MMMs	0	2.3	0.15	15.33
	1	4.53	0.19	23.84
	2	6.52	0.21	30.05
	3	8.16	0.23	35.48
	4	7.28	0.21	34.67
PI/NH_2-GO MMMs	0	2.3	0.15	15.33
	1	5.98	0.21	28.48
	2	9.04	0.25	36.16
	3	12.34	0.32	38.56
	4	10.21	0.31	32.94

I.6.2 High thermal conductivity film

The thermal conductivity of PI is only about 0.1W m^{-1} K^{-1},[26,27] which cannot satisfy the requirement of rapid thermal conductivity of advanced electronic instruments. In order to improve the thermal conductivity, researchers started to be attracted to the excellent thermal conductivity of graphene. However, the thermal conductivity of PI composites has not been improved much because of the random arrangement of graphene when it is dispersed in PAA solution. In order to solve the problem of heterogeneity, a study has been conducted to arrange rGO inside PI by freeze-drying method. From the results, it was found that the thermal conductivity could reach 2.78 W m^{-1} K^{-1} (15.4 times higher than that of PI and 5.5 times higher than that of conventional products) when the addition of rGO reached 8 wt% (Fig. 9a-e).[44] The surface modification of graphene fluoride (GeF) two-dimensional insulating material was also studied to effectively increase the thermal conductivity to 2.11 W m^{-1} K^{-1}(Fig. 9f and g),[45] which also indicates that the functionalized graphene and composite film fabrication method can effectively improve the thermal conductivity of PI.

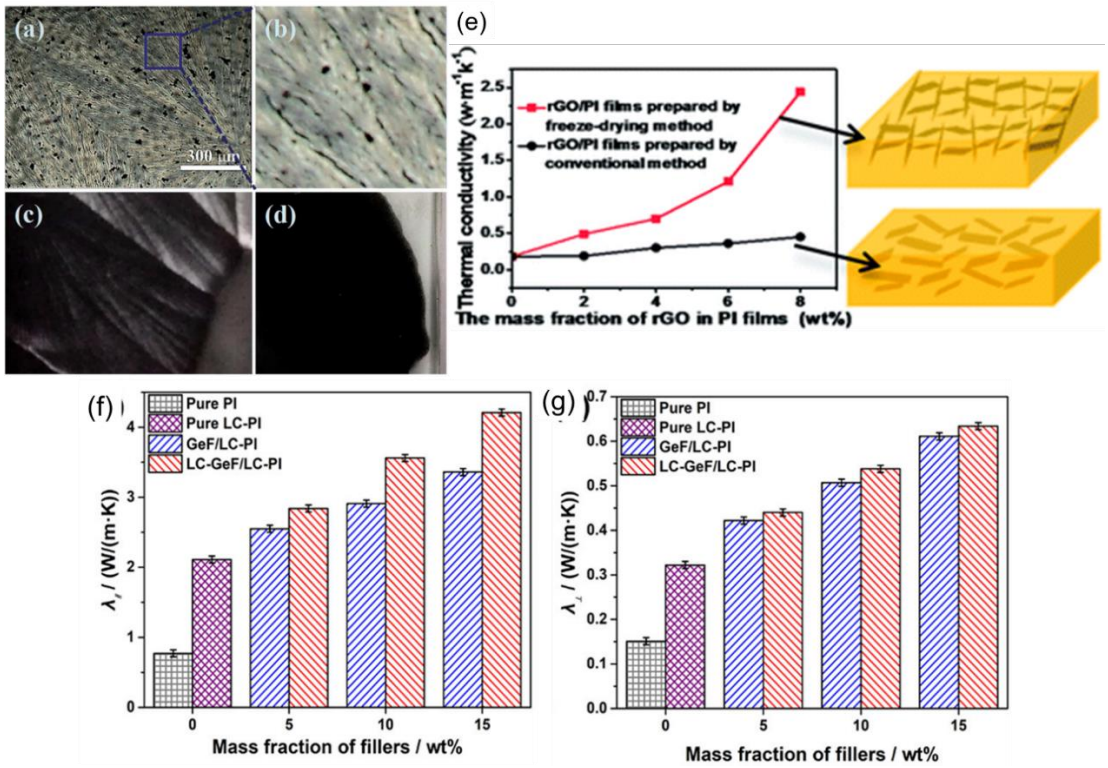

Fig. 9 (a-d) POM diagram of rGO/PAA (a) At low magnification, (b) at high magnification. (c) PAA photos after 12 hours of freezing (d) PAA film after freezing and drying solvent treatment (e) Effect of filler content on the thermal conductivities of rGO/PI composite films. Reproduced with permission from RSC Advances.[44] (f) LC-GeF/LC-PI horizontal orientation thermal conductivity. (g) LC-GeF/LC-PI vertical orientation thermal conductivity Reproduced with permission from Macromolecules.[45]

I.6.3 Battery separators

PI nanofiber membrane has high porosity and excellent heat resistance, it has great potential as a lithium-ion battery separator. However, the performance is still unsatisfactory. Studies points out that the mechanical properties, thermal stability and electrochemical properties of PI nanofiber membrane can be improved by adding GO.[46,47] The enhancement of these properties is crucial for the safety of future lithium-ion battery.

I.6.4 High strength and low dielectric constant film

With the rapid development of electronic equipment in recent years, the requirements for materials with low dielectric coefficient and good mechanical properties are getting higher and higher. Although PI has good mechanical properties, the dielectric coefficient is around 3~4, which is a disadvantage

for communication equipment, require a dielectric constant close to that of PTFE <2.1. In 2011, Chen-Chi M. Ma and his research team eacted GO with 4,4'-Diaminodiphenyl Ether (ODA) to produce amine-functionalized GO,and successfully prepared PI-ODA -GO composite films by in situ polymerization. With 5 wt% of ODA-GO, the tensile strength and tensile modulus increase to 728 MPa and 19.6 GPa, respectively, and the dielectric constant decreases to 2.0 Fig. 10.[48] In 2014, the same team added polyhedral oligomeric silsesquioxane (POSS) containing POSS functionalized with GO to the PI films. As a result, the mechanical properties and dielectric coefficients of the PI films were improved.[49] This shows that the functionalized GO not only provides a link to the PI, but also reduces the internal energy loss.

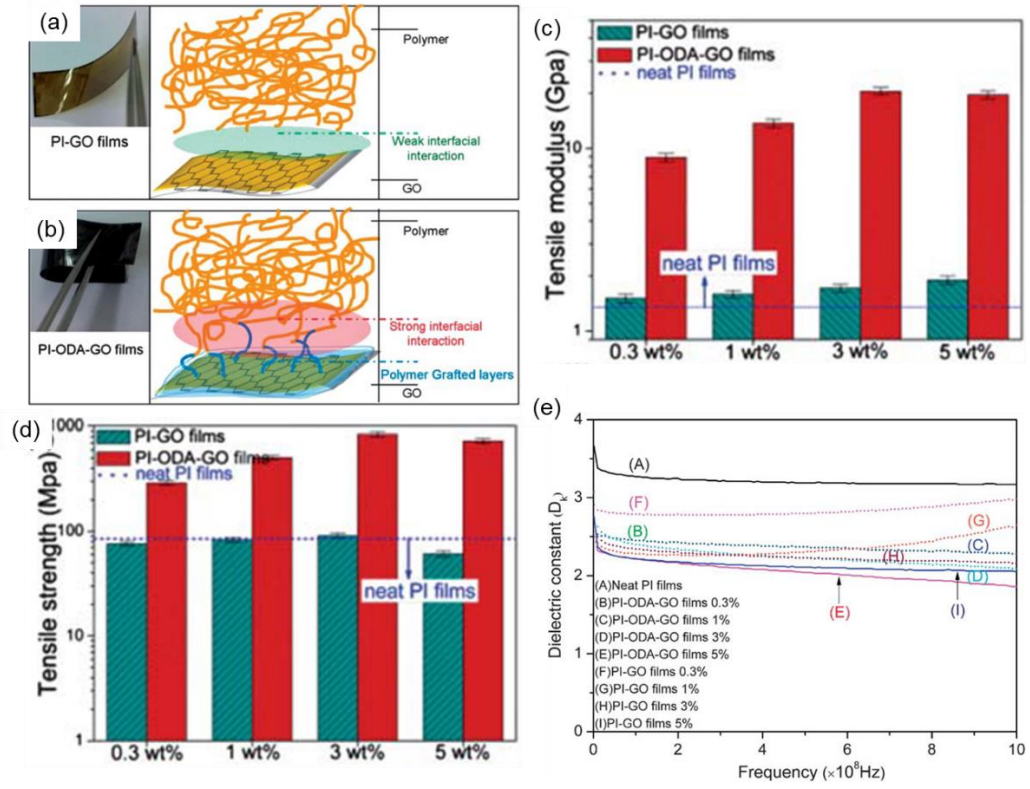

Fig. 10 (a-b) The proposed model of the interphase structure of (a) PI–GO films and (b) PI–ODA-GO films,(c) Tensile modulus, (d) tensile strength, (e) Dielectric constant of neat PI film, PI–GO films and PI–ODA-GO films Reproduced with permission from Journal of Materials Chemistry[48]

I.6.5 Aerogels

The above-mentioned PAA freeze-dried gel fibers, after undergoing thermal amidation, transform into PI aerogel fibers. However, aerogels produced through this method have excessively large pore sizes, leading to higher specific surface area and thermal conductivity compared to regular aerogels. In 2015, Edwin Hang Tong Teo and his research team developed a hybrid material comprising PI and 3D graphene.[49] This composite exhibits excellent thermal conductivity (an order of magnitude higher than PI) and electrical conductivity (ten orders of magnitude). Under bending, thermal cycling, and simulated space environment conditions, it demonstrates remarkable stability. In 2020, Pengbo Liu's research team successfully prepared anisotropic PI/GO composite aerogels using a unidirectional freeze-casting method, as shown in Fig. 11.[50] These composite aerogels have low density (0.0076 g cm^{-3}), outstanding thermal stability (decomposition temperature starting in a nitrogen atmosphere at 546°C), and excellent electromagnetic wave shielding properties (26.1–28.8 dB·). They offer significant advantages for future aerospace electromagnetic interference (EMI) shielding materials.

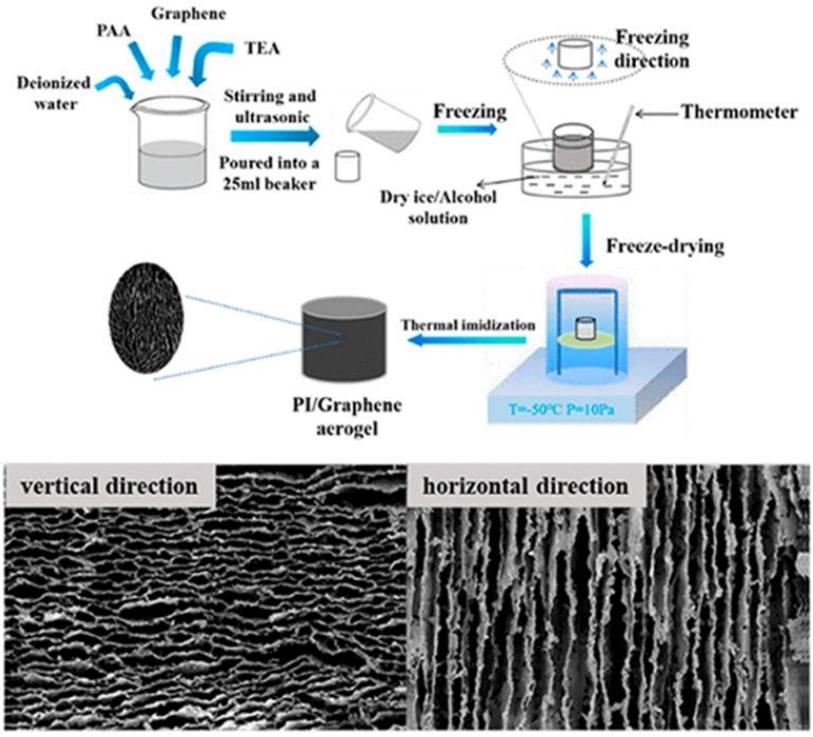

Fig. 11 Preparation of PI/graphene composite aerogels. Reproduced with permission from ACS Applied Materials & Interfaces[50]

I.7 Application of PI/BN

I.7.1 Gas separation membranes

The excellent physical properties of BN and its complementary unique features with graphene have attracted significant attention. In 2018, Yuqi Wang demonstrated that amino-functionalized boron nitride nanosheets (FBN) as a filler in PI significantly enhanced tensile strength by 282% and exhibited excellent selectivity for H_2 (Fig. 12).[50] This development holds promise for future hydrogen fuel cell applications.

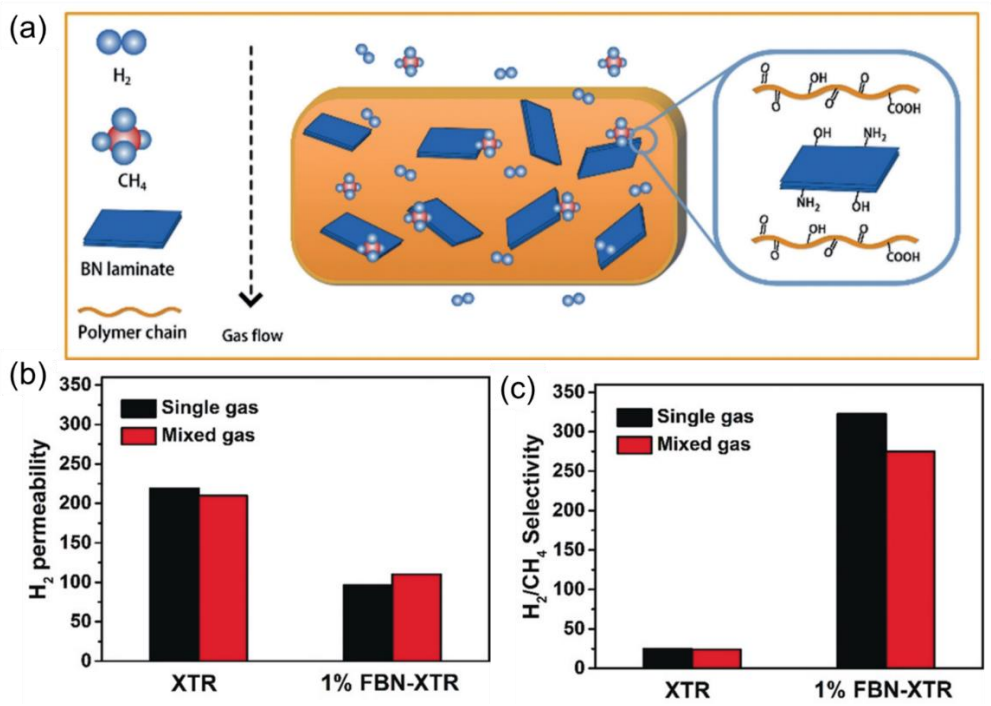

Fig. 12 (a) Schematic illustration of the structure of FBN-XTR membrane and selective gas permeation through the membrane. (b) H_2 permeability and (c) H_2/CH_4 selectivity of XTR and 1 wt% FBN-XTR membrane measured with single and mixed gas permeation experiments. Reproduced with permission from Angewandte Chemie[50]

I.7.2 High thermal conductivity films

h-BN has very good thermal conductivity (550 W m^{-1} k^{-1})[51,52] which is very close to graphene, and has been emphasized for its structural stability and excellent high temperature resistance. It is pointed out that the surface-modified h-BN in micron and nanometer sizes are added to PI in different ratios

to form a composite film.[53] When the ratio of micron- to nanometer-sized surface-modified h-BN is 7:3 and the addition amount reaches 30 wt%, the thermal conductivity coefficient reaches 1.2 W m^{-1} k^{-1} (about 10 times that of PI). The micron-sized h-BN is the main thermal conductivity path in PI, and the nano-sized h-BN particles act as a link between the micron-sized particles to increase contact and thus enhance the thermal conductivity. However, when the surface is modified, the crystallinity of h-BN will be changed, resulting in a decrease in thermal conductivity. In order to maintain the high crystallinity, it has been reported that h-BN edge can be functionalized and then added to PI to form a composite film, which effectively improves the thermal conductivity of the film. When the h-BN amount reaches 60 wt%, the thermal conductivity coefficient can reach 7 $Wm^{-1}k^{-1}$, which is 70 times higher than that of PI (Fig. 13).[54] It will be helpful for the application of heat exhaust system of electronic products in the future.

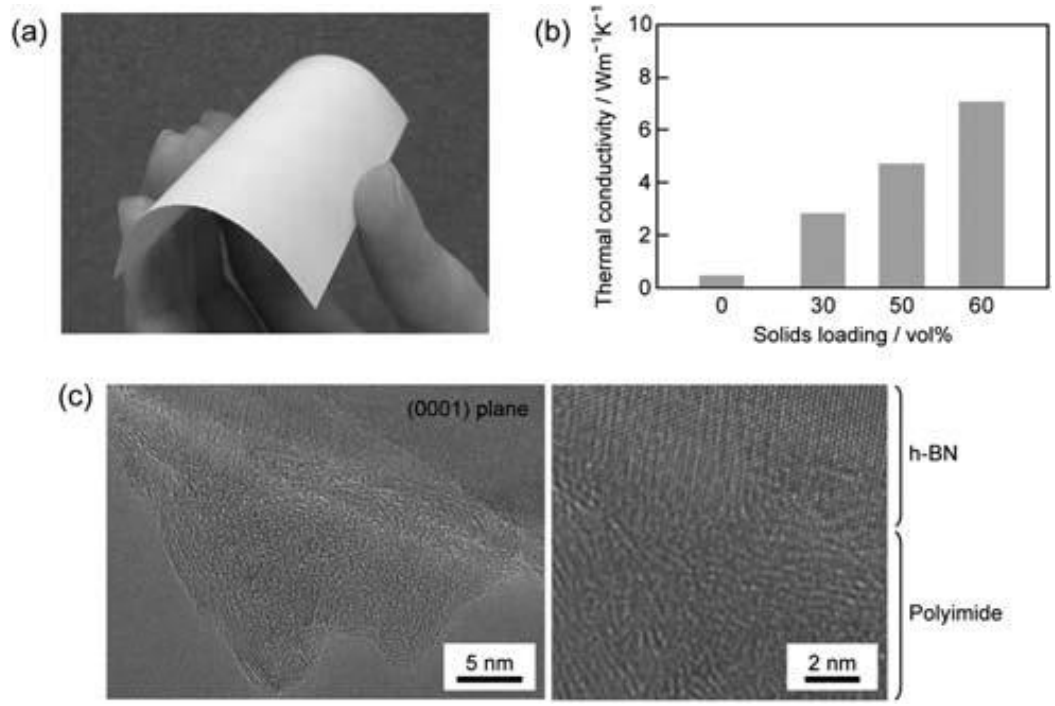

Fig. 13 Obtained h-BN/polyimide composite films. (a) Photograph of the composite film with 60 vol% solids loading. (b) Effect of filler content on thermal conductivity. (c) TEM images of the interface between h-BN filler and polyimide in the composite film. Reproduced with permission from J Mater Chem.[54]

I.7.3 Aerogels

h-BN possesses excellent thermal conductivity, thermal stability, and good mechanical properties, making it a potential filler for polymer materials. In 2019, Weiwei Lei and his research team, through a simple ball milling process, functionalized edge-hydroxylated h-BN (FBN) and added it to PAA, forming a PAA composite. After heating, FBN-PI aerogels were formed through freeze-drying (Fig. 14).[55] The resulting aerogel had very low density (6.5 mg cm^{-3}) and exhibited excellent thermal conductivity, thermal stability, and mechanical properties. Even at high temperatures, FBN-PI aerogels showed remarkable compression resilience. In 2022, Qinghong Zhai developed BNNSs/PI foam composite materials with a filling amount of 12 wt%. After 10,000 cycles of 60% compression strain, the total strain loss was 14% (2/3 of pure PI).[56] This offers a potential pathway for lightweight materials in the fields of thermal energy and compression sensors in the future.

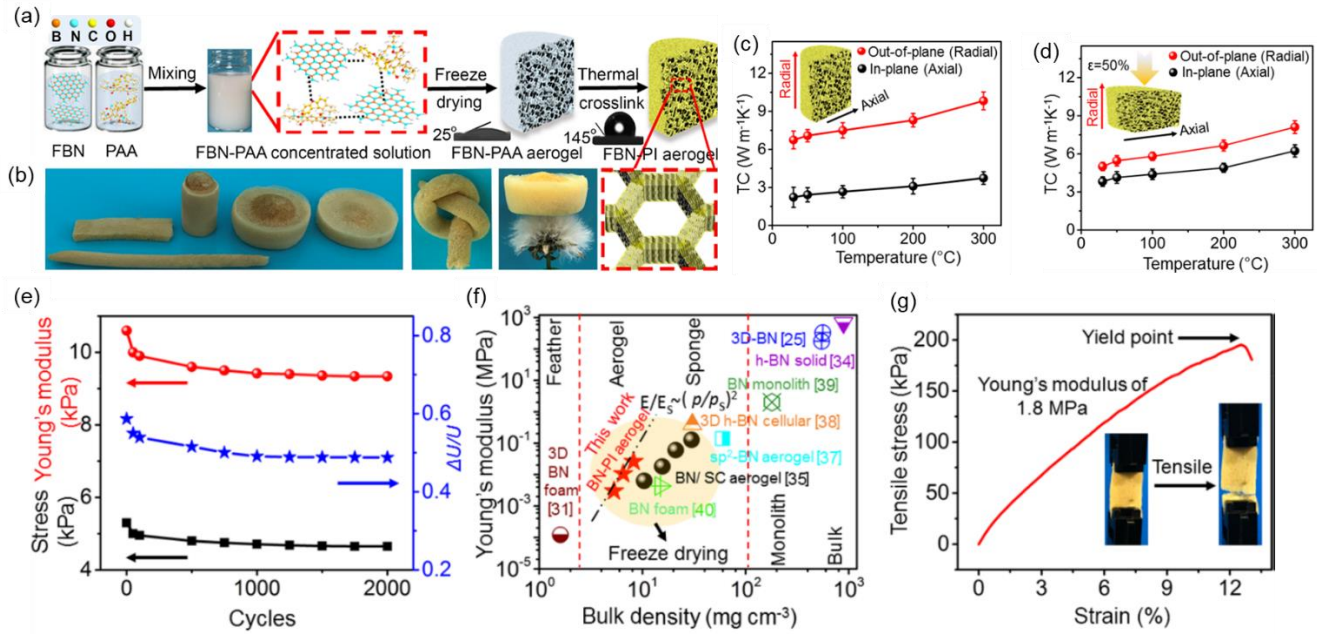

Fig. 14 (a) Schematic illustration of the fabrication process of FBN-PI aerogel. (b) Digital photographs of FBN-PI aerogels with different shapes, under knot and floating on the flower stamen. (c) The thermal conductivities of FBN-PI-2 aerogel without compression at different temperatures. (d) The thermal conductivities of FBN-PI-2 aerogel at different temperatures. (e) The relationships between compressive Young's modulus and bulk density of BN-PI aerogels and other reported BN-based 3D structures. (f) Tensile stress−strain curve of the FBN-PI-2 aerogel. (g) A set of digital images show the normal compression and recovering process of FBN-PI-2 aerogel. Reproduced with permission from ACS Nano[55]

II CONCLUSIONS

The above introduction shows that employing only GO or h-BN has a filler allows the preparation of PI with enhanced properties, making such PI composites holding great potentials for tomorrow's electronic application.

In order to increase the range of application of PI composites, the research in this thesis is devoted to explore and find new functionalization methods for the complex dual introduction of additive materials, including GO and h-BN, and to clearly understand the synthesis principles, characterize its chemical and physical properties, and to investigate its potential applications.

REFERENCES

1. Bogert, M. T. & Renshaw, R. R. 4-AMINO-0-PHTHALIC ACID AND SOME OF ITS DERIVATIVES. 1. *J Am Chem Soc* **30**, 1135–1144 (1908).
2. Serafini, T. T., Delvigs, P. & Lightsey, G. R. Thermally stable polyimides from solutions of monomeric reactants. *J Appl Polym Sci* **16**, 905–915 (1972).
3. Liaw, D.-J., Chang, F.-C., Leung, M., Chou, M.-Y. & Muellen, K. High Thermal Stability and Rigid Rod of Novel Organosoluble Polyimides and Polyamides Based on Bulky and Noncoplanar Naphthalene−Biphenyldiamine. *Macromolecules* **38**, 4024–4029 (2005).
4. Pramoda, K. P., Chung, T. S., Liu, S. L., Oikawa, H. & Yamaguchi, A. Characterization and thermal degradation of polyimide and polyamide liquid crystalline polymers. *Polym Degrad Stab* **67**, 365–374 (2000).
5. Li, J. *et al.* Synthesis and properties of ultralow dielectric constant porous polyimide films containing trifluoromethyl groups. *J Appl Polym Sci* **134**, (2017).
6. Chern, Y.-T. Low Dielectric Constant Polyimides Derived from Novel 1,6-Bis[4-(4-aminophenoxy)phenyl]diamantane. *Macromolecules* **31**, 5837–5844 (1998).
7. Simpson, J. O. & St.Clair, A. K. Fundamental insight on developing low dielectric constant polyimides. *Thin Solid Films*, **308-309**, 480-485, (1997)
8. Ogieglo, W., Wormeester, H., Eichhorn, K. J., Wessling, M. & Benes, N. E. In situ ellipsometry studies on swelling of thin polymer films: A review. *Prog Polym Sci* **42**, 42–78 (2015).
9. Kong, J. Y. *et al.* Preparation and properties of polyimide/graphene oxide nanocomposite films with Mg ion crosslinker. *Eur Polym J* **48**, 1394–1405 (2012).
10. Arrington, C. B. *et al.* Supramolecular Salts for Additive Manufacturing of Polyimides. *ACS Appl Mater Interfaces* **13**, 48061–48070 (2021).

11. Sarbolouki, M. N. Properties of asymmetric polyimide ultrafiltration membranes. I. Pore size and morphology characterization. *J Appl Polym Sci* **29**, 743–753 (1984).
12. Kawakami, H., Mikawa, M. & Nagaoka, S. Gas Transport Properties of Asymmetric Polyimide Membrane with an Ultrathin Surface Skin Layer. *Macromolecules* **31**, 6636–6638 (1998).
13. XIAO, Y., CHUNG, T., GUAN, H. & GUIVER, M. Synthesis, cross-linking and carbonization of co-polyimides containing internal acetylene units for gas separation. *J Memb Sci* **302**, 254–264 (2007).
14. Liu, Y. *et al.* Well-ordered mesoporous polymers and carbons based on imide-incorporated soft materials. *Polym. Chem.* **5**, 6452–6460 (2014).
15. Kim, H. J., Park, Y. J., Choi, J., Han, H. S. & Hong, Y. T. Surface modification of polyimide film by coupling reaction for copper metallization. *Journal of Industrial and Engineering Chemistry* **15**, 23–30 (2009).
16. Komamura, T., Okuhara, K., Horiuchi, S., Nabae, Y. & Hayakawa, T. Fabrication of Well-Ordered Mesoporous Polyimide Films by a Soft-Template Method. *ACS Appl Polym Mater* **1**, 1209–1219 (2019).
17. Liou, G., Lin, P., Yen, H., Yu, Y. & Chen, W. Flexible nanocrystalline-titania/polyimide hybrids with high refractive index and excellent thermal dimensional stability. *J Polym Sci A Polym Chem* **48**, 1433–1440 (2010).
18. Tseng, I. H., Liao, Y. F., Chiang, J. C. & Tsai, M. H. Transparent polyimide/graphene oxide nanocomposite with improved moisture barrier property. *Materials Chemistry and Physics* vol. 136 247–253 Preprint at https://doi.org/10.1016/j.matchemphys.2012.06.061 (2012).
19. Li, H., Liu, G., Liu, B., Chen, W. & Chen, S. Dielectric properties of polyimide/Al2O3 hybrids synthesized by in-situ polymerization. *Mater Lett* **61**, 1507–1511 (2007).
20. Sessler, G. M., Hahn, B. & Yoon, D. Y. Electrical conduction in polyimide films. *J Appl Phys* **60**, 318–326 (1986).
21. Chen, Y. & Iroh, J. O. Synthesis and Characterization of Polyimide/Silica Hybrid Composites. *Chemistry of Materials* **11**, 1218–1222 (1999).
22. Bell, V. L., Stump, B. L. & Gager, H. Polyimide structure–property relationships. II. Polymers from isomeric diamines. *Journal of Polymer Science: Polymer Chemistry Edition* **14**, 2275–2291 (1976).
23. Takahashi, Y., Iijima, M., Inagawa, K. & Itoh, A. Synthesis of aromatic polyimide film by vacuum deposition polymerization. *Journal of Vacuum Science & Technology A: Vacuum, Surfaces, and Films* **5**, 2253–2256 (1987).
24. Sugimoto, E. Applications of Polyimide Films to the Electrical and Electronic Industries in Japan. *IEEE Electrical Insulation Magazine* vol. 5 15–23 Preprint at https://doi.org/10.1109/57.16949 (1989).
25. Ding, M. *et al.* Comparative study on polyimides from 3,3-and 4,4-linked diphthalic anhydride. *J Appl Polym Sci* **59**, 923–930 (1996).

26. Wei, S. *et al.* Fabricating high thermal conductivity rGO/polyimide nanocomposite films via a freeze-drying approach. *RSC Adv* **8**, 22169–22176 (2018).
27. Li, T.-L. & Hsu, S. L.-C. Enhanced Thermal Conductivity of Polyimide Films via a Hybrid of Micro- and Nano-Sized Boron Nitride. *J Phys Chem B* **114**, 6825–6829 (2010).
28. Olivier, J. G. J., Bouwman, A. F., Van Der Hoek, K. W. & Berdowski, J. J. M. Global air emission inventories for anthropogenic sources of NO(x), NH3 and N2O in 1990. *Environmental Pollution* vol. 102 135–148 Preprint at https://doi.org/10.1016/S0269-7491(98)80026-2 (1998).
29. Kampa, M. & Castanas, E. Human health effects of air pollution. *Environmental Pollution* **151**, 362–367 (2008).
30. Liu, Z., Liu, Y., Qiu, W. & Koros, W. J. Molecularly Engineered 6FDA-Based Polyimide Membranes for Sour Natural Gas Separation. *Angewandte Chemie International Edition* **59**, 14877–14883 (2020).
31. Wang, Z., Wang, D., Zhang, F. & Jin, J. Tröger's Base-Based Microporous Polyimide Membranes for High-Performance Gas Separation. *ACS Macro Lett* **3**, 597–601 (2014).
32. Yu, H. *et al.* Recent developments of polyimide materials for lithium-ion battery separators. *Ionics* vol. 27 907–923 Preprint at https://doi.org/10.1007/s11581-020-03865-2 (2021).
33. Choi, J. *et al.* Highly stable porous polyimide sponge as a separator for lithium-metal secondary batteries. *Nanomaterials* vol. 10 1–15 Preprint at https://doi.org/10.3390/nano10101976 (2020).
34. Lu, Z. *et al.* Polyimide separators for rechargeable batteries. *Journal of Energy Chemistry* vol. 58 170–197 Preprint at https://doi.org/10.1016/j.jechem.2020.09.043 (2021).
35. Cao, L., An, P., Xu, Z. & Huang, J. Performance evaluation of electrospun polyimide non-woven separators for high power lithium-ion batteries. *Journal of Electroanalytical Chemistry* **767**, 34–39 (2016).
36. Kistler, S. S. Coherent Expanded-Aerogels. *J Phys Chem* **36**, 52–64 (1932).
37. KISTLER, S. S. Coherent Expanded Aerogels and Jellies. *Nature* **127**, 741–741 (1931).
38. Pekala, R. W. Organic aerogels from the polycondensation of resorcinol with formaldehyde. *Journal of Materials Science* vol. 24 3221–3227 Preprint at https://doi.org/10.1007/BF01139044 (1989).
39. Meador, M. A. B. *et al.* Mechanically Strong, Flexible Polyimide Aerogels Cross-Linked with Aromatic Triamine. *ACS Appl Mater Interfaces* **4**, 536–544 (2012).
40. Wang, Y. *et al.* Multifunctional polyimide aerogel textile inspired by polar bear hair for thermoregulation in extreme environments. *Chemical Engineering Journal* **390**, 124623 (2020).
41. Kim, H. W. *et al.* Selective Gas Transport Through Few-Layered Graphene and Graphene Oxide Membranes. *Science (1979)* **342**, 91–95 (2013).
42. Zhao, L. *et al.* Enhancement on the permeation performance of polyimide mixed matrix membranes by incorporation of graphene oxide with different oxidation degrees. *Polym Adv Technol* **26**, 330–337 (2015).

43. Ge, B., Wang, T., Sun, H., Gao, W. & Zhao, H. Preparation of mixed matrix membranes based on polyimide and aminated graphene oxide for CO 2 separation. *Polym Adv Technol* **29**, 1334–1343 (2018).
44. Wei, S. *et al.* Fabricating high thermal conductivity rGO/polyimide nanocomposite films via a freeze-drying approach. *RSC Adv* **8**, 22169–22176 (2018).
45. Ruan, K. & Gu, J. Ordered Alignment of Liquid Crystalline Graphene Fluoride for Significantly Enhancing Thermal Conductivities of Liquid Crystalline Polyimide Composite Films. *Macromolecules* **55**, 4134–4145 (2022).
46. Song, K. *et al.* Electrospun PI@GO separators for Li-ion batteries: a possible solution for high-temperature operation. *Journal of Sol-Gel Science and Technology* vol. 94 109–117 Preprint at https://doi.org/10.1007/s10971-019-05063-7 (2020).
47. Tian, Q. *et al.* Fabrication of Aligned PI/GO Nanofibers for Battery Separators. *Fibers and Polymers* vol. 22 30–35 Preprint at https://doi.org/10.1007/s12221-021-0103-1 (2021).
48. Wang, J.-Y. *et al.* Preparation and properties of graphene oxide/polyimide composite films with low dielectric constant and ultrahigh strength via in situ polymerization. *J Mater Chem* **21**, 13569 (2011).
49. Liao, W.-H. *et al.* Effect of Octa(aminophenyl) Polyhedral Oligomeric Silsesquioxane Functionalized Graphene Oxide on the Mechanical and Dielectric Properties of Polyimide Composites. *ACS Appl Mater Interfaces* **6**, 15802–15812 (2014).
50. Yu, Z., Dai, T., Yuan, S., Zou, H. & Liu, P. Electromagnetic Interference Shielding Performance of Anisotropic Polyimide/Graphene Composite Aerogels. *ACS Appl Mater Interfaces* **12**, 30990–31001 (2020).
51. Jiang, P., Qian, X., Yang, R. & Lindsay, L. Anisotropic thermal transport in bulk hexagonal boron nitride. *Physical Review Materials* vol. 2 Preprint at https://doi.org/10.1103/PhysRevMaterials.2.064005 (2018).
52. Cai, Q. *et al.* High thermal conductivity of high-quality monolayer boron nitride and its thermal expansion. *Sci Adv* **5**, (2019).
53. Li, T.-L. & Hsu, S. L.-C. Enhanced Thermal Conductivity of Polyimide Films via a Hybrid of Micro- and Nano-Sized Boron Nitride. *J Phys Chem B* **114**, 6825–6829 (2010).
54. Sato, K. *et al.* Thermally conductive composite films of hexagonal boron nitride and polyimide with affinity-enhanced interfaces. *J Mater Chem* **20**, 2749 (2010).
55. Wang, J. *et al.* Lightweight, Superelastic Yet Thermoconductive Boron Nitride Nanocomposite Aerogel for Thermal Energy Regulation. *ACS Nano* **13**, 7860–7870 (2019).
56. Zhai, Q. *et al.* Ultralight and Highly Resilient Boron Nitride Nanosheet/Polyimide Foams for Energy Harvesting and Sensing. *ACS Appl Polym Mater* **4**, 3236–3246 (2022).

CHAPTER 3
Synergic effect of graphene oxide and boron nitride on the mechanical properties of polyimide composite films

ABSTRACT

The addition of two-dimensional (2D) materials into polymers can improve their mechanical properties. In particular, graphene oxide (GO) and hexagonal boron nitride (h-BN) have been expected as potential nanoplatelets additives for polymers. Covalent bonds between such nanoplatelets and polymers are effective in improving the above properties. However, no report investigates the effect of using two types of nanoplatelets that have covalent bonds with a polymer. In this study, we fabricated polyimide (PI) films that contain two types of nanoplatelets, amine-functionalized h-BN (BN_{NH2}) and GO, covalently bonded with PI. We have elucidated that there is the critical ratio and the content of BN_{NH2} and GO within PI governing the films' mechanical properties. When the BN_{NH2}/GO weight ratio was 52:1 and their content was 1 wt% in the PI film, the tensile modulus and tensile strength were increased by 155.2 MPa and 4.2 GPa compared with the pristine PI film.

I. INTRODUCTION

Polymer films with molecularly designed structures have been playing an important role in applications such as medical devices,[1] separator in batteries,[2–4] high-performance audio diaphragms,[5] and computer memories.[6] Therefore, the fabrication of polymers with targeted properties is of great interest for the development of next-generation technologies. Polymers have advantages in their ease of processing, lightweight, and chemical resistance compared

with metallic materials.[7,8] Polyimide (PI), which was first synthesized in 1908,9 has extremely high heat and chemical resistances, mechanical properties, and electrical insulation compared to other polymer materials. These properties enable PI to be used in a wide range of applications such as waterproof coatings,[10,11] speaker components,[12–14] separators for batteries,[15,16] gas separations,[17–19] and water purification membranes.[20,21]

The introduction of fillers has been investigated to improve the properties of polymer films. Addition of one- and/or two-dimensional (2D) carbon materials has been aimed at forming strong π–π interaction between the aromatic frameworks in PI and carbon materials.[22,23] For example, physical properties of PI can be improved by the addition of low-dimensional carbon materials, such as carbon nanotube,[24–26] graphene oxide (GO),[27–31] and amine-functionalized carbon materials.[32,33] Another promising filler with a honeycomb structure is hexagonal boron nitride (h-BN), which can interact strongly with 2D carbon materials.[34] Therefore, the mixing of the carbon composites of h-BN would exert a synergic effect, such as thermal conductivity, thermoelectric, and mechanical property.[35–37] Several modification methods of h-BN edges with hydroxyl groups or amino (NH_2) groups were reported recently.[38–40] However, the fabrication of PI-BN/GO composite film and evaluation of its mechanical property has not been reported so far.

In this study, we focused on edge functionalization of h-BN with NH2 groups (BN_{NH2}) to have a good affinity with GO and PI to improve mechanical strength. BN_{NH2} edge can bond with PI through amide bonds, while its basal plane remains non-reactive honeycomb structure. Interestingly, h-BN and GO show good interaction with each other.[41–43] Therefore, we hypothesized that the covering basal plane of BN_{NH2} with GO results in a filler with superior mechanical strength through interaction with PI at both basal plane (oxy functional groups on GO) and edge (amino groups of BN_{NH2}) of 2D structure. In this context, we prepared PI-BN_{NH2}/GO composite, containing both GO and BN_{NH2} to elucidate the effect of employing

multiple types of nanoplatelets in PI films (Fig. 1). As a result, the mechanical properties of PI films were improved by the introduction of BN_{NH2}, and a further improvement was obtained with an additional small amount of GO.

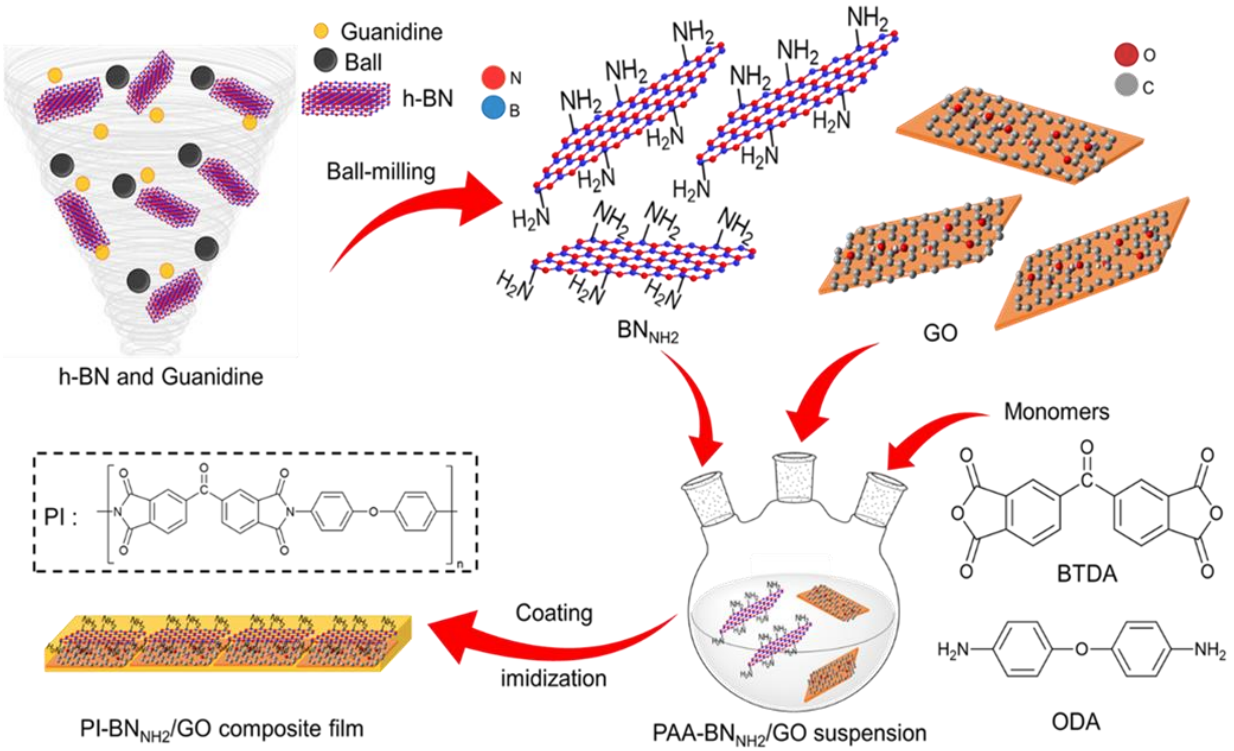

Fig. 1 Schematic illustration of the fabrication of the PI-BN_{NH2}/GO composite film.

II. RESULTS AND DISCUSSION

First, we synthesized amine-functionalized h-BN (BN_{NH2}) by ball milling method (details are shown in the experimental section). We used guanidine or urea as a nitrogen source. Hereafter, we call h-BN treated with urea as BN_{NH2}(U) and treated with guanidine as BN_{NH2}(G), respectively. After ball milling, dialysis was carried out to remove unreacted guanidine or urea. The specimens were treated by sonication for 1h in dimethylacetamide (DMAc), resulting in homogeneous dispersion (Fig. 2).

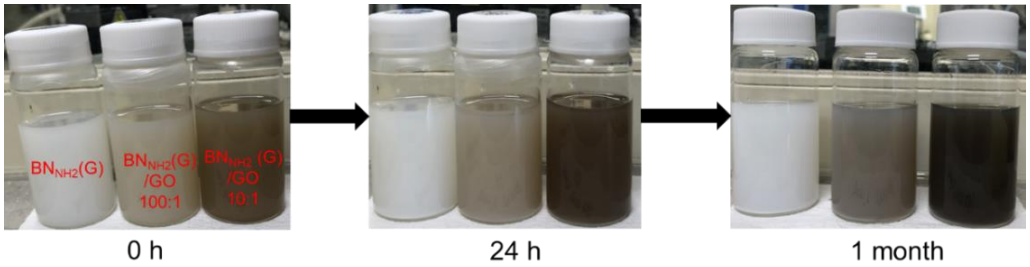

Fig. 2 Schematic illustration of dispersion process (in DMAc).

The Fourier transform infrared (FTIR) analysis exhibited strong peaks at 780 cm^{-1} and 1380 cm^{-1} originating from the in-plane B-N stretching vibration and out-of-plane B-N-B bending vibration (Fig. 3).[44,45] Furthermore, an additional peak appeared at around 3250 cm^{-1} in BN$_{NH2}$(G). This peak is assigned to N-H vibration mode.[46,47]

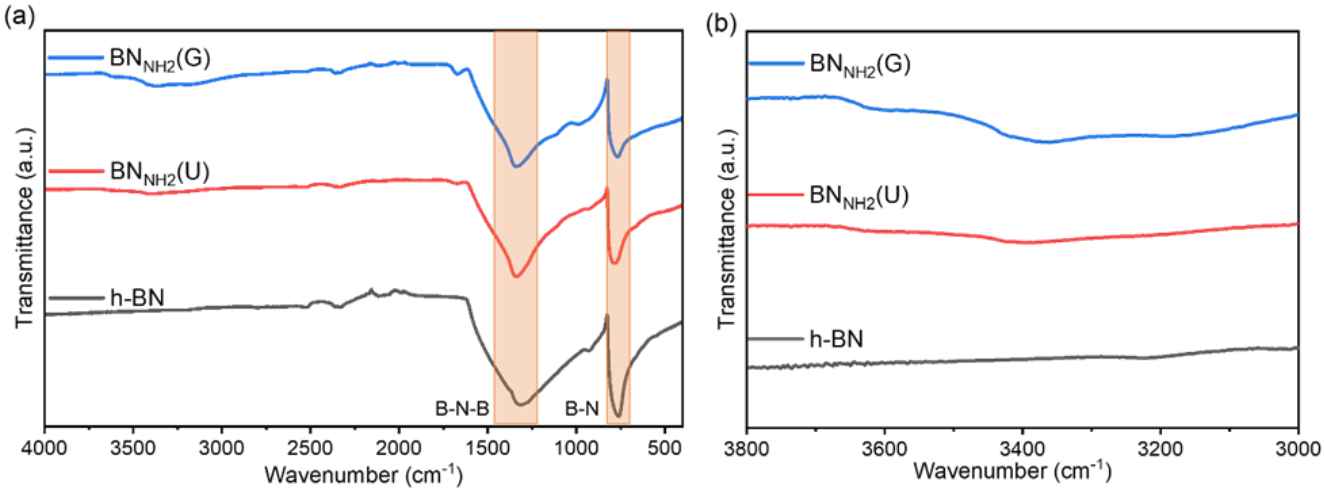

Fig. 3 FT-IR spectra of h-BN, BN$_{NH2}$(U), and BN$_{NH2}$(G): (a) full range and (b) narrow range.

Thermal gravimetric analysis (TGA) results are shown in Fig. 4a. According to the TGA results, BN$_{NH2}$(U) and BN$_{NH2}$(G) showed 2 wt% and 4 wt% loss, respectively, whereas pure h-BN did not show weight loss. These results indicate that functionalized h-BN was successfully synthesized and that more amine-functionalization proceeded by guanidine than by urea. Therefore, BN$_{NH2}$(G) was used for the following experiments. X-ray diffraction (XRD) data are presented in Fig. 4b; BN$_{NH2}$(G) showed two main characteristic diffraction peaks at 26.2° and 42.8° originating from h-BN structure. Compared to the pristine h-BN, the peak intensities of (002) and (100) of BN$_{NH2}$(G) decreased. Thus,

the FWHM of (002) was changed from 0.25 to 0.34, in contrast, the (002) peak position was not significantly shifted (Fig. 4c). These results suggest that h-BN sheets were exfoliated because of the physical force and/or the chemical functionalization during the ball milling process.

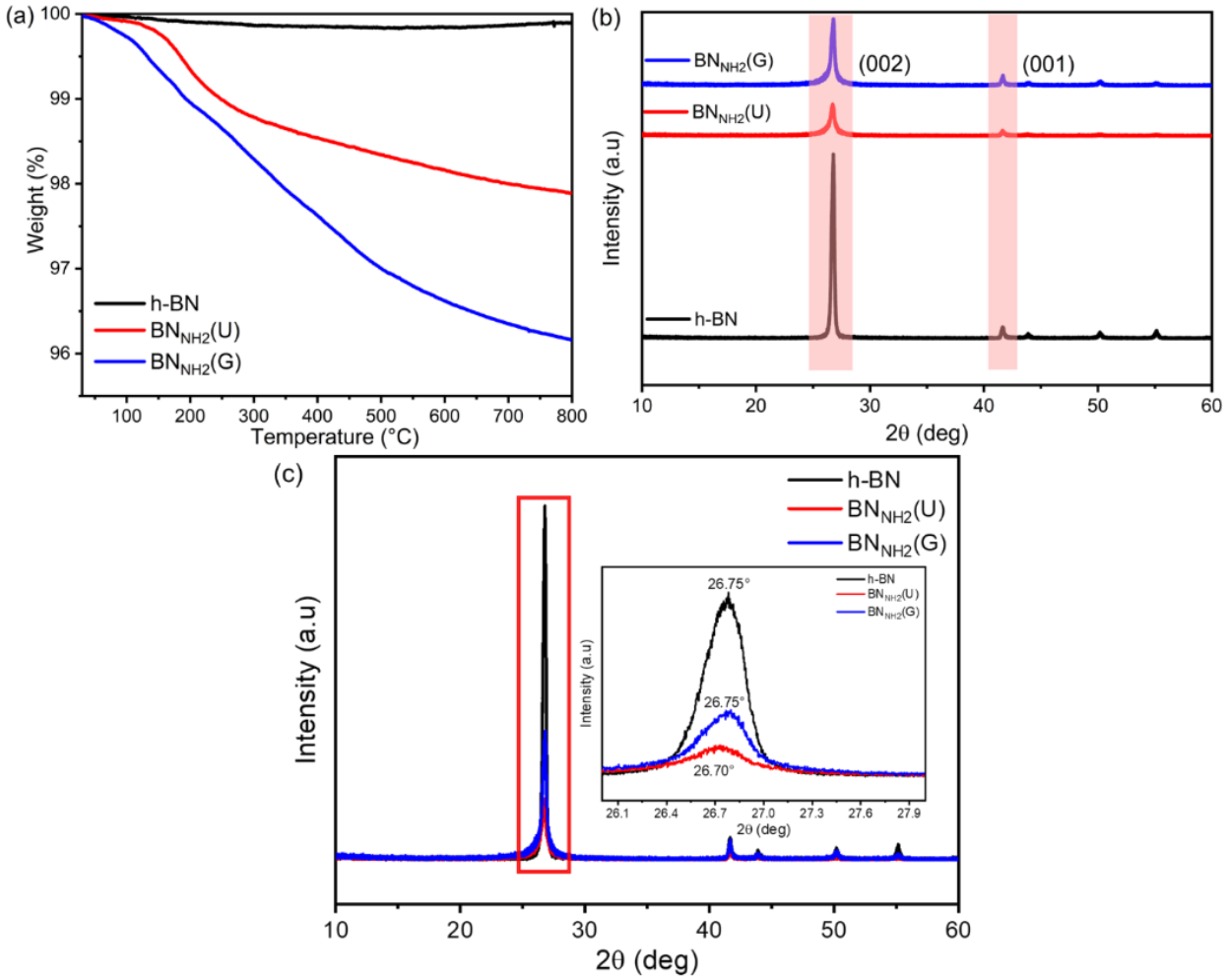

Fig. 4 (a) TGA curves of h-BN, BN_{NH2}(U), and BN_{NH2}(G) with a heating rate of 10 °C min^{-1}. (b) XRD patterns of BN_{NH2}(G), BN_{NH2}(U), and pristine h-BN. (c) XRD patterns of BN_{NH2}(G), BN_{NH2}(U), and pristine h-BN zoom at (002) peak

II.1 Reaction of BN_{NH2} with acid anhydride

To confirm the presence of NH_2 groups in BN_{NH2}, we treated BN_{NH2}(G) with 3,3´,4,4´-benzophenonetetracarboxylic dianhydride (BTDA) to form amide bonds. Detailed synthesis procedure is given in the experimental section. TGA data of h-BN, BN_{NH2}(G), and BN_{NH2}(G) treated with BTDA (BN_{NH2}(G)/BTDA) are presented in Fig. 5. For comparison, h-BN treated with BTDA (h-BN/BTDA) is also listed in Fig. 5a. The h-BN/BTDA sample showed two mass losses of 1.7 wt% and 2.2 wt% at 225 °C and 320 °C. On the other hand, the BN_{NH2}(G)/BTDA sample showed two mass losses of 5.6 wt% and 4.2 wt% at 150 °C and 500 °C, respectively, corresponding to the release of water during the thermal imidization and the carbonization reactions.[48–50] After TGA analysis, only the surface of BN_{NH2}(G)/BTDA turned black (Fig. 5b-e).

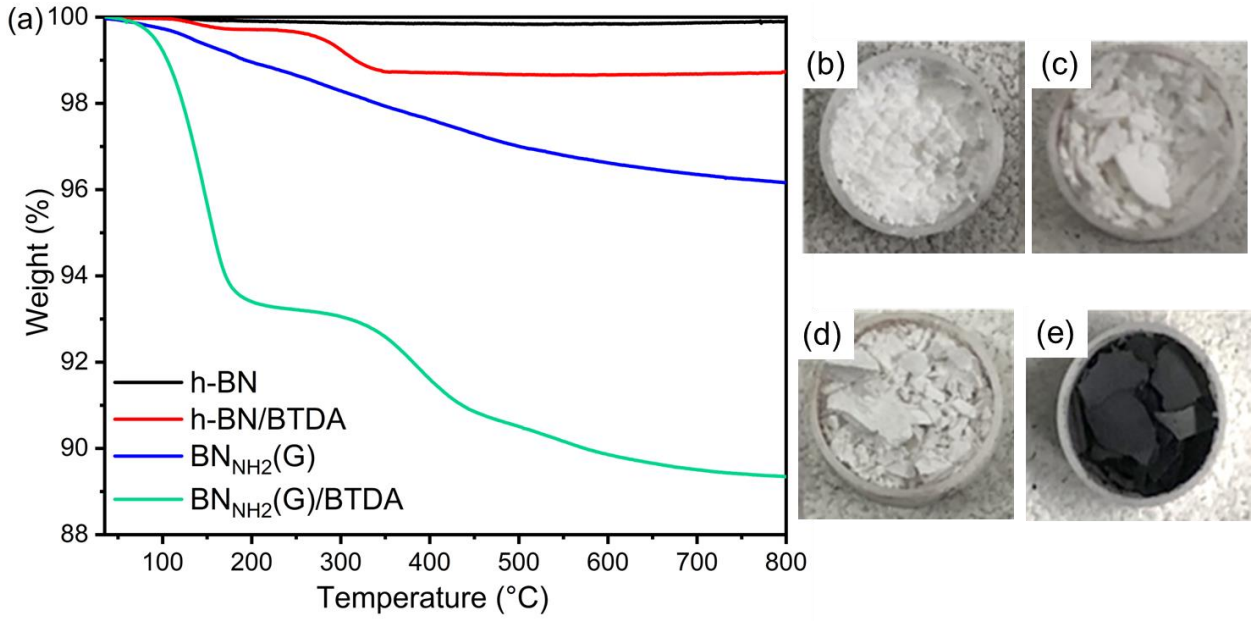

Fig. 5 (a) TGA curves of h-BN, h-BN/BTDA, BN_{NH2}(G), and BN_{NH2}(G)/BTDA with a heating rate of 10 °C min^{-1}. (b) h-BN after TGA. (c) h-BN/BTDA after TGA. (d) BN_{NH2}(G) after TGA. (e) BN_{NH2}(G)/BTDA after TGA.

Furthermore, FTIR spectra of BN_{NH2}(G)/BTDA (Fig. 6a, b) show an additional peak at 1720 cm^{-1} derived from the C=O vibration,[51,52] and the NH stretched vibration at 3520 cm^{-1}[h]as slightly decreased (Fig. 6c). Above description suggests NH_2 group on h-BN can bond with BTDA through amide bond.

In the case of h-BN/BTDA, C=O vibration at 1720 cm^{-1} was not observed (Fig. 6d). The TGA and FTIR results confirm NH_2 groups are present on h-BN, and the NH_2 groups can form amide bonds.

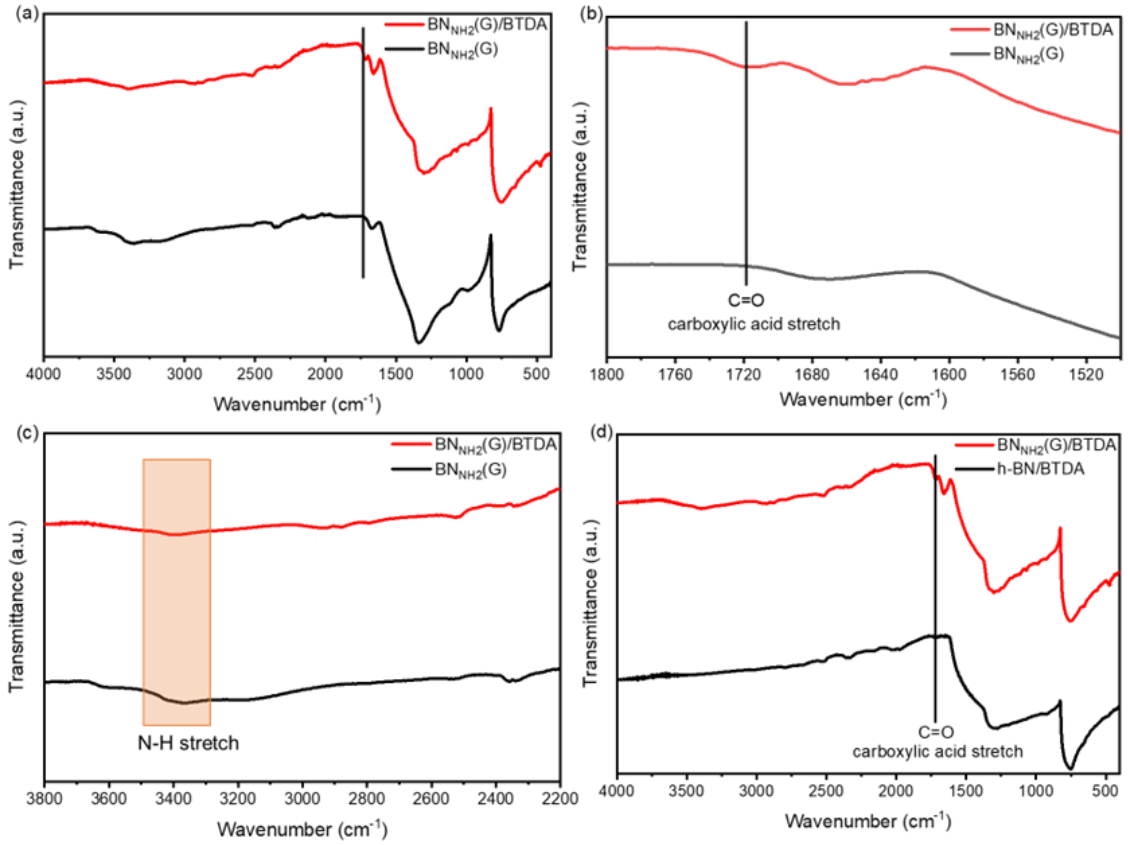

Fig. 6 FT-IR spectra of BN_{NH2}(G)**,** BN_{NH2}(G)/BTDA: (a)~(c). BN_{NH2}(G)/BTDA and h-BN/BTDA comparison: (b). (a) full range, (b) narrow range around C=O peak, (c) narrow range around NH stretch peak, (d) BN_{NH2}(G)/BTDA and h-BN/BTDA full range.

II.2 Fabrication of PI-BN_{NH2}(G) and PI-BN_{NH2}(G)/GO composites films

DMAc is generally used as a solvent for the preparation of polyamic acid (PAA),[32,33] a precursor for PI. Therefore, the dispersibility of BN_{NH2}(G) and BN_{NH2}(G)/GO was investigated in DMAc by sonication. The ratio of BN_{NH2}(G):GO was 10:1 and 100:1, and the obtained samples were termed BN_{NH2}(G)/GO (10:1) and BN_{NH2}(G)/GO (100:1), respectively. The suspensions were stable for more than one month at room temperature without visible precipitation (Fig. 2). The particle size analysis (Fig. 7a-c) showed a mean size of 273 nm, 234 nm, and 223 nm for BN_{NH2}(G), BN_{NH2}(G)/GO (100:1), and BN_{NH2}(G)/GO (10:1), respectively.

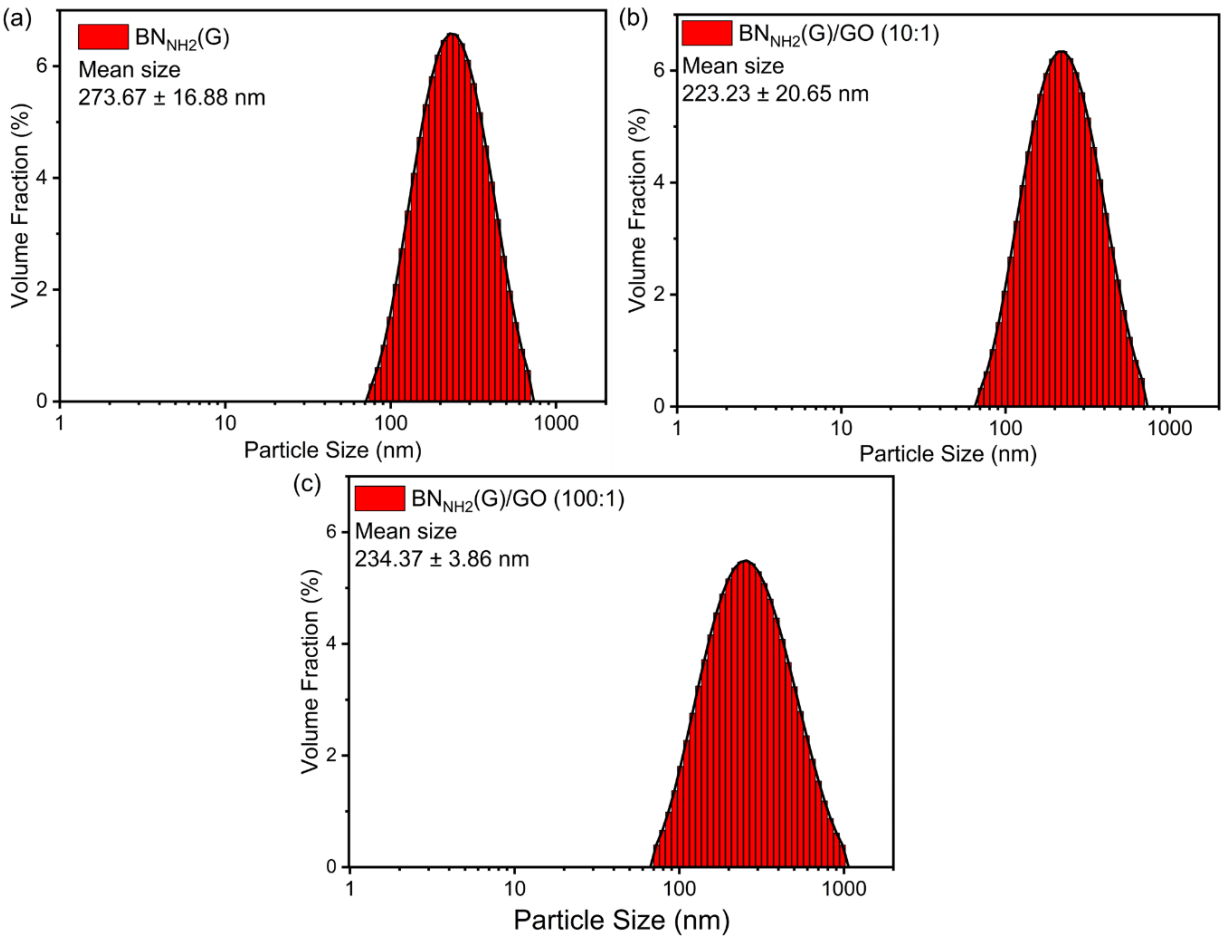

Fig. 7 The particle size analyses of (a) BN_{NH2}(G), (b) BN_{NH2}(G)/GO (10:1), (c) BN_{NH2}(G)/GO (100:1).

Next, homogeneous suspensions of PAA composites were prepared in DMAc by a two-step process. Initially, sonication was employed to disperse BN_{NH2}(G) or BN_{NH2}(G)/GO with 4,4´-diaminodiphenyl ether (ODA) and BTDA. Then, as obtained dispersion was mixed for 12 hours to allow the polymerization and formation of PAA composite suspensions, which are termed as PAA-BN_{NH2}(G), PAA-BN_{NH2}(G)/GO (10:1), and PAA-BN_{NH2}(G)/GO (100:1). These PAA composite suspensions were coated on glass and heated at 300 °C, resulting in PI composite films, termed as PI-BN_{NH2}(G), PI-BN_{NH2}(G)/GO (10:1), and PI-BN_{NH2}(G)/GO (100:1) (detail is shown in the experimental section). A conventional method for the synthesis of PI films consists of the heating of PAA films at elevated temperatures within 200 to 300 °C.[53,54] The heating rate was kept as low as 5 °C min^{-1} to avoid the formation of bubbles within the PI film during the solvent evaporation.[55]

II.3 Mechanical properties of composite films

First, we investigated the effect of BN_{NH2}(G) and GO on PI film. According to Fig. 8 and Table 1, the tensile modulus of PI containing a low quantity (1 wt%) of GO showed 22% increase over the tensile modulus of the pristine PI, although the tensile strength of the PI-GO was slightly decreased (Table 1, Entry 1, and 2). The addition of only GO does not significantly improve the mechanical properties. A previous study also pointed out that GO decreased tensile strength because the interaction between GO and PI is not strong.[31]

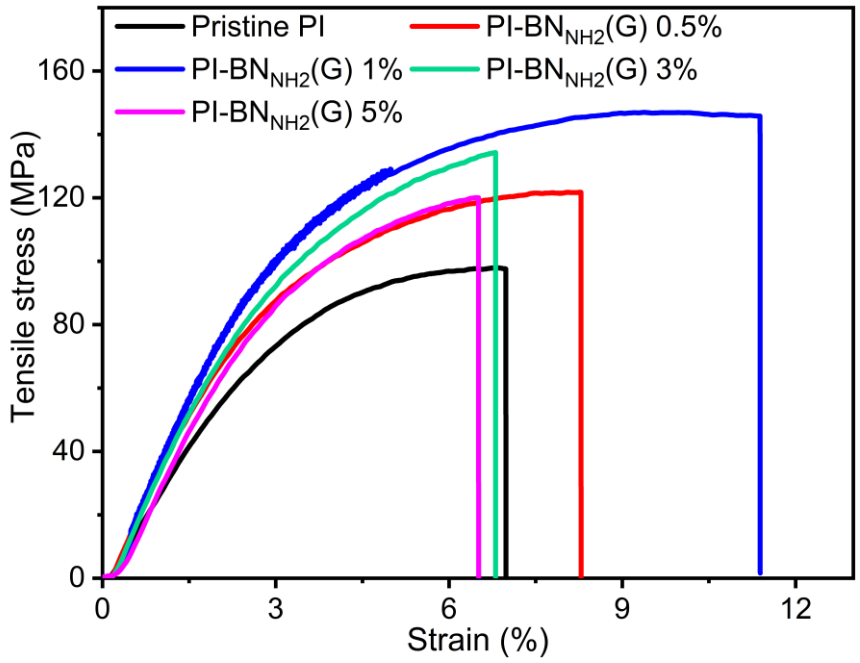

Fig. 8 Stress-strain curves of pristine PI film and PI-BN_{NH2}(G) films.

Next, we investigated the effect of the addition of h-BN, which improved the mechanical properties (Table 1, Entry 3). Due to the surface roughness and wrinkles in h-BN(Fig. 9a, b), the PI-hBN composite film has higher mechanical properties than the pristine PI film, as reported previously.[56] Then, we investigated the composite with BN_{NH2}(G) to elucidate the effect of the functionalization. The tensile strength of PI containing a low quantity (0.5 wt%) of BN_{NH2}(G) showed 23% increase over the tensile strength of the pristine PI (Table 1, Entry 4). Increasing the amount of BN_{NH2}(G) from 0.5 to 1 wt% improved the tensile strength by 44% (Table 1, Entry 5). However, further increase of

BN_{NH2}(G) to 3 wt% decreased both the tensile strength and tensile modulus (Table 1, Entry 6). These results indicate that an excess amount of BN_{NH2}(G) leads to reducing the positive effects of BN_{NH2}(G) in the PI matrix, probably caused by the stacking of BN_{NH2}(G) and void formation. Therefore, the optimal amount of BN_{NH2}(G) in PI is determined to be 1 wt%.

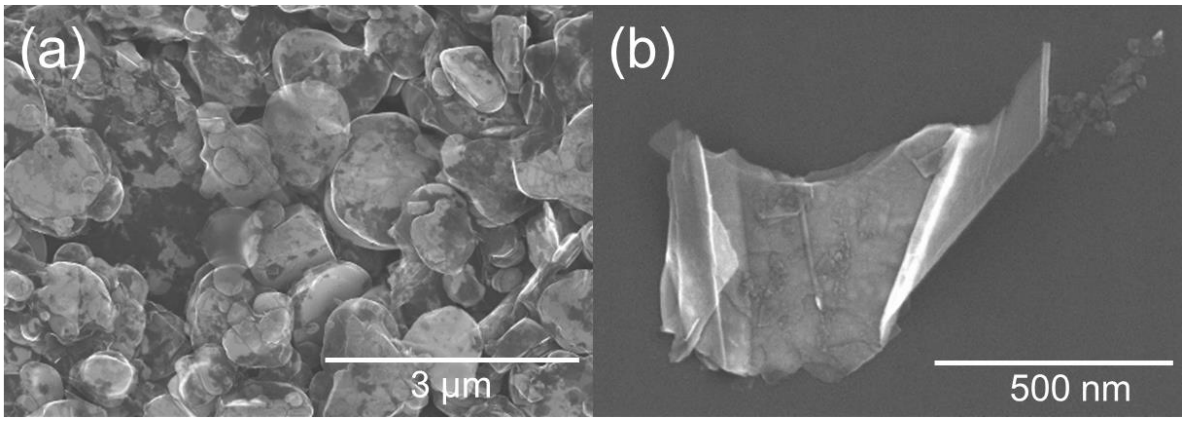

Fig. 9 SEM images of fractured surface of (a)h-BN powder (b) Dispersion of h-BN via ultrasound in DMAc

Than those including a single component (GO, h-BN, or BNNH2(G)) (Table 1, Entry 2, 3, 4, 5, and 6). This suggests there is a good interaction between GO and BN, which enhances the mechanical properties of PI. According to the table1 (Entry 7 and 8) and Fig. 10, the tensile strength and tensile modulus of BNNH2(G)/GO composite film are 22% and 23% higher than PI-hBN/GO. This proved the edge-functionalization of h-BN improves mechanical properties of composite film. In addition, PI-BNNH2(G)/GO composite film has a tensile strength of approximately 154.89 MPa, which is 65% higher than the original PI, and the tensile modulus was increased to 3.83 GPa, which is 69% higher than the original PI (Table 1, Entry 1). By reducing the amount of BNNH2(G)/GO to 0.5 wt% of BNNH2(G), the tensile strength and tensile modulus of PI were also reduced to 118.96 MPa and 2.84 GPa (Table 1, Entry 9). When the BNNH2(G)/GO ratio increases to 10:1, the tensile strength dropped to 137.33 MPa and the tensile modulus also dropped to 3.30 GPa (Table 1, Entry 10). Similar to only h-BN, there is a critical BNNH2(G)/GO amount for the improvement of PI film mechanical properties. Furthermore, these data also revealed that the ratio of BNNH2(G) and GO strongly affects PI film mechanical properties.

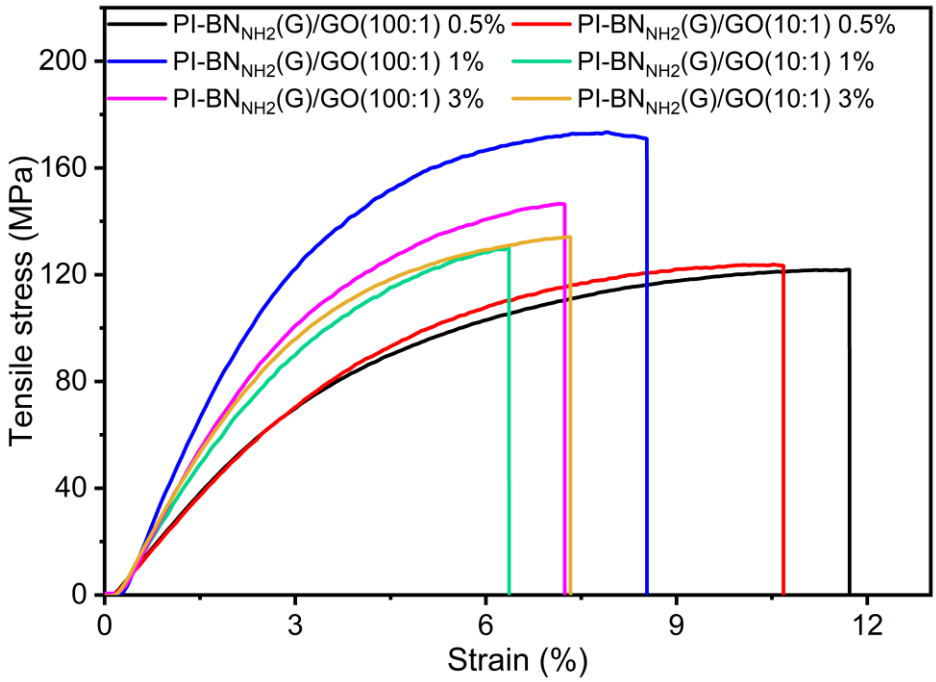

Fig. 10 Stress-strain curves of PI- BN_{NH2}(G) (100:1) and PI-BN_{NH2}(G) (10:1) films.

Based on our experimental results, we propose a model structure of PI-BN_{NH2}(G)/GO. As reported previously, GO sheets are easily aggregated in the composite, resulting in lower tensile strength (Fig. 11a, b).[31] In contrast, GO has a strong affinity with h-BN (Fig. 11c, d).[41-43] The attachment of GO on BN_{NH2}(G) surface facilitates the interaction with PI because of the following synergic effect; 1) amide bond formation with BTDA at the edge of BN_{NH2}(G),[57] and 2) amination of GO at the basal plane with ODA through epoxy ring-opening reaction.[27] Due to these effects, BN_{NH2}(G)/GO composite would successfully enhance the mechanical properties of PI.

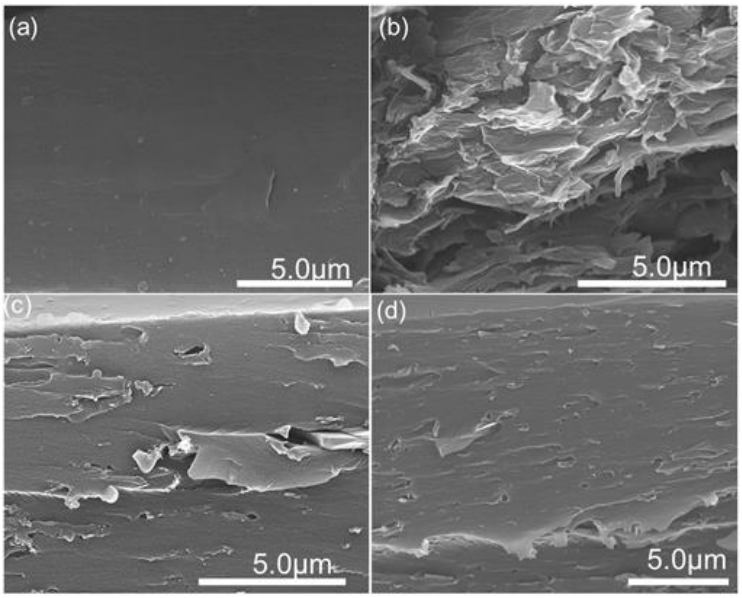

Fig. 11 SEM images of fractured surface of (a) pristine PI, (b) PI-GO 1wt%, (c) PI- BN_{NH2}(G) 1wt%, (d) PI- BN_{NH2}(G)/GO (100:1) 1wt% films.

Ideally, BN_{NH2}(G)/GO should be composed of single BN_{NH2}(G) flakes covered by single-layer GO on both sides. According to AFM measurement, the average thickness of BN_{NH2}(G) was 36 nm (Fig. 12).

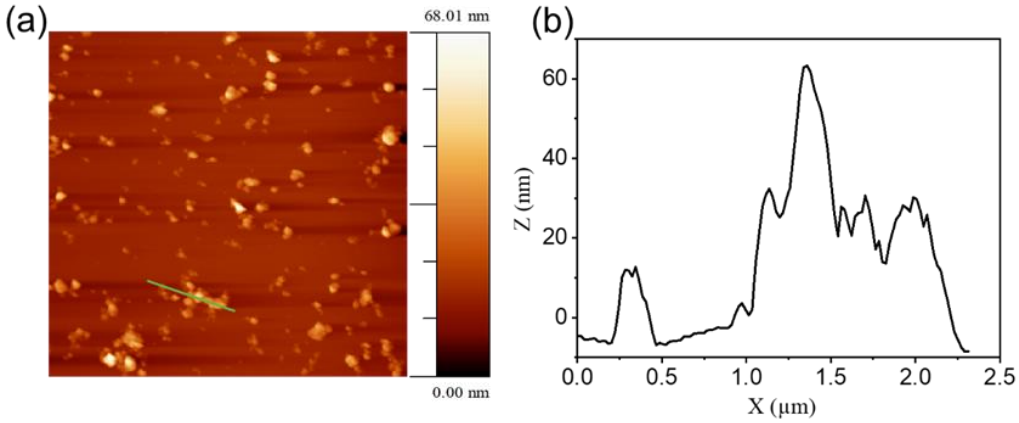

Fig. 12 (a) AFM images of BN_{NH2}(G) flakes, (b) the height profile along the green line in (a).

Considering the thickness of a single layer h-BN is 0.33 nm,[58] the prepared BN_{NH2}(G) is composed of about 109 layers. As GO sheets are adsorbed only on the surface of BN_{NH2}(G), the ideal ratio to fully cover BN_{NH2}(G) surface with GO is 109 layers of BN_{NH2}(G) and 2 layers of GO. Considering the unit weight of BN and GO (the elemental ratio of C and O is 2: 1), the ideal ratio of BN_{NH2}(G)/GO is

52:1. To prove our speculation, we measured the mechanical properties of BN_{NH2}(G)/GO that has a ratio of 52:1 (BN_{NH2}(G)/GO(52:1)); its tensile modulus increased by 86%, and the tensile strength increased 65% in comparison to the neat PI film (Table 1, Entry 12). This specimen shows the highest tensile strength and tensile modulus among all specimens, which supports our hypothesis that surface coating of h-BN with GO is desirable for the strong interaction with PI.

Table 1. Mechanical properties of neat PI film, PI-BN_{NH2}(G) films, and PI-BN_{NH2}(G)/GO films.

Entry	Sample	Percentage of sample in PI	Tensile strength (MPa)	Tensile modulus (GPa)	Elongation at break (%)
1	Pristine PI	-	93.9 ± 3.4	2.2 ± 0.2	10.6 ± 3.6
2	PI-GO	1	90.2 ± 6.3	2.7 ± 0.1	4.4 ± 1.3
3	PI-hBN	1	110.9 ± 7.0	2.7 ± 0.1	6.8 ± 1.4
4	PI-BN_{NH2}(G)	0.5	114.9 ± 5.9	3.1 ± 0.1	7.8 ± 3.1
5	PI-BN_{NH2}(G)	1	135.7 ± 5.4	3.1 ± 0.5	10.3 ± 1.7
6	PI-BN_{NH2}(G)	3	126.8 ± 6.3	3.3 ± 0.1	6.4 ± 0.8
7	PI-hBN/GO (100:1)	1	127.4 ± 6.8	3.1 ± 0.2	9.5 ± 3.1
8	PI-BN_{NH2}(G)/GO (100:1)	1	154.8 ± 11.1	3.8 ± 0.4	7.8 ± 1.6
9	PI-BN_{NH2}(G)/GO (100:1)	0.5	118.9 ± 4.1	2.1 ± 0.2	13.9 ± 3.2
10	PI-BN_{NH2}(G)/GO (10:1)	1	137.3 ± 3.2	3.3 ± 0.1	7.2 ± 1.5
11	PI-BN_{NH2}(G)/GO (10:1)	3	129.8 ± 4.2	2.9 ± 0.4	7.9 ± 0.9
12	PI-BN_{NH2}(G)/GO (52:1)	1	155.2 ± 2.1	4.2 ± 0.1	7.1 ± 0.7

[a] 1 wt% sample for PI matrix was used in this table.

III. CONCLUSIONS

Improvement of the mechanical properties of composite films, including modulus, strength, and failure strain, has attracted tremendous interest in the field of materials science. Although the improvement of the modulus and/or strength has been realized in current studies,[59,60] the improvement of failure strain along with modulus and strength is rare in the previous studies. In this research, we

have demonstrated the improvement of the mechanical properties of PI films using the mixture of two types of materials, BN_{NH2}(G) and GO. Changing the ratio between BN and GO and their ratio with PI, we elucidated that there is a critical value at which PI composite film showed the highest tensile modulus, tensile strength, and failure strain in the same time. This enhances the toughness and potential application of PI.

In the case of 1 wt% PI-BN_{NH2}(G)/GO (52:1) composite film, the tensile modulus increased by 86%, and the tensile strength increased by 65% in comparison to the neat PI film. According to our results, we proposed and experimentally confirmed a model for the improvement of PI mechanical properties via the addition of BN_{NH2}(G) and GO. In the case of BN_{NH2}(G), only NH_2 groups at edges interact with the raw materials of PI because of BN_{NH2}(G) surface is inert. On the other hand, covering the BN_{NH2}(G) surface with GO creates additional interaction between the BN_{NH2}(G)/GO surface and the raw material of PI. Therefore, PI can be grafted both on surfaces and edges, which enhances the mechanical properties of PI composite film. In contrast, the excess amount of GO that is not attached to the h-BN surface deteriorates the mechanical properties of the composite. Our results and the proposed mechanism will be useful guidelines for fabricating 2D composite materials in polymer matrixes.

IV. EXPERIMENTAL SECTION

IV.1 Materials

Hexagonal boron nitride (h-BN) average size (1~2 μm) was purchased from Showa Denko K.K., Japan. Guanidine hydrochloride (purity 99.0+%), 3,3´,4,4´-benzophenonetetracarboxylic dianhydride (BTDA, purity 96.0+%), 4,4´-diaminodiphenyl ether (ODA, purity 99.0+%), dimethylacetamide (DMAc, purity 98.0+%), sulfuric acid (H_2SO_4, purity 95.0+%), and potassium permanganate ($KMnO_4$, purity 99.3+%) were purchased from FUJIFILM Wako Pure Chemical Corporation, Japan.

IV.2 Characterization instruments

The particle size analyzer (PSA) used in this work was ELSZ-2000N (Photal Otsuka Electronics, Japan). The samples for the PSA were dispersed in DMAc. Fourier transform infrared spectroscopy (FTIR) spectra of samples were recorded between 400 and 4000 cm^{-1} with IRTracer-100 (Shimadzu Corporation, Japan). The scanning electron microscope (SEM) measurement was performed with S-5200 (Hitachi Limited, Japan) with an accelerating voltage of 30 kV. X-ray diffraction (XRD) measurements were performed on AERIS equipped with single crystalline silicon (Panalytical, Netherlands). Thermal gravimetric analyses (TGA) were performed with a DTG-60AH (Shimadzu Corporation, Japan) from room temperature to 800 °C in nitrogen (N_2) at a heating rate of 10 °C min^{-1}. To measure the tensile strength of PI films, sample sheets were cut into 10 mm × 60 mm and were tested using a Universal Testing Machine AG-Xplus (Shimadzu, Japan) at a tensile testing rate of 1 mm/min.

IV.3 Preparation of graphene oxide (GO)

GO was prepared using a modified Hummers' method.[61,62] Graphite (3.0 g) was stirred in 95% H_2SO_4 (75 mL). $KMnO_4$ (9.0 g) was gradually added to the solution while keeping the temperature under 10 °C, using an ice bath. The mixture was then stirred at 35 °C for 2 h. The resulting mixture was diluted by water (75 mL) under vigorous stirring and cooling so that temperature does not exceed 50 °C. The suspension was further treated by 30% aq. H_2O_2 (7.5 mL). The resulting graphite oxide suspension was purified by centrifugation with water until neutralization, and freeze-dried.

IV.4 Preparation of amine-functionalized hexagonal boron nitride (BN_{NH2}(G))

BN_{NH2}(G) was prepared using a ball mill Pulverisette 7 Classic Line (Fritsch, Germany).[39,40] h-BN (0.5 g) and guanidine hydrochloride (10 g) were mixed by a ball mill at a rotation speed of 750rpm for 16 h at ambient temperature. Water (ca. 50 mL) was added to the solid product. The resulting BN_{NH2}(G) suspension was purified by dialysis (membrane cutoff: 12000~14000 kDa) in deionized (DI) water for 24 h (DI water was changed every 3 h, which was repeated 3 times, then settled for 16 h) to remove

the guanidine hydrochloride. A 1 week dialyzed treatment was also investigated (Fig. 13), but no difference was detected with thein 24 h treated sample. Therefore, the 24 h dialyzed treatment was selected. Finally, the sample was ultrasound for 10 min in DI water, and freeze-dried.

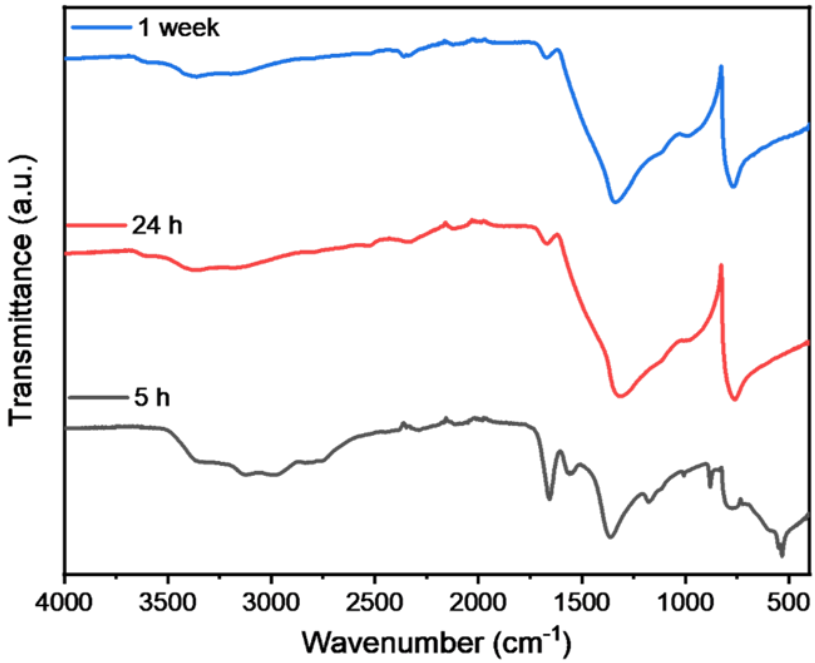

Fig. 13 FT-IR spectra of BN_{NH2}(G) by three different dialysis times (5h, 24h, and 1 week).

IV.5 Preparation of PI-BN_{NH2}(G) composite films

To prepare different concentrations PAA-BN_{NH2}(G) suspension, BN_{NH2}(G) (0.026 g, 0.053 g, 0.161 g, or 0.274 g) was dispersed in DMAc (20ml) by sonication for 1h. ODA (2.0 g, 10 mmol) was added in the BN_{NH2}(G) suspension by sonication for 10 min. Then, BTDA (3.2 g, 10 mmol) was added into the suspension, sonicated for 10 min, and cooled into freezer at about -18 °C for 12 h.

A viscous PAA-BN_{NH2}(G) suspension was coated on glass using MSK-AFA-III coater (MTI Corporation, USA) with a coating rate of 20 mm/sec. The coating was heated at 90 °C for 1h (heating speed 1 °C/min under nitrogen) to evaporate solvent. Finally, PI I was formed by heat-treatment from room temperature to 300 °C for 1h (room temperature to 300 °C for 5 h under nitrogen).

IV.6 Preparation of PI-BN_{NH2}(G)/GO composite films

BN_{NH2}(G)/GO (100:1) or BN_{NH2}(G)/GO (10:1) (5.2 g) were dispersed in DMAc (20 ml) with sonication for 1h. ODA (2.0 g, 10 mmol) was added in the BN_{NH2}(G)/GO suspension with sonication for 10 min. BTDA (3.2g, 10 mmol) was then added into the suspension and sonicated for 10 min, furnishing PAA-BN_{NH2}(G)/GO suspension. The mixture was coated on glass and heated at 90 °C for 1h (heating speed: 1 °C min^{-1} under nitrogen) to evaporate the solvent. Next, heat-treatment was performed from room temperature to 300 °C in 5 h under nitrogen atmosphere, then kept at 300 °C for 1h. The PI-BN_{NH2}(G)/GO composite films containing 0.5wt%, 1wt%, and 3wt% of BN_{NH2}(G)/GO were prepared by the same procedures.

REFERENCES

1. Alf, M. E. *et al.* Chemical vapor deposition of conformal, functional, and responsive polymer films. *Advanced Materials* **22**, 1993–2027 (2010).
2. Wang, C., Zheng, W., Yue, Z., Too, C. O. & Wallace, G. G. Buckled, stretchable polypyrrole electrodes for battery applications. *Advanced Materials* **23**, 3580–3584 (2011).
3. Chen, Z. *et al.* Fast and reversible thermoresponsive polymer switching materials for safer batteries. *Nat Energy* **1**, (2016).
4. Kim, J. K. *et al.* Nano-fibrous polymer films for organic rechargeable batteries. *J Mater Chem A Mater* **1**, 2426–2430 (2013).
5. Kang, S. *et al.* Transparent and conductive nanomembranes with orthogonal silver nanowire arrays for skin-attachable loudspeakers and microphones. *Sci Adv* **4**, 1–12 (2018).
6. Park, Y. J., Bae, I. S., Ju Kang, S., Chang, J. & Park, C. Control of thin ferroelectric polymer films for non-volatile memory applications. *IEEE Transactions on Dielectrics and Electrical Insulation* **17**, 1135–1163 (2010).
7. Bernards, D. A. & Desai, T. A. Nanoscale porosity in polymer films: Fabrication and therapeutic applications. *Soft Matter* **6**, 1621–1631 (2010).
8. Ogieglo, W., Wormeester, H., Eichhorn, K. J., Wessling, M. & Benes, N. E. In situ ellipsometry studies on swelling of thin polymer films: A review. *Prog Polym Sci* **42**, 42–78 (2015).
9. Bogert, M. T. & Renshaw, R. R. 4-Amino-O-Phthalic Acid and Some of Its Derivatives. *J Am Chem Soc* **30**, 1135–1144 (1908).
10. Ma, Y. *et al.* Tunable dielectric and other properties in high-performance sandwich-type polyimide films achieved by adjusting the porous structure. *J Mater Chem C Mater* **7**, 7360–7370 (2019).
11. Komamura, T., Okuhara, K., Horiuchi, S., Nabae, Y. & Hayakawa, T. Fabrication of Well-Ordered Mesoporous Polyimide Films by a Soft-Template Method. *ACS Appl Polym Mater* **1**, 1209–1219 (2019).
12. Hosoya, N., Baba, S. & Maeda, S. Hemispherical breathing mode speaker using a dielectric elastomer actuator. *J Acoust Soc Am* **138**, EL424–EL428 (2015).
13. Kim, K. M. & Park, K. Numerical investigation on vibration characteristics of a micro-speaker diaphragm considering thermoforming effects. *Journal of Mechanical Science and Technology* **27**, 2923–2928 (2013).
14. Sharifzadeh Mirshekarloo, M. *et al.* Transparent piezoelectric film speakers for windows with active noise mitigation function. *Applied Acoustics* **137**, 90–97 (2018).
15. Wang, H. G. *et al.* Tailored aromatic carbonyl derivative polyimides for high-power and long-cycle sodium-organic batteries. *Adv Energy Mater* **4**, 1–7 (2014).

16. Miao, Y. E., Zhu, G. N., Hou, H., Xia, Y. Y. & Liu, T. Electrospun polyimide nanofiber-based nonwoven separators for lithium-ion batteries. *J Power Sources* **226**, 82–86 (2013).
17. Kim, T. H., Koros, W. J., Husk, G. R. & O'Brien, K. C. Relationship between gas separation properties and chemical structure in a series of aromatic polyimides. *J Memb Sci* **37**, 45–62 (1988).
18. Coleman, M. R. & Koros, W. J. Isomeric polyimides based on fluorinated dianhydrides and diamines for gas separation applications. *J Memb Sci* **50**, 285–297 (1990).
19. Wang, Y. *et al.* Functionalized Boron Nitride Nanosheets: A Thermally Rearranged Polymer Nanocomposite Membrane for Hydrogen Separation. *Angewandte Chemie* **130**, 16288–16293 (2018).
20. Chen, G. Q., Scholes, C. A., Qiao, G. G. & Kentish, S. E. Water vapor permeation in polyimide membranes. *J Memb Sci* **379**, 479–487 (2011).
21. Minelli, M. *et al.* Vapor and liquid sorption in matrimid polyimide: Experimental characterization and modeling. *Ind Eng Chem Res* **52**, 8936–8945 (2013).
22. Okamoto, M., Fujigaya, T. & Nakashima, N. Individual dissolution of single-walled carbon nanotubes by using polybenzimidazole, and highly effective reinforcement of their composite films. *Adv Funct Mater* **18**, 1776–1782 (2008).
23. Qin, S. *et al.* Facile preparation of polyimide/graphene nanocomposites via an in situ polymerization approach. *RSC Adv* **7**, 3003–3011 (2017).
24. Lebrón-Colón, M. *et al.* Reinforced thermoplastic polyimide with dispersed functionalized single wall carbon Nanotubes. *ACS Appl Mater Interfaces* **2**, 669–676 (2010).
25. Cui, C. *et al.* High strength composites using interlocking carbon nanotubes in a polyimide matrix. *Carbon N Y* **60**, 102–108 (2013).
26. Ning, W. *et al.* Multifunctional super-aligned carbon nanotube/polyimide composite film heaters and actuators. *Carbon N Y* **139**, 1136–1143 (2018).
27. Chen, D., Zhu, H. & Liu, T. In situ thermal preparation of polyimide nanocomposite films containing functionalized graphene sheets. *ACS Appl Mater Interfaces* **2**, 3702–3708 (2010).
28. Luong, N. D. *et al.* Enhanced mechanical and electrical properties of polyimide film by graphene sheets via in situ polymerization. *Polymer (Guildf)* **52**, 5237–5242 (2011).
29. Kong, J. Y. *et al.* Preparation and properties of polyimide/graphene oxide nanocomposite films with Mg ion crosslinker. *Eur Polym J* **48**, 1394–1405 (2012).
30. Kim, K. *et al.* Effect of defect-healing in graphene nanosheets on the mechanical properties of polyimide nanocomposites. *Carbon N Y* **122**, 614–621 (2017).
31. Chen, Z., Tong, F., Zhu, D., Lu, X. & Lu, Q. Ductile Polyimide/Reduced Graphene Oxide Nanohybrid Films with Porous Structure Fabricated by a Green Hydrogel Strategy. *ACS Appl Polym Mater* **1**, 914–923 (2019).
32. Liao, W. H. *et al.* Effect of molecular chain length on the mechanical and thermal properties of amine-functionalized graphene oxide/polyimide composite films prepared by in situ polymerization. *ACS Appl Mater Interfaces* **5**, 869–877 (2013).

33. Wang, J. Y. *et al.* Preparation and properties of graphene oxide/polyimide composite films with low dielectric constant and ultrahigh strength via in situ polymerization. *J Mater Chem* **21**, 13569–13575 (2011).
34. Chu, T. *et al.* Cationic Hexagonal Boron Nitride, Graphene, and MoS 2 Nanosheets Heteroassembled with Their Anionic Counterparts for Photocatalysis and Sodium-Ion Battery Applications. *ACS Appl Nano Mater* **3**, 5327–5334 (2020).
35. Li, H., Tay, R. Y., Tsang, S. H., Liu, W. & Teo, E. H. T. Reduced graphene oxide/boron nitride composite film as a novel binder-free anode for lithium ion batteries with enhanced performances. *Electrochim Acta* **166**, 197–205 (2015).
36. Li, H. *et al.* Multifunctional and highly compressive cross-linker-free sponge based on reduced graphene oxide and boron nitride nanosheets. *Chemical Engineering Journal* **328**, 825–833 (2017).
37. Yang, G. *et al.* Boron nitride microsheets bridged with reduced graphene oxide as scaffolds for multifunctional shape stabilized phase change materials. *Solar Energy Materials and Solar Cells* **209**, 110441 (2020).
38. Wang, J. *et al.* Lightweight, Superelastic Yet Thermoconductive Boron Nitride Nanocomposite Aerogel for Thermal Energy Regulation. *ACS Nano* **13**, 7860–7870 (2019).
39. Lei, W. *et al.* Boron nitride colloidal solutions, ultralight aerogels and freestanding membranes through one-step exfoliation and functionalization. *Nat Commun* **6**, 1–8 (2015).
40. Chen, C. *et al.* Functionalized boron nitride membranes with ultrafast solvent transport performance for molecular separation. *Nat Commun* **9**, (2018).
41huang, T. *et al.* Boron nitride@graphene oxide hybrids for epoxy composites with enhanced thermal conductivity. *RSC Adv* **6**, 35847–35854 (2016).
42. Byun, S. *et al.* Ordered, Scalable Heterostructure Comprising Boron Nitride and Graphene for High-Performance Flexible Supercapacitors. *Chemistry of Materials* **28**, 7750–7756 (2016).
43 he, X. & Wang, Y. Highly Thermally Conductive Polyimide Composite Films with Excellent Thermal and Electrical Insulating Properties. *Ind Eng Chem Res* **59**, 1925–1933 (2020).
44. Lin, Y. *et al.* Aqueous dispersions of few-layered and monolayered hexagonal boron nitride nanosheets from sonication-assisted hydrolysis: Critical role of water. *Journal of Physical Chemistry C* **115**, 2679–2685 (2011).
45. Weng, Q. *et al.* Highly water-soluble, porous, and biocompatible boron nitrides for anticancer drug delivery. *ACS Nano* **8**, 6123–6130 (2014).
46. Geick, R., Perry, C. H. & Rupprecht, G. Normal modes in hexagonal boron nitride. *Physical Review* **146**, 543–547 (1966).
47. Shi, Y. *et al.* Synthesis of few-layer hexagonal boron nitride thin film by chemical vapor deposition. *Nano Lett* **10**, 4134–4139 (2010).

48. Chang, J. H. & Park, K. M. Thermal cyclization of the poly(amic acid): thermal, mechanical, and morphological properties. *European Polymer Journal* vol. 36 2185–2191 Preprint at https://doi.org/10.1016/S0014-3057(99)00280-3 (2000).
49. Liaw, D. J. *et al.* Advanced polyimide materials: Syntheses, physical properties and applications. *Progress in Polymer Science* vol. 37 907–974 Preprint at https://doi.org/10.1016/j.progpolymsci.2012.02.005 (2012).
50. Mochizuki, A., Teranishi, T. & Ueda, M. Preparation and properties of polyisoimide as a polyimide-precursor. *Polym J* **26**, 315–323 (1994).
51. Shin, S., Jang, J., Yoon, S. H. & Mochida, I. A study on the effect of heat treatment on functional groups of pitch based activated carbon fiber using FTIR. *Carbon N Y* **35**, 1739–1743 (1997).
52. Gershevitz, O. & Sukenik, C. N. In Situ FTIR-ATR Analysis and Titration of Carboxylic Acid-Terminated SAMs. *J Am Chem Soc* **126**, 482–483 (2004).
53. Liao, W. H. *et al.* Effect of molecular chain length on the mechanical and thermal properties of amine-functionalized graphene oxide/polyimide composite films prepared by in situ polymerization. *ACS Appl Mater Interfaces* **5**, 869–877 (2013).
54. Henglein, A. Small-Particle Research: Physicochemical Properties of Extremely Small Colloidal Metal and Semiconductor Particles. *Chem Rev* **89**, 1861–1873 (1989).
55. Brekner, M. -J & Feger, C. Curing studies of a polyimide precursor. II. Polyamic acid. *J Polym Sci A Polym Chem* **25**, 2479–2491 (1987).
56. Lavin, J. M., Keicher, D. M., Whetten, S. R., Moore, P. B. & Mani, S. S. Understanding Sources Of Defects In Polyimide Films Using Aerosol Based Printing. *Solid Freeform Fabrication 2016* 729–737 (2016).
57. Zhi, C., Bando, Y., Tang, C., Kuwahara, H. & Golberg, D. Large-scale fabrication of boron nitride nanosheets and their utilization in polymeric composites with improved thermal and mechanical properties. *Advanced Materials* **21**, 2889–2893 (2009).
58. Zheng, X. *et al.* Preparation of polyimide/amino-modified reduced graphene oxide composite matrix and its application in UV-cured functionalized films. *Prog Org Coat* **124**, 122–128 (2018).
59. Topsakal, M., Aktürk, E. & Ciraci, S. First-principles study of two- and one-dimensional honeycomb structures of boron nitride. *Phys Rev B* **79**, 115442 (2009).
60. Chen, L. *et al.* Enhanced epoxy/silica composites mechanical properties by introducing graphene oxide to the interface. *ACS Appl Mater Interfaces* **4**, 4398–4404 (2012).
61. Rodrigues, C. *et al.* Mechanical, Thermal and Antimicrobial Properties of Chitosan-Based-Nanocomposite with Potential Applications for Food Packaging. *J Polym Environ* **28**, 1216–1236 (2020).
62. Hummers, W. S. & Offeman, R. E. Preparation of Graphitic Oxide. *J Am Chem Soc* **80**, 1339 (1958).
63. Morimoto, N. *et al.* Real-Time, in Situ Monitoring of the Oxidation of Graphite: Lessons Learned. *Chemistry of Materials* **29**, 2150–2156 (2017).

CHAPTER 4
Ball mill enhances the functionalization of boron nitride: the application for polyimide fillers

ABSTRACT

Polymer properties can be tuned by the addition of filler materials such as carbon-base materials and inorganic materials. In recent years, 2D filers as additives for polymers have extensively been studied. Among them, functionalized hexagonal boron nitride (FBN) improves polymers' physical properties. In this study, we prepared 27 types of FBNs by using different ball milling parameters in the presence of amine molecules. Ball mill conditions, such as the ratios of h-BN and the amine, rotation speeds, and treatment times of ball milling, were investigated, and then, the FBNs were covalently bonded with polyimide (PI) in all specimens. An optimum FBN-PI composite showed tensile strength and tensile modulus of 151.1 MPa and 3.8 GPa, respectively. Finally, we found that the tensile strength and modulus were increased to 159.2 MPa and 3.9 GPa by addition of a small amount of graphene oxide (GO) that were combined with FBN and PI. The ball milling and covalent bonding approach efficiently developed high-performance BN-polymer composite films.

I. INTRODUCTION

Polyimides (PIs) are indispensable polymers in our life owing to their excellent physical properties, including mechanical properties, heat and chemical resistance, and good electrical insulation.[1–3] PIs have been used in a variety of products, such as waterproof coatings,[4] speaker components,[5] separators for batteries,[6,7] gas separations,[8,9] water purification membranes,[4,10] and protective materials for space devices.[11–13] However, the rapid development of next-generation electrical products (e.g.,

flexible/wearable smartphones, watches, and sensors, etc.) in recent years requires a further enhancement of the mechanical properties of PIs.[14,15]

It is known that the mechanical properties of PI can be improved by homogeneously dispersing nano-fillers into PI film, which is prepared by *in situ* polymerization of PI monomers.[16–19] However, the pristine nano-fillers have limited compatibility with PI and dispersibility in reaction solvents, leading to phase separation to hamper homogenous composites. Depending on the interactions between nano-fillers and PI matrix, their blending can be divided into the following two types: 1) physical blending; nano-fillers are mechanically mixed with the monomers of PI or polyamic acid (PAA) intermediates,[11,20] and 2) chemical blending; nano-fillers are covalently bonded to the polymer matrix.[21–24] Chemical blending significantly improves the mechanical properties of PI films, because of the strong covalent bond between a nano-filler and PI. The chemical modification of the fillers improves their interaction with PI, as well as dispersibility into the solvents for PI fabrication such DMAc, DMF, and NMP.[2,3,25,26]

To date, various kinds of nano-fillers such as carbon black,[27,28] carbon nanotube (CNT),[29–31] fullerene,[32,33] graphene,[20,34–37] graphene oxide (GO),[34,38–41] and hexagonal boron nitride (h-BN)[42–44] have been utilized to improve the mechanical properties of PI films. Among them, 2D nano-fillers have attracted tremendous attention owing to their large specific surface area and feasibility of functionalization.[45–49] So far, aromatic diamine-functionalized GO has been recognized as an excellent 2D nano-filler, because the excellent dispersibility of GO in solvents leads to uniform composites with PIs. In addition, the amino groups on GO form strong interactions in PI matrix to stabilize the composites.[38,41]

In contrast, h-BN, so-called white graphene, has received less attention than GO, because it has low dispersibility into the organic solvents. To utilize h-BN as a filler for chemical blending, surface functionalization is required. There are several methods for h-BN functionalization, such as plasma treatment, oxidation, and sonication,[50–52] but these methods only provide oxygen functional groups.

Recently, ball milling has received significant attention, because this treatment can achieve exfoliation of bulk h-BN to nanosheets, as well as simultaneous functionalization.[53–55] However, previous researches realized only 1-2 wt% loading of functional groups at the edge of BN framework, which are too low to have good interaction with PI matrix. On the other hand, Mingjun *et al*. reported that h-BN could be well non-covalently functionalized and dispersed in a solvent by π-π interaction with polydopamine.[56] Therefore, we aimed to form two types of interactions; chemical interactions at the edges and the π-π interactions between the basal plane of h-BN and the aromatic moiety of the molecules via ball mill treatment.

First, we produced functionalized h-BN with p-phenylenediamine (PDA) via solid state ball milling method (Fig. 1). To maximize the number of the amino-functional groups in the composite, various kinds of ball milling conditions, such as the weight ratio of h-BN and PDA, ball milling speed and treatment time, were investigated. To obtain a stronger PI film, we further investigated the addition of GO into PI matrix, expecting the synergistic effect on the enhancement of the mechanical properties.

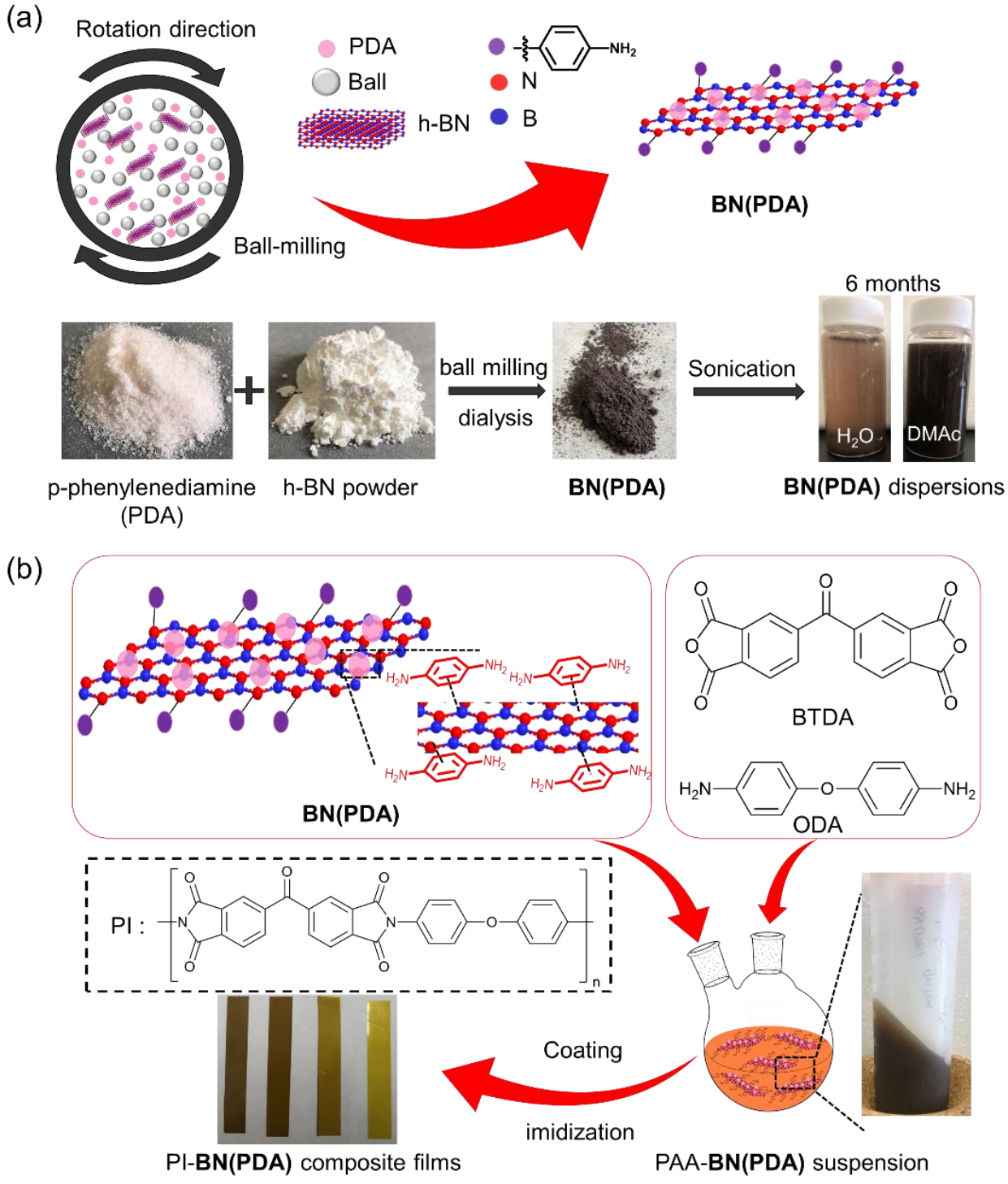

Fig. 1 Schematic illustration of the fabrication of the PI-**BN(PDA)** composite film.

II. RESULTS AND DISCUSSION

II.1 Synthesis and characterization of BN(PDA)

First, functionalized h-BN (**BN(PDA)**) was prepared from h-BN and PDA via solid-state ball milling treatment. To optimize the ball milling parameters for the efficient PDA loading, **BN(PDA)** was prepared under various experimental conditions, including weight ratios of h-BN and PDA (1:0.5, 1:1, and 1:5), rotation speeds of ball mill (200, 500, and 700 rpm), and reaction time (3 and 16 h).

Then, the **BN(PDA)** was characterized by FTIR spectroscopy. As shown in Fig. 2, the peaks at 780 and 1380 cm^{-1} are attributed to the B-N stretching and out-of-plane N-B-N bending of h-BN, respectively.[59,60] The peak at 3240 cm^{-1} is assigned to the N-H stretching of amino groups in PDA.[61] These characteristics indicate that PDA were attached on **BN(PDA)** and that the h-BN structure remained after the ball milling process.

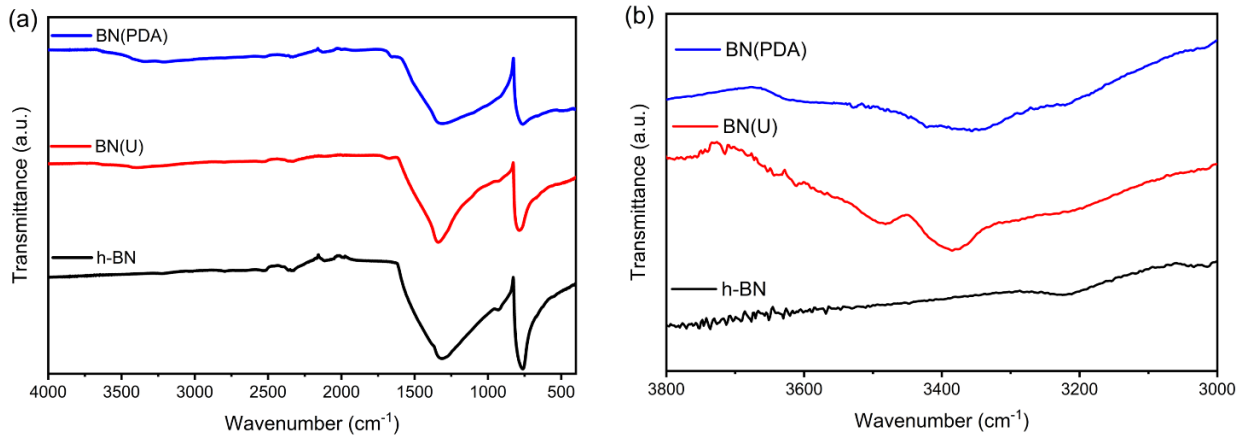

Fig. 2 FT-IR spectra of h-BN, BN(U), and **BN(PDA)**: (a) full range and (b) narrow range.

XPS analysis was conducted to elucidate the chemical state of FBN. Fig. 3a and 3b show B 1s and N 1s spectrum of the raw material. The dominant peak is B-N bond in both spectra. In the B 1s spectrum, there is a slight peak at 193.8 ev,[62,63] which is originated from BO_x. The BO_x peak on the surface of h-BN disappeared after ultrasonic or ball mill treatment of h-BN (Fig. 3a - d). The full width at half maximum (FWHM) of **BN(PDA)** at B 1s and N 1s increased from 1.49 to 1.73 and 1.56 to 1.74 after

ball milling, which means that new chemical bonds are formed and suggests that h-BN and PDA are chemically bonded. Furthermore, the N 1s of **BN(PDA)** shows that, in addition to the main peak N-B (398.2 eV), N-H bond peak appears at 399.6 eV,[54] further proving the successful chemical functionalization of **BN(PDA)**.

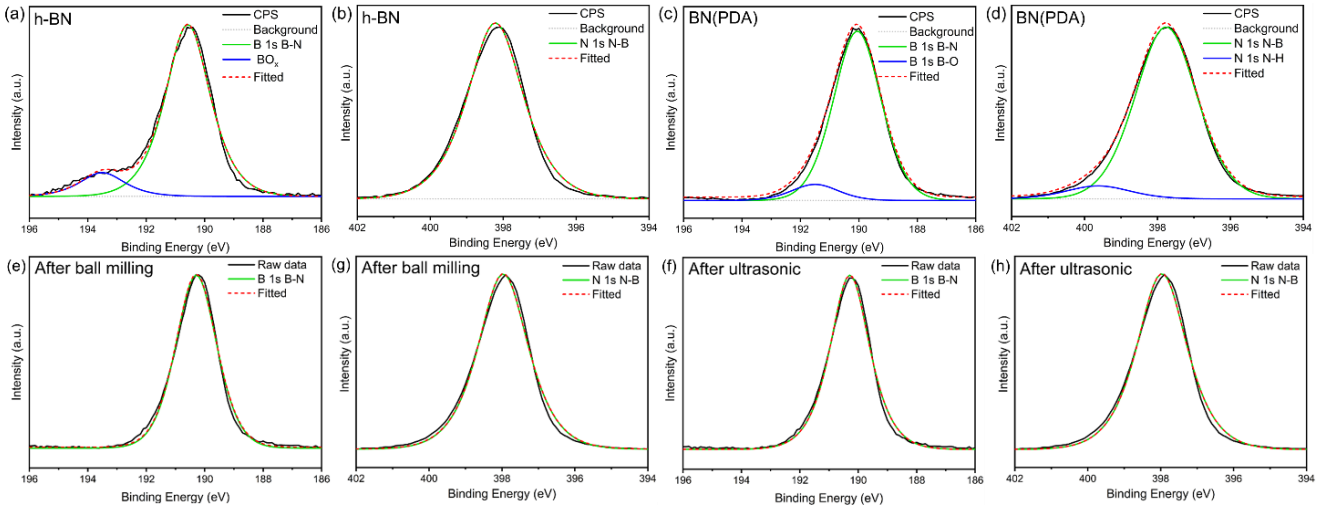

Fig. 3 XPS analysis of h-BN and **BN(PDA) 1:5 700 16 h** (a,c) B 1s and (b,d) N 1s., The Analysis of h-BN in B 1s and N 1s after (e,f) ball milling and (g,f) ultrasonic treatment.

In the next step, **BN(PDA)** was analyzed by TGA to quantify the loading quantity of PDA. As summarized in Table 1, the amount of PDA in **BN(PDA)**, which corresponds to the weight loss at temperatures higher than 400 °C in TGA curves (Fig. 4), was affected by ball milling parameters including the weight ratio, the rotation speed, and the reaction time. Focusing on the rotation speed, at the weight ratio of 1:1 and 16 hours treatment, the loading of PDA increased from 3.26 to 11.37 wt% as the reaction speed increased from 200 to 700 rpm. In terms of the treatment time, longer treatment time increased the loading amount in all cases. From these investigations, we achieved the highest PDA loading (12.06%) under the condition of h-BN:PDA = 1:5 at 700 rpm for 16 h. Interestingly, after ball mill treatment, we found the smell of ammonia (Fig 5), indicating C-N bond cleavage of PDA.[55,64] Therefore, surface covalent functionalization via aryl radical may occur.

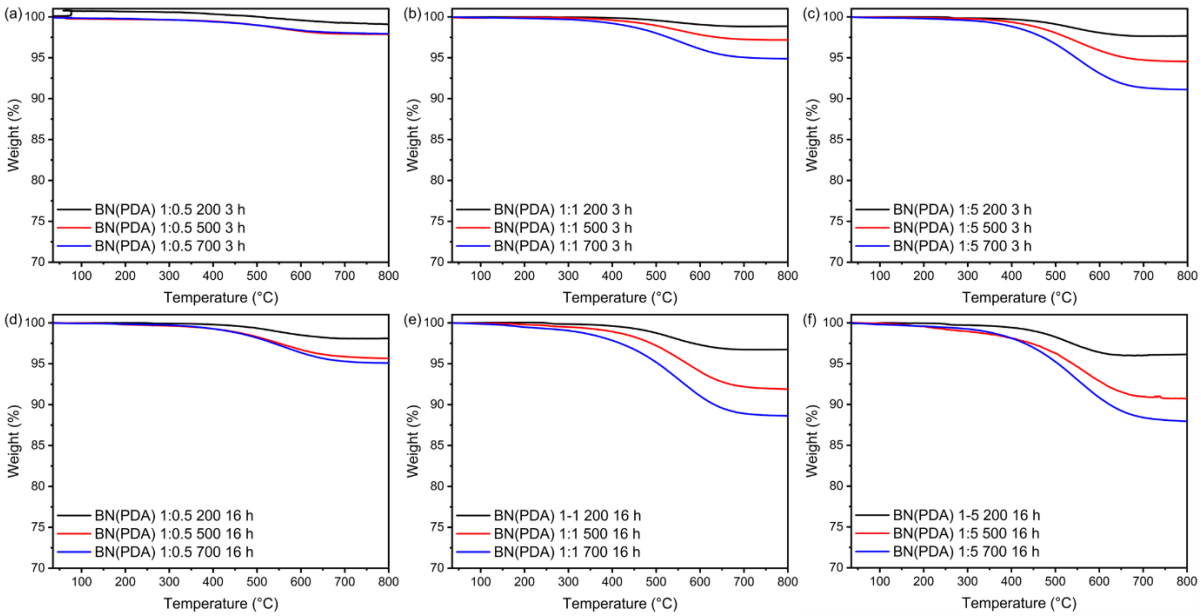

Fig. 4 TGA of **BN(PDA)**: (a-c) ball milling for 3 h and (d-f) ball milling for 16 h.

Fig. 5 Ammonia detection after the ball mill experiment.

Table 1 List of fixed amounts of PDA[a]

h-BN:PDA	Speed (rpm)	Weight loss (%)[b]	
		3 h[c]	16 h[d]
1:0.5	200	0.91	1.89
	500	2.13	4.34
	700	2.05	4.91
1:1	200	1.15	3.26
	500	2.82	8.09
	700	5.12	11.37
1:5	200	2.33	3.86
	500	5.46	9.08
	700	8.90	12.06

[a]h-BN, PDA, and zirconia ball (ø= 5 mm, 10 pieces) were used at room temperature. [b]Weight loss was determined by TGA at 800 °C in air. [c]Ball mill treatment for 3 h. [d]Ball mill treatment for 16 h.

XRD measurements revealed that the speed of ball milling has the most significant effect on the crystallinity of **BN(PDA)** (Fig. 6 and 7). As shown in Fig. 6, sharp peaks were observed at 26.2°, 41.5°, 43.7°, 50.1° and 55.1° in h-BN, which are in agreement with previous characterizations of h-BN.[65–67] Since the FWHM represents the crystal size of h-BN, the gradual increase of FWHM in **BN(PDA)** implies that smaller h-BN flakes are produced as the rotation speed increases. The XRD analysis well explains the relationship between the rotation speed and the loading amount of PDA; higher rotation speed generates smaller-sized h-BN flakes, which facilitate the PDA loading owing to their larger specific surface area and a larger amount of reactive edge sites.

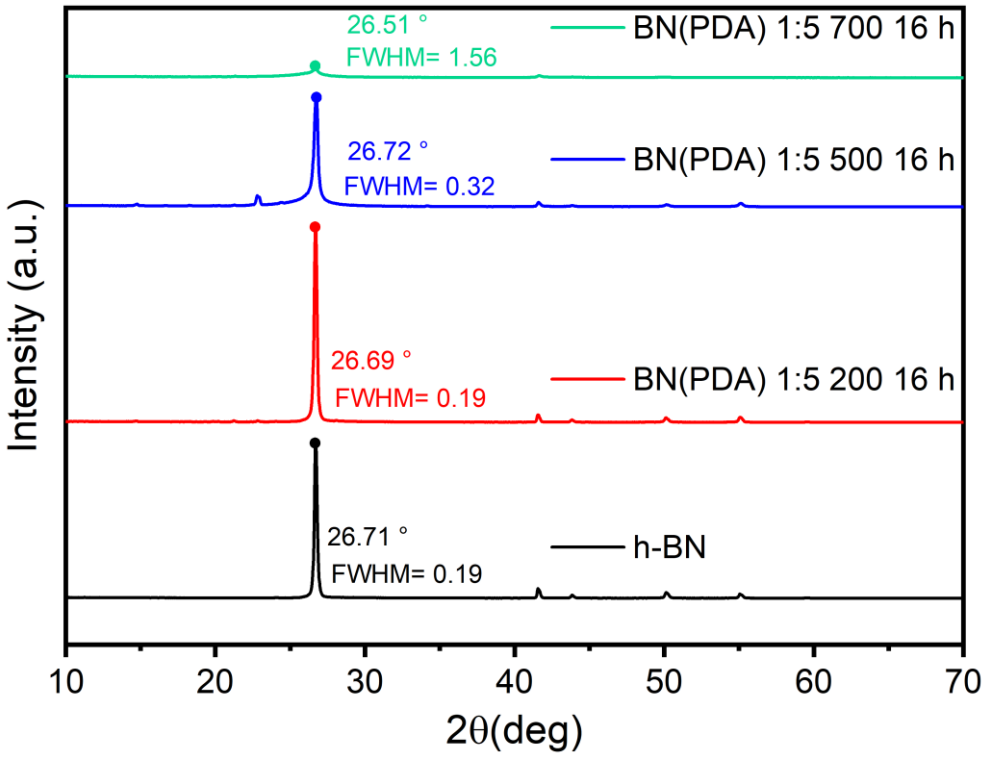

Fig. 6 XRD patterns of h-BN and **BN(PDA)** prepared under different rotation speeds.

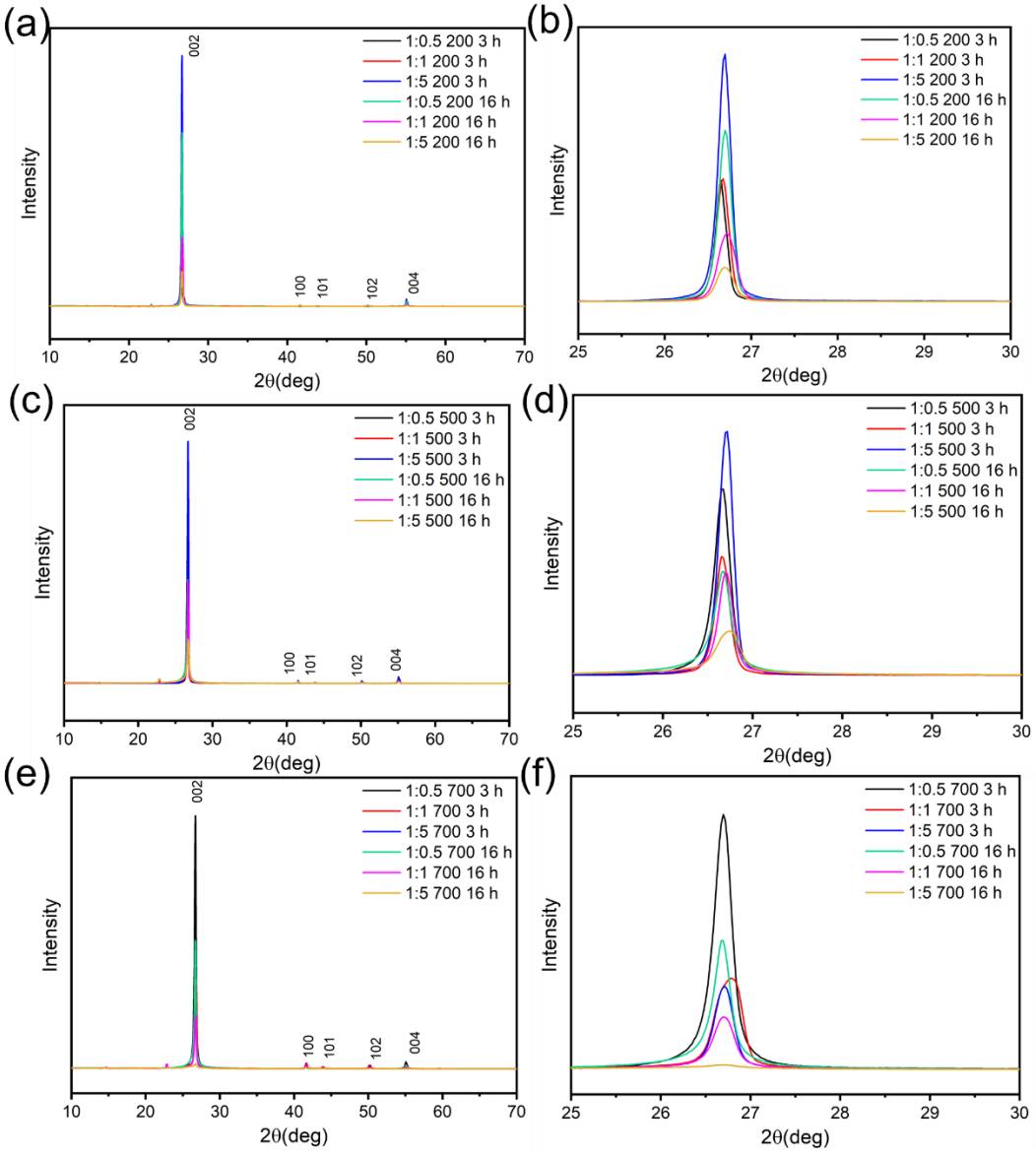

Fig. 7 XRD patterns of **BN(PDA)** in different ball milling treatment. (a-b) 200 rpm with different parameters, (c-d) 500 rpm with different parameters, (e-f) 700 rpm with different parameters.

To confirm the reactivity of amino groups in **BN(PDA)**, we treated **BN(PDA)** with 3,3',4,4'-benzophenonetetracarboxylic dianhydride (BTDA). TGA data of h-BN, BTDA, reaction product between PDA and BTDA (PDA-BTDA), reaction product of h-BN and BTDA (h-BN/BTDA), and **BN(PDA)** treated with BTDA (**BN(PDA)**/BTDA) are presented in Fig. 8. The h-BN/BTDA showed two weight losses of 0.3% and 1.1% at 225 °C and 320 °C, respectively. On the other hand, the **BN(PDA)**/BTDA showed three larger weight losses of 3.7 wt%, 17.1 wt% and 24.1 wt% at 150 °C,

450 °C and 650 °C, respectively, corresponding to the dehydration through imidization, the carbonization reactions and the decomposition of compound originated PDA and BTDA.

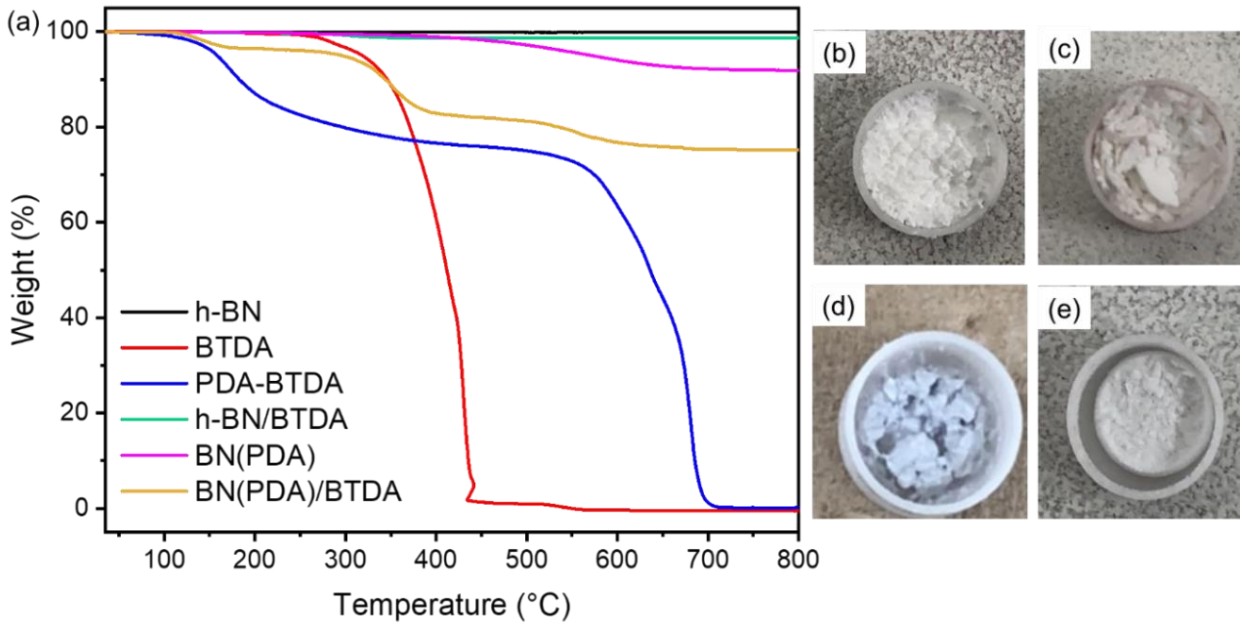

Fig. 8 (a) TGA curves of h-BN, BTDA, PDA-BTDA, h-BN/BTDA, **BN(PDA)**, and **BN(PDA)**/BTDA with a heating rate of 10 °C min^{-1}. (b) h-BN after TGA. (c) h-BN/BTDA after TGA. (d) **BN(PDA)** after TGA (e) **BN(PDA)**/BTDA after TGA.

A similar pattern was observed for PDA-BTDA specimens. Furthermore, FTIR spectra of **BN(PDA)**/BTDA showed an additional C=O stretching vibration peak at 1720 cm^{-1} and the decrease of NH stretch vibration at 3200 cm^{-1} (Fig. 9).[68–70] Therefore, the above descriptions indicate that the PDA on h-BN can bond with BTDA through an amide bond. In addition, the C=O vibrations were not observed for h-BN/BTDA, indicating BTDA was not attached on pristine h-BN and PDA functionalization is indispensable for the chemical blending of h-BN in PI.

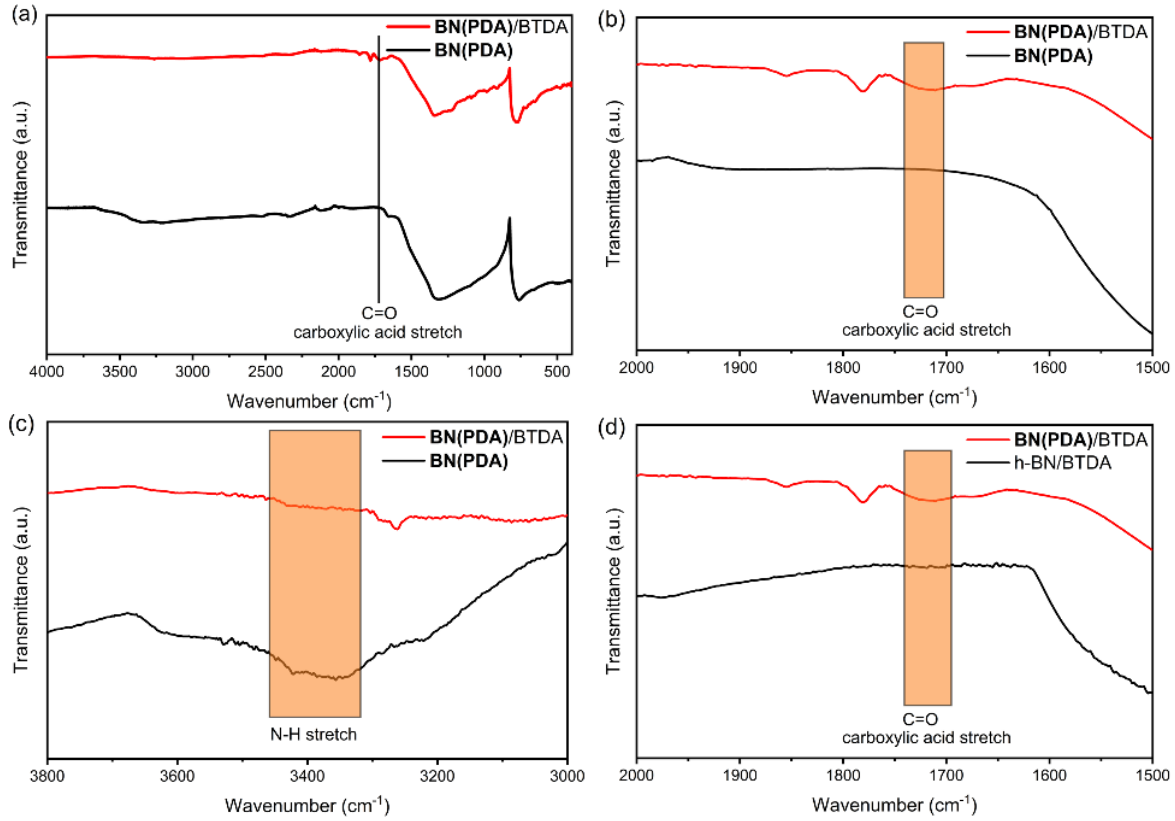

Fig. 9 FT-IR spectra of **BN(PDA), BN(PDA)**/BTDA: (a)~(c). **BN(PDA)**/BTDA and h-BN/BTDA comparison: (b). (a) full range, (b) narrow range around C=O peak, (c) narrow range around NH stretch peak, (d) **BN(PDA)**/BTDA and h-BN/BTDA full range.

II.2 The kinetic energy modeling and mechanistic study of ball milling

To gain deep insights into the effect of rotation speed on the efficacy of PDA loading, the kinetic energy of the ball milling at various speeds (200, 300, 400, 500, 600, and 700 rpm) were calculated by eq.1[71–73] and correlated to PDA content in TGA.

$$\Delta E = -m_b\left[\frac{\omega_v^3\left(R_v-\frac{d_b}{2}\right)}{\omega_p}+\omega_v\omega_p R_p\right]\left(R_v-\frac{d_b}{2}\right) \qquad (1)$$

In this equation, ΔE, m_b, ω_p, ω_v, R_p, R_v, and d_b correspond to impact energy of a single ball, weight of the ball, rotation speed of the instrument, rotation speed of the container, rolling radius of equipment, rolling radius of milling jar, and the radius of milling jar, respectively.[71–73]

The detailed values of the above parameters are specified in Table 2. A positive correlation between the impact energy and the PDA content was evidenced from the calculation (Fig. 10), showing that both parameters increased as the rotation speed increased from 200 to 700 rpm. As a further interpretation, we found a linear relationship between the kinetic energy and the PDA content. This implies that the rotation speed increases the loading of PDA by increasing the impact energy of the ball milling. According to the above calculation, the energy of one impact energy is around 2 mJ-18 mJ. Suppose that the ball strikes the chemicals with a volume of 0.001 mm3, the impact energy for each molecule is about 3.15×10-16 mJ to 2.84×10-15 mJ. A bond dissociation energy of C-N bond and B-N bond is 4.82×10-16 mJ and 6.28×10-16 mJ, respectively,72 which confirms that the ball mill can break the bonds.

Table. 2 Parameters of the planetary ball mill

R_v	26.5 mm
R_p	67.2 mm
ω_v/ω_p	-2
d_b	5 mm
m_b	4.4 g

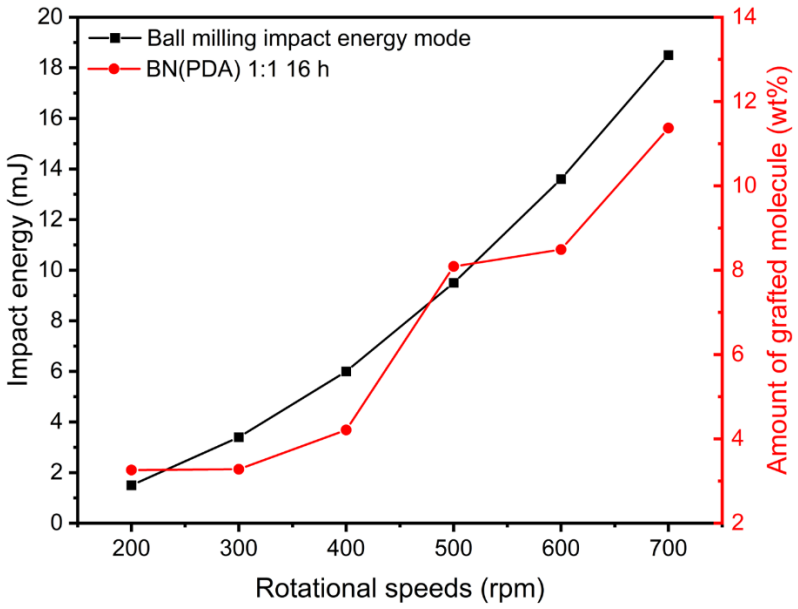

Fig. 10 Schematic of the planetary ball mill. Amount of grafted molecule was determined by TGA weight loss until 800 °C

II.3 Preparation of polyimide composites and their mechanical properties

The characterization of **BN(PDA)** revealed the presence of NH_2 on its surface; therefore, we applied this material as a filler of polyimide. Various **BN(PDA)**, such as **BN(PDA) 1:1 500 16 h**, were reacted with 4,4'-Diaminodiphenyl ether (ODA) and BTDA to form polyimide-**BN(PDA)** composites (PI-**BN(PDA)**). Detailed synthesis procedure is shown in the experimental section.

The mechanical properties of PI-**BN(PDA)**, including tensile strength, tensile modulus, and elongation, were evaluated by tensile test. The addition of pristine h-BN without PDA modification into PI (PI-h-BN) also increased the tensile strength and tensile modulus of PI to 18 and 22%, respectively (Table 3, Entry 2). These enhancements may be caused by the surface roughness of h-BN, according to a previous study.[74] As compared to PI-h-BN, the PI-**BN(PDA)** showed better mechanical properties. As shown in Table 3 and Table 4, the highest tensile strength and tensile modulus of PI-**BN(PDA) 1:1 500 16 h** composite films were observed as 151.1 MPa and 3.8 GPa, which were 57.8% and 58.3% higher than those of the pristine PI. In addition, when the amount of **BN(PDA) 1:1 500 16 h** increased from 1 wt% to 3 wt% or 5 wt% in PI, the tensile strength and tensile modulus both decreased (Table 3, Entry 4 and Table 4, Entry 2 and 3). These results indicate that excess **BN(PDA)** leads to a reduction of the positive effects of the material in the PI matrix, probably because the abundant **BN(PDA)** causes aggregation, which deteriorates the mechanical properties. Therefore, we can determine 1 wt% addition of **BN(PDA) 1:1 500 16 h** to be optimal in PI film.

To further understand the effect of ball milling parameters on the PI composite films, we plotted the loaded amount of PDA on h-BN and the mechanical properties of PI composite films (Fig. 10). When the loading amount of PDA was 1-6 wt%, the tensile strength increased as the amounts of PDA increased. However, further increase of PDA decreased the strength of the film. This demonstrates that the amount of PDA on the h-BN surface affects the mechanical properties of PI composite films.

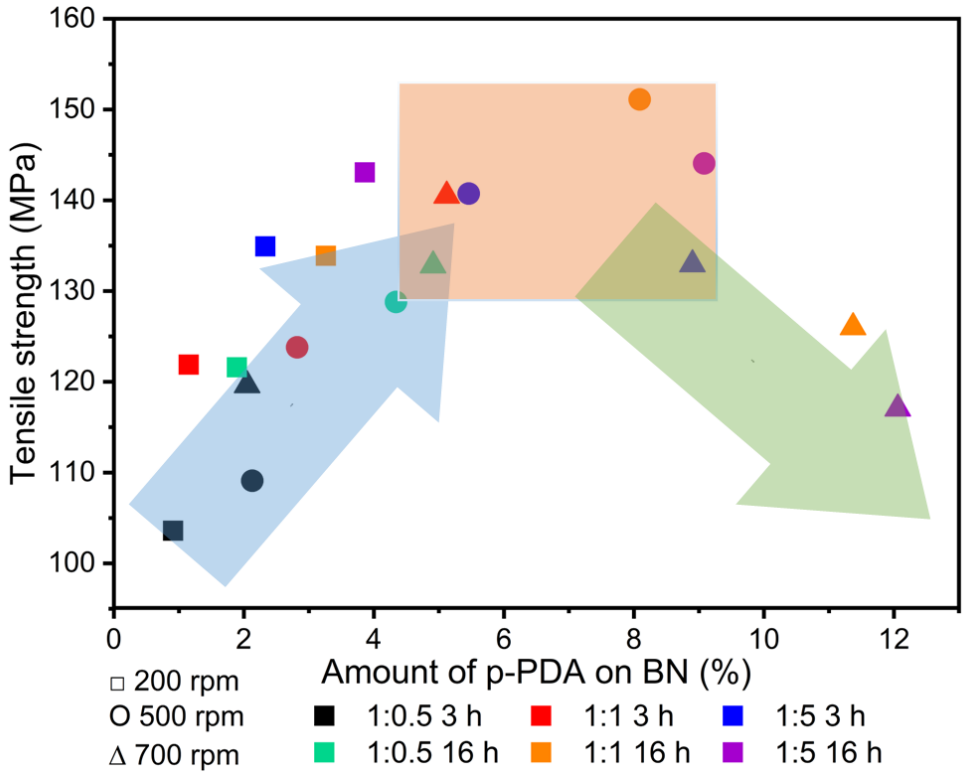

Fig. 10 The curves of the tensile strength with amount of PDA on h-BN.

Finally, **BN(PDA) 1:1 500 16 h** was combined with GO in PI film for further improvement. PI films with both **BN(PDA)** and GO showed higher mechanical properties than the PI containing only **BN(PDA)**. According to Table 4, the tensile strength and tensile modulus of **BN(PDA)**/GO composite fillers were 28% and 30% higher than those of h-BN/GO fillers (Table 5, Entry 1 and 2). This proved the functionalization of h-BN with PDA improves mechanical properties of the composite film. In addition, PI-**BN(PDA)**/GO composite film has a tensile strength of 159.2 MPa, which is 66% higher than that of the pristine PI, and the tensile modulus was increased to 3.9 GPa, which is 63% higher (Table 3, Entry 1). By reducing the amount of **BN(PDA)**/GO to 3 wt%, the tensile strength and tensile modulus both decreased (Table 5, Entry 3 and 5). When the **BN(PDA)**: GO ratio increased to 10: 1, the tensile strength dropped to 135.3 MPa and the tensile modulus also dropped to 3.1 GPa (Table 5, Entry 4). Furthermore, these data also revealed that the ratio of **BN(PDA)** and GO strongly affects PI film mechanical properties.

Table 3. Mechanical properties of pristine PI, PI-hBN, PI-**BN(PDA)** films.

Entry	Filler	h-BN:PDA	Ball milling of speed (rpm)	Tensile strength (MPa)	Tensile modulus (GPa)
1	-	-	-	95.7 ± 15.6	2.4 ± 0.4
2	h-BN[a]	-	-	110.9 ± 7.0	2.7 ± 0.1
3			200	103.6 ± 3.1	2.6 ± 0.3
4		1:0.5	500	109.1 ± 5.3	2.7 ± 0.1
5			700	119.6 ± 4.2	2.9 ± 0.2
6			200	121.9 ± 6.9	3.0 ± 0.2
7	BN(PDA)[a,x]	1:1	500	123.8 ± 7.3	2.8 ± 0.1
8			700	140.5 ± 7.5	3.5 ± 0.4
9			200	134.9 ± 12.4	3.1 ± 0.2
10		1:5	500	140.7 ± 9.9	3.3 ± 0.2
11			700	132.9 ± 7.8	3.1 ± 0.2
12			200	121.6 ± 2.7	2.7 ± 0.1
13		1:0.5	500	128.8 ± 5.9	3.2 ± 0.2
14			700	132.8 ± 6.2	3.3 ± 0.3
15			200	133.9 ± 11.1	3.4 ± 0.2
16	BN(PDA)[a,y]	1:1	500	151.1 ± 3.1	3.8 ± 0.2
17			700	126.0 ± 7.6	3.1 ± 0.2
18			200	143.1 ± 6.7	3.7 ± 0.1
19		1:5	500	144.1 ± 7.2	3.6 ± 0.2
20			700	117.0 ± 11.1	3.1 ± 0.2

[a]1 wt% sample for PI matrix was used in this table. [x]Ball mill was performed for 3 h to prepare **BN(PDA)**. [y]Ball mill was performed for 16 h to prepare **BN(PDA)**.

Table 4. Mechanical properties of PI-**BN(PDA) 1-1 500 16 h** films[z,x]

Entry	Percentage of filler in PI (wt%)	Tensile strength (MPa)	Tensile modulus (GPa)
1	1	151.1 ± 3.1	3.8 ± 0.2
2	3	134.4 ± 3.4	3.4 ± 0.1
3	5	135.1 ± 3.4	3.8 ± 0.3

[z]Ball mill was performed for 500 rpm to prepare **BN(PDA)**. [x]Ball mill was performed for 16 h to prepare **BN(PDA)**.

Table 5. Mechanical Properties of PI-**BN(PDA)**/GO films.

Entry	Filler	BN(PDA):GO	Tensile strength (MPa)	Tensile modulus (GPa)
1	h-BN/GO[a]	100:1	124.8 ± 5.8	3.0 ± 0.2
2	BN(PDA)/GO[a]	100:1	159.2 ± 4.1	3.9 ± 0.3
3	BN(PDA)/GO[b]	100:1	138.4 ± 3.9	3.5 ± 0.2
4	BN(PDA)/GO[a]	10:1	135.3 ± 2.7	3.1 ± 0.2
5	BN(PDA)/GO[b]	10:1	125.8 ± 6.6	3.3 ± 0.3

[a]1 wt% filler for PI matrix was used in this table. [b]3 wt% filler for PI matrix was used in this table.

III. CONCLUSIONS

In this study, we have elucidated, for the first time, the correlation between the total amount of functional groups within **BN(PDA)** and the mechanical properties of PI films through the ball milling treatment with various parameters. We found that rotation speed is the most significant parameter for the functionalization. There is the optimum amount of the functional groups for the mechanical strength. When the total amount of functional groups reached 8 wt%, the tensile strength and tensile modulus of PI composite films were the highest in this study (57.8% and 58.3% higher than the pristine PI). Moreover, the addition of a small amount of GO to PI-**BN(PDA)** improves the tensile strength and tensile modulus by 5.4% and 2.6% compared to PI-**BN(PDA)**. Consequently, controlled **BN(PDA)** functionalization can be useful for future applications as mechanically enriched composites.

We experimentally demonstrated that PI mechanical properties can be improved by modifying the ball milling parameters for **BN(PDA)** and adding GO. Chemical bondings at the edges of h-BN and the π-π interaction between the basal plane of h-BN and the aromatic moiety of PDA increases the amount of reactive NH_2 groups, thereby improving the interaction with the raw materials of PI. On the other hand, covering the **BN(PDA)** surface with GO creates additional interaction between the raw material of PI. Therefore, larger amount of PI can be grafted both on surfaces and edges, which enhances the mechanical properties of PI composite film. In contrast, the excess amount of GO that is not attached to the h-BN surface deteriorates the mechanical properties of the composite. Our results and the proposed mechanism will be useful guidelines for fabricating 2D composite materials in polymer matrixes.

IV. EXPERIMENTAL SECTION

IV.1 Materials

Hexagonal boron nitride (h-BN) with an average size of 1-2 μm was obtained from Showa Denko K.K., Tokyo, Japan. p-Phenylenediamine (PDA, purity 97.0+%), 3,3',4,4'-benzophenonetetracarboxylic dianhydride (BTDA, purity 96.0+%), 4,4'-diaminodiphenyl ether (ODA, purity 99.0+%), dimethylacetamide (DMAc, purity 98.0+%), sulfuric acid (H_2SO_4, purity 95.0+%), and potassium permanganate ($KMnO_4$, purity 99.3+%) were purchased from FUJIFILM Wako Pure Chemical Corporation, Osaka, Japan. Graphene oxide (GO) was prepared according to Hummers' method with a slight modification.[57,58]

IV.2 Characterization instruments

Fourier transform infrared spectroscopy (FTIR) spectra of samples were recorded on a IRTracer-100 (Shimadzu, Japan) in the wavenumber range of 400 to 4000 cm^{-1}. X-ray diffraction (XRD) measurements were performed on AERIS equipped with single crystalline silicon (Panalytical, Netherlands). X-ray photoelectron spectroscopy (XPS) was carried out on a JPS-9030 (JEOL, Japan) with a pass energy of 20 eV. Thermal gravimetric analyses (TGA) were measured from room temperature to 800 °C at a heating rate of 10 °C min^{-1} under air on a DTG-60AH (Shimadzu, Japan). The tensile strength of PI films (10 mm × 60 mm) was tested using a Universal Testing Machine AG-Xplus (Shimadzu, Japan) at a tensile testing rate of 1 mm/min.

IV.3 Preparation of PDA-functionalized hexagonal boron nitride (BN(PDA))

BN(PDA) was prepared using a ball mill Pulverisette 7 classic line (Fritsch, Germany) under different conditions. In detail, h-BN and PDA were mixed at weight ratios of 1:0.5, 1:1, or 1:5 in a milling container, and stirred at rotation speeds of 200, 500, or 700 rpm for 3 or 16 h at room temperature. The resulting product was purified by dialysis (membrane cutoff: 12-14 kDa) in deionized water until pH

reached 8-7. To confirm a complete removal of unreacted PDA, the dialyzed solution at various pH values (11-10, 10-9, and 8-7) were analyzed by FTIR spectra after drying (Fig. 11). At pH 8-7, peak of PDA was not detected, suggesting the completion of dialysis. Finally, the sample was sonicated for 10 min and freeze-dried for further use.

Hereafter, we call the yielded **BN(PDA)** as **BN(PDA)x y z** where x, y and z mean weight ratios, rotation speed and reaction time, respectively.

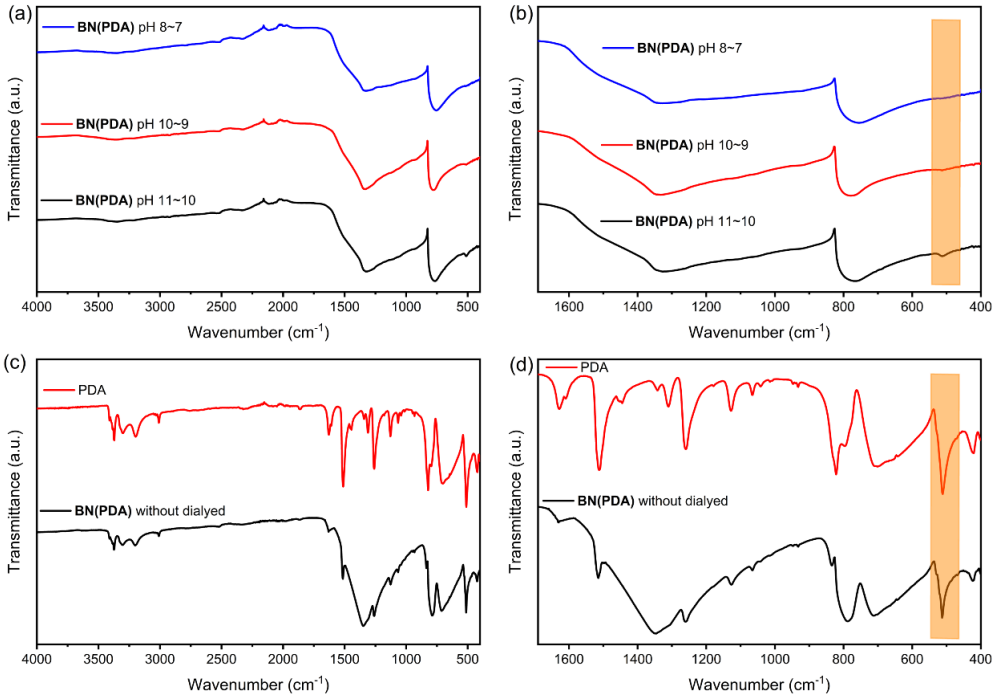

Fig. 11 (a-b) FT-IR spectra of **BN(PDA)** after dialysis with three different pH (8-7, 10-9, 11-10). (a) full range and (b) narrow range. (c-d) FT-IR spectra of PDA and **BN(PDA)** before dialysis. (c) full range and (d) narrow range.

IV.4 Preparation of PI-BN(PDA) composite films

To prepare different concentrations of PAA-**BN(PDA)** suspension, different amount of **BN(PDA) 1:1 500 16 h** (0.053 g, 0.161 g, or 0.274 g) was dispersed in DMAc (20 ml) by sonication for 1h. Then, ODA (2.0 g, 10 mmol) was added to the **BN(PDA)** suspension by sonication for 10 min. Finally, BTDA (3.2 g, 10 mmol) was added to the suspension, sonicated for 10 min, and kept at -20 °C as a stock suspension of PAA-**BN(PDA)**.

The film samples were produced by coating PAA-**BN(PDA)** suspension on a glass plate and heating it at 90 °C for 1h (heating speed 1 °C/min under nitrogen) until the solvent was evaporated. A further heat-treatment was performed at 300 °C for 1h (room temperature to 300 °C for 5 h under nitrogen).

IV.5 Preparation of PI-BN(PDA)/GO composite films

BN(PDA)/GO with 2 different ratios (100:1 and 10:1) was dispersed in DMAc (20 ml) by sonication for 1h. Then, ODA (2.0 g, 10 mmol) was added to the **BN(PDA)**/GO homogeneous suspension, and further homogenized by sonication for 10 min. Next, BTDA (3.2 g, 10 mmol) was added into the solution and sonicated for 10 min to form PAA-**BN(PDA)**/GO. PAA-**BN(PDA)**/GO solution was loaded on a glass plate and heated at 90 °C for 1h (heating speed 1 °C/min under nitrogen) until the solvent was evaporated. A further heat-treatment was performed at 300 °C for 1h (room temperature to 300 °C for 5 h under nitrogen).

The PI-**BN(PDA)**/GO composites films containing 1 wt%, 3 wt% of **BN(PDA)**/GO were prepared by the same experimental steps.

REFERENCES

1. Agag, T., Koga, T. & Takeichi, T. Studies on thermal and mechanical properties of polyimide-clay nanocomposites. *Polymer* **42**, 3399–3408 (2001).
2. Bernards, D. A. & Desai, T. A. Nanoscale porosity in polymer films: Fabrication and therapeutic applications. *Soft Matter* **6**, 1621–1631 (2010).
3. Ogieglo, W., Wormeester, H., Eichhorn, K. J., Wessling, M. & Benes, N. E. In situ ellipsometry studies on swelling of thin polymer films: A review. *Prog Polym Sci* **42**, 42–78 (2015).
4. Chen, G. Q., Scholes, C. A., Qiao, G. G. & Kentish, S. E. Water vapor permeation in polyimide membranes. *J Memb Sci* **379**, 479–487 (2011).
5. Shearwood, C., Harradine, M. A., Birch, T. S. & Stevens, J. C. Applications of polyimide membranes to MEMS technology. *Microelectron Eng* **30**, 547–550 (1996).
6. Miao, Y. E., Zhu, G. N., Hou, H., Xia, Y. Y. & Liu, T. Electrospun polyimide nanofiber-based nonwoven separators for lithium-ion batteries. *J Power Sources* **226**, 82–86 (2013).
7. Wang, H. G. *et al.* Tailored aromatic carbonyl derivative polyimides for high-power and long-cycle sodium-organic batteries. *Adv Energy Mater* **4**, 1–7 (2014).
8. Coleman, M. R. & Koros, W. J. Isomeric polyimides based on fluorinated dianhydrides and diamines for gas separation applications. *J Memb Sci* **50**, 285–297 (1990).
9. Wang, Y. *et al.* Functionalized Boron Nitride Nanosheets: A Thermally Rearranged Polymer Nanocomposite Membrane for Hydrogen Separation. *Angewandte Chemie* **130**, 16288–16293 (2018).
10. Minelli, M. *et al.* Vapor and liquid sorption in matrimid polyimide: Experimental characterization and modeling. *Ind Eng Chem Res* **52**, 8936–8945 (2013).
11. Guerra, G., Williams, D. J., Karasz, F. E. & MacKnight, W. J. Miscible polybenzimidazole blends with a benzophenone-based polyimide. *J Polym Sci B Polym Phys* **26**, 301–313 (1988).
12. Loeblein, M. *et al.* 3D Graphene-Infused Polyimide with Enhanced Electrothermal Performance for Long-Term Flexible Space Applications. *Small* **11**, 6425–6434 (2015).
13. Komamura, T., Okuhara, K., Horiuchi, S., Nabae, Y. & Hayakawa, T. Fabrication of Well-Ordered Mesoporous Polyimide Films by a Soft-Template Method. *ACS Appl Polym Mater* **1**, 1209–1219 (2019).
14. Liaw, D. J. *et al.* Advanced polyimide materials: Syntheses, physical properties and applications. *Progress in Polymer Science* vol. 37 907–974 Preprint at https://doi.org/10.1016/j.progpolymsci.2012.02.005 (2012).
15. Ni, H. jiang, Liu, J. gang, Wang, Z. he & Yang, S. yong. A review on colorless and optically transparent polyimide films: Chemistry, process and engineering applications. *Journal of Industrial and Engineering Chemistry* **28**, 16–27 (2015).
16. Wu, Y. W., Zhang, W. C. & Yang, R. J. Ultralight and Low Thermal Conductivity Polyimide–Polyhedral Oligomeric Silsesquioxanes Aerogels. *Macromol Mater Eng* **303**, 1–12 (2018).

17. Zhang, L. *et al.* Polyimide/ladder-like polysilsesquioxane hybrid films: Mechanical performance, microstructure and phase separation behaviors. *Compos B Eng* **56**, 808–814 (2014).
18. Wu, Z., He, J., Yang, H. & Yang, S. Progress in Aromatic Polyimide Films for Electronic Applications: Preparation, Structure and Properties. *Polymers (Basel)* **14**, 1–34 (2022).
19. Ghosh, A., Sen, S. K., Banerjee, S. & Voit, B. Solubility improvements in aromatic polyimides by macromolecular engineering. *RSC Adv* **2**, 5900–5926 (2012).
20. Hones, H. M., Bielicki, T. J., Mccaffrey, M. J., Chao, R. & Cook, J. T. Polyimide-based Nanocomposites as Low- Temperature Dielectrics. *IEEE Nanotechnology Materials and Devices Conference* 8–11 (2019).
21. Min, C. K., Wu, T. B., Yang, W. T. & Chen, C. L. Functionalized mesoporous silica/polyimide nanocomposite thin films with improved mechanical properties and low dielectric constant. *Compos Sci Technol* **68**, 1570–1578 (2008).
22. Yang, Z., Peng, H., Wang, W. & Liu, T. Crystallization behavior of poly(ε-caprolactone)/layered double hydroxide nanocomposites. *J Appl Polym Sci* **116**, 2658–2667 (2010).
23. Gu, H. *et al.* Effect of interphase and strain-rate on the tensile properties of polyamide 6 reinforced with functionalized silica nanoparticles. *Compos Sci Technol* **75**, 62–69 (2013).
24. Mohamed, M. G. & Kuo, S. W. Functional polyimide/polyhedral oligomeric silsesquioxane nanocomposites. *Polymers (Basel)* **11**, (2019).
25. Tyan, H. L., Leu, C. M. & Wei, K. H. Effect of reactivity of organics-modified montmorillonite on the thermal and mechanical properties of montmorillonite/polyimide nanocomposites. *Chemistry of Materials* **13**, 222–226 (2001).
26. Bernards, D. A. & Desai, T. A. Nanoscale porosity in polymer films: Fabrication and therapeutic applications. *Soft Matter* **6**, 1621–1631 (2010).
27. Wu, S., Hayakawa, T., Kakimoto, M. A. & Oikawa, H. Synthesis and characterization of organosoluble aromatic polyimides containing POSS in main chain derived from double-decker-shaped silsesquioxane. *Macromolecules* **41**, 3481–3487 (2008).
28. Lin, J. S. & Chiu, H. T. Preparation and properties of conductive polyimide films. *Journal of Polymer Research* **9**, 189–194 (2002).
29. Fukushi, Y. *et al.* Fabrication and characterization of glucose fuel cells with a microchannel fabricated on flexible polyimide film. *Journal of Photopolymer Science and Technology* **26**, 303–308 (2013).
30. Cui, C. *et al.* High strength composites using interlocking carbon nanotubes in a polyimide matrix. *Carbon.* **60**, 102–108 (2013).
31. Ning, W. *et al.* Multifunctional super-aligned carbon nanotube/polyimide composite film heaters and actuators. *Carbon.* **139**, 1136–1143 (2018).
32. Lebrón-Colón, M. *et al.* Reinforced thermoplastic polyimide with dispersed functionalized single wall carbon Nanotubes. *ACS Appl Mater Interfaces* **2**, 669–676 (2010).

33. Ganeev, R. A. *et al.* Frequency conversion of picosecond radiation in fullerene-doped polyimide films and colloidal metals. *Journal of Optics B: Quantum and Semiclassical Optics* **3**, 88–92 (2001).
34. Kamanina, N. V., Kaporskii A, L. N. & Kotov, B. V. Absorption spectra and optical limiting of the fullerene-polyimide system. *Opt Commun* **152**, 280–282 (1998).
35. Chen, Z., Tong, F., Zhu, D., Lu, X. & Lu, Q. Ductile Polyimide/Reduced Graphene Oxide Nanohybrid Films with Porous Structure Fabricated by a Green Hydrogel Strategy. *ACS Appl Polym Mater* **1**, 914–923 (2019).
36. Kim, K. *et al.* Effect of defect-healing in graphene nanosheets on the mechanical properties of polyimide nanocomposites. *Carbon.* **122**, 614–621 (2017).
37. Luong, N. D. *et al.* Enhanced mechanical and electrical properties of polyimide film by graphene sheets via in situ polymerization. *Polymer* **52**, 5237–5242 (2011).
38. Marashdeh, W. F., Longun, J. & Iroh, J. O. Relaxation behavior and activation energy of relaxation for polyimide and polyimide-graphene nanocomposite. *J Appl Polym Sci* **133**, 1–8 (2016).
39. Liao, W. H. *et al.* Effect of molecular chain length on the mechanical and thermal properties of amine-functionalized graphene oxide/polyimide composite films prepared by in situ polymerization. *ACS Appl Mater Interfaces* **5**, 869–877 (2013).
40. Chen, D., Zhu, H. & Liu, T. In situ thermal preparation of polyimide nanocomposite films containing functionalized graphene sheets. *ACS Appl Mater Interfaces* **2**, 3702–3708 (2010).
41. Kong, J. Y. *et al.* Preparation and properties of polyimide/graphene oxide nanocomposite films with Mg ion crosslinker. *Eur Polym J* **48**, 1394–1405 (2012).
42. Wang, J. Y. *et al.* Preparation and properties of graphene oxide/polyimide composite films with low dielectric constant and ultrahigh strength via in situ polymerization. *J Mater Chem* **21**, 13569–13575 (2011).
43. Wang, J. *et al.* Lightweight, Superelastic Yet Thermoconductive Boron Nitride Nanocomposite Aerogel for Thermal Energy Regulation. *ACS Nano* **13**, 7860–7870 (2019).
44. Tsai, M. H., Tseng, I. H., Chiang, J. C. & Li, J. J. Flexible polyimide films hybrid with functionalized boron nitride and graphene oxide simultaneously to improve thermal conduction and dimensional stability. *ACS Appl Mater Interfaces* **6**, 8639–8645 (2014).
45. Zhang, S. *et al.* Synthesis of pyridine-containing diamine and properties of its polyimides and polyimide/hexagonal boron nitride composite films. *Compos Sci Technol* **152**, 165–172 (2017).
46. Lee, C., Wei, X., Kysar, J. W. & Hone, J. of Monolayer Graphene. *Science (1979)* **321**, 385–388 (2008).
47. Dikin, D. A. *et al.* Preparation and characterization of graphene oxide paper. *Nature* **448**, 457–460 (2007).
48. Falin, A. *et al.* Mechanical properties of atomically thin boron nitride and the role of interlayer interactions. *Nat Commun* **8**, 1–9 (2017).

49. Cai, Q. *et al.* Molecule-Induced Conformational Change in Boron Nitride Nanosheets with Enhanced Surface Adsorption. *Adv Funct Mater* **26**, 8202–8210 (2016).
50. Balandin, A. A. *et al.* Superior thermal conductivity of single-layer graphene. *Nano Lett* **8**, 902–907 (2008).
51. Sainsbury, T. *et al.* Dibromocarbene functionalization of boron nitride nanosheets: Toward band gap manipulation and nanocomposite applications. *Chemistry of Materials* **26**, 7039–7050 (2014).
52. Pakdel, A., Bando, Y. & Golberg, D. Plasma-assisted interface engineering of boron nitride nanostructure films. *ACS Nano* **8**, 10631–10639 (2014).
53. Sainsbury, T. *et al.* Oxygen radical functionalization of boron nitride nanosheets. *J Am Chem Soc* **134**, 18758–18771 (2012).
54. Lee, D. *et al.* Scalable exfoliation process for highly soluble boron nitride nanoplatelets by hydroxide-assisted ball milling. *Nano Lett* **15**, 1238–1244 (2015).
55. Chen, C. *et al.* Functionalized boron nitride membranes with ultrafast solvent transport performance for molecular separation. *Nat Commun* **9**, (2018).
56. Lei, W. *et al.* Boron nitride colloidal solutions, ultralight aerogels and freestanding membranes through one-step exfoliation and functionalization. *Nat Commun* **6**, 1–8 (2015).
57. Cui, M. *et al.* Non-covalent functionalized hexagonal boron nitride nanoplatelets to improve corrosion and wear resistance of epoxy coatings. *RSC Adv* **7**, 44043–44053 (2017).
58. Kim, K. S. *et al.* Hydrogen-catalyzed, pilot-scale production of small-diameter boron nitride nanotubes and their macroscopic assemblies. *ACS Nano* **8**, 6211–6220 (2014).
59. Weng, Q. *et al.* Highly water-soluble, porous, and biocompatible boron nitrides for anticancer drug delivery. *ACS Nano* **8**, 6123–6130 (2014).
60. Lei, W., Portehault, D., Dimova, R. & Antonietti, M. Boron carbon nitride nanostructures from salt melts: Tunable water-soluble phosphors. *J Am Chem Soc* **133**, 7121–7127 (2011).
61. Liu, Z. *et al.* Plasma Tuning Local Environment of Hexagonal Boron Nitride for Oxidative Dehydrogenation of Propane. *Angewandte Chemie - International Edition* **60**, 19691–19695 (2021).
62. Matveev, A. T. *et al.* New insights into synthesis of nanocrystalline hexagonal BN. *Ceram Int* **46**, 19866–19872 (2020).
63. Lin, Y. *et al.* Aqueous dispersions of few-layered and monolayered hexagonal boron nitride nanosheets from sonication-assisted hydrolysis: Critical role of water. *Journal of Physical Chemistry C* **115**, 2679–2685 (2011).
64. Matović, B. *et al.* Synthesis and characterization of nanocrystaline hexagonal boron nitride powders: XRD and luminescence properties. *Ceram Int* **42**, 16655–16658 (2016).
65. Li, S., Lu, X., Lou, Y., Liu, K. & Zou, B. The Synthesis and Characterization of h-BN Nanosheets with High Yield and Crystallinity. *ACS Omega* **6**, 27814–27822 (2021).
66. Guerra, V. *et al.* 2D boron nitride nanosheets (BNNS) prepared by high-pressure homogenisation: Structure and morphology. *Nanoscale* **10**, 19469–19477 (2018).

67. Gershevitz, O. & Sukenik, C. N. In Situ FTIR-ATR Analysis and Titration of Carboxylic Acid-Terminated SAMs. *J Am Chem Soc* **126**, 482–483 (2004).
68. Starsinic, M., Taylor, R. L., Walker, P. L. & Painter, P. C. FTIR studies of Saran chars. *Carbon.* **21**, 69–74 (1983).
69. Shin, S., Jang, J., Yoon, S. H. & Mochida, I. A study on the effect of heat treatment on functional groups of pitch based activated carbon fiber using FTIR. *Carbon.* **35**, 1739–1743 (1997).
70. Burgio, N., Iasonna, A., Magini, M., Martelli, S. & Padella, F. Mechanical alloying of the Fe-Zr system. Correlation between input energy and end products. *Il Nuovo Cimento D* **13**, 459–476 (1991).
71. Magini, M., Iasonna, A. & Padella, F. Ball milling: An experimental support to the energy transfer evaluated by the collision model. *Scr Mater* **34**, 13–19 (1996).
72. Murty, B. S., Mohan Rao, M. & Ranganathan, S. Milling maps and amorphization during mechanical alloying. *Acta Metallurgica Et Materialia* **43**, 2443–2450 (1995).
73. Liu, X. *et al.* Preparation of polyimide composites reinforced with oxygen doped boron nitride nano-sheet as multifunctional materials. *Mater Des* **180**, (2019).
74. Morimoto, N. *et al.* Real-Time, in Situ Monitoring of the Oxidation of Graphite: Lessons Learned. *Chemistry of Materials* **29**, 2150–2156 (2017).
75. Hummers, W. S. & Offeman, R. E. Preparation of Graphitic Oxide. *J Am Chem Soc* **80**, 1339 (1958).

CHAPTER 5
Vertically grown carbon nanowalls on graphene oxide: synthesis and Li-ion storage application

ABSTRACT

We report herein the synthesis of polyimide (PI) nanowalls on graphene oxide surface by a simple in situ polymerization. The nanowall structures are converted to three-dimensional carbon materials, and their capacity and cycling stability of Li-ion batteries (LIBs) are investigated. The performance of LIBs electrodes relies on the synthesis conditions, such as time and temperature, of the PI nanowall structures; the highest charging capacity reaches 500 mAh g^{-1} at 1C (372 mA g-1) and 152 mAh g^{-1} at 10C charging/discharging cycles. Furthermore, it has excellent stability after 500 cycles of charging and discharging.

I. INTRODUCTION

Li-ion batteries (LIBs) possess the advantage of high energy density, making them the primary power source for electric vehicles, smartphones, and portable electronic devices.[1] With the rapid development of LIB technology, there is a growing demand for high capacity and stability. Although graphite exhibits excellent cycling stability and is used in commercial anode material of LIBs, it shows a low theoretical capacity (372 mAh g^{-1}), slow charge-discharge performance.[2,3] Therefore, it is essential to develop new materials with higher capacity, good rate performance, and higher cycling stability.[4,5] Transition metal oxides have been investigated as the anode electrode materials, such as TiO_2, Fe_2O_3, and MnO_2, for LIBs due to their high-capacity performance (500-1000 mA g^{-1}).[6–9] However, these materials suffer from electrical conductivities, inhibiting high rate performances. Moreover, during the

charge-discharge processes, the volume expansion of the electrodes caused by lithium insertion leads to electrode fracturing and rapid capacity decay.[10–12] To address these issues, nanostructured wire arrays of transition metal oxides have been investigated.[13–15] Nano-structured wires significantly increase the material's specific surface area, facilitating the diffusion of Li-ion into the electrodes and contributing to the improved rate performance of LIBs.[16–19] Moreover, previous studies have shown that nanowall structures exhibit enhanced cycle performance in LIBs, similar to the nanowire structure.[20,21] However, the metal oxides have drawbacks in terms of weight and cost. Recent reports have indicated that the growth of polyaniline nanowires structures contributes to good capacity and cycle stability of LIBs.[22,23] Based on these research backgrounds, we aim to construct the carbon nanostructures on a lightweight and cost-effective two dimensional carbons to address these shortcomings.

In this research, we employ graphene oxide (GO) as a substrate for carbon nanostructures. GO is a mass-producible two-dimensional nanocarbon that contains numerous oxygen functional groups on its surface, allowing chemical modification with organic molecules and dispersion in various solvents.[10,24–29] Previous reports indicate that the composite of transition metal oxide nanowalls and GO enhance the capacities and cycling stabilities of LIBs.[30–34] However, there is no report on the performance of carbon nanowalls/GO composites in anode materials of LIBs. Polyimide (PI) is a promising material for various applications due to its good chemical stability, heat resistance, and good mechanical properties.[35–37] PI carbonizes without melting when heated at >500 °C,[38–40] forming an electron conductive carbon material. In this study, PI nanostructures were fabricated on GO, then nanostructured conductive carbon materials were produced by heat treatment to apply for LIB anodes. The optimum preparation condition of PI/GO composites for LIB electrodes was investigated by changing the reaction time and heating conditions. Finally, we successfully fabricated a nanostructured composite of PI nanowalls on the surface of GO nanosheets, demonstrating a synergistic improvement in the capacity and rate performances of anode material in LIBs.

II. RESULT AND DISCUSSION

II.1 PI-GO nanowall structures (PI-GO) synthesis

GO is highly dispersible in polar organic solvents such as DMAc, DMF, and NMP.[27,29] First, we measured scanning electron microscope (SEM), transmission electron microscope (TEM), and atomic force microscopy (AFM) for pristine GO (Fig. 1), confirming the 2D nanosheet morphology of GO with the thickness of 1 nm, which is consistent with the previous reports.[25–27,29]

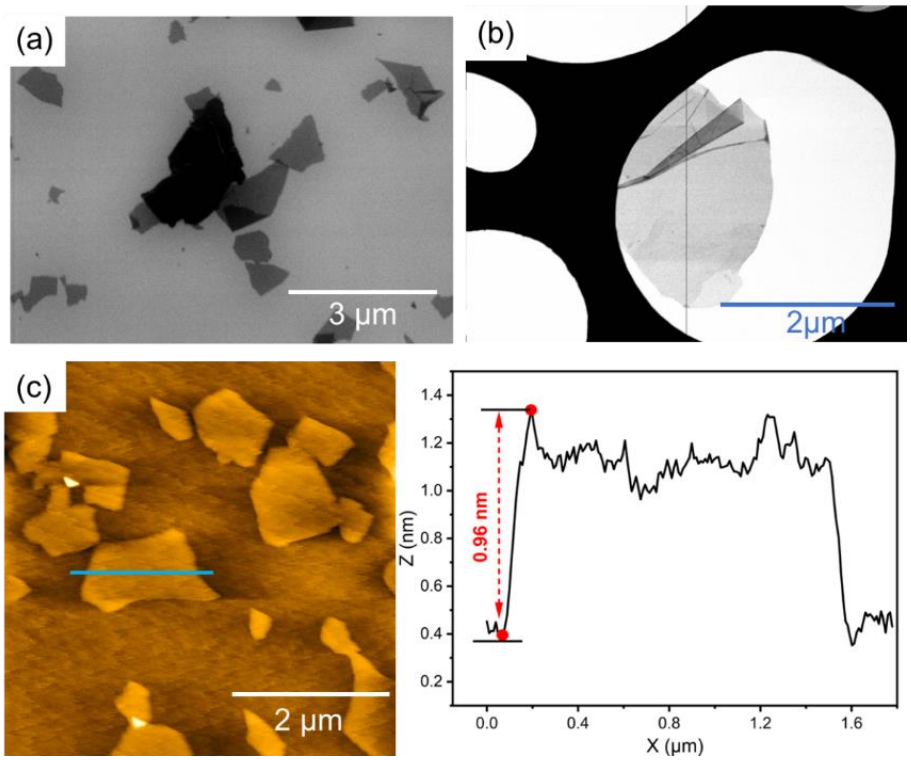

Fig. 1 SEM, TEM, and AFM images of GO sheets (a) SEM images of GO, (b) TEM images of GO, (c) AFM image of GO on SiO_2 and its section analysis.

After chemical reacting GO with p-phenylenediamine (p-PDA) (Fig 2a), the following analyses were conducted: AFM, FTIR, X-ray Diffraction (XRD), and X-ray Photoelectron Spectroscopy (XPS) (Fig 2b-e). Initially, AFM measurements revealed an increase in the thickness of GO-PDA to 1.89 nm (Fig 2b), which is nearly equivalent to the molecule thickness of p-PDA.[41] In FTIR (Fig 2c), the presence of C-N and N-H bonds was observed at 1287 cm^{-1} and 1510 cm^{-1}, respectively,[42] indicating the chemical modification of GO with p-PDA. XRD analysis (Fig 2d) showed that the peak of chemically

modified GO (002) shifted from 11.7° to 7.5°, and the Full Width at Half Maximum (FWHM) increased from 1.03 to 2.07, demonstrating the incorporation of p-PDA within GO.[43] In XPS (Fig 2e), the nitrogen peak was clearly observed after reaction with p-PDA, confirming the successful modification of the GO surface with p-PDA. [43]

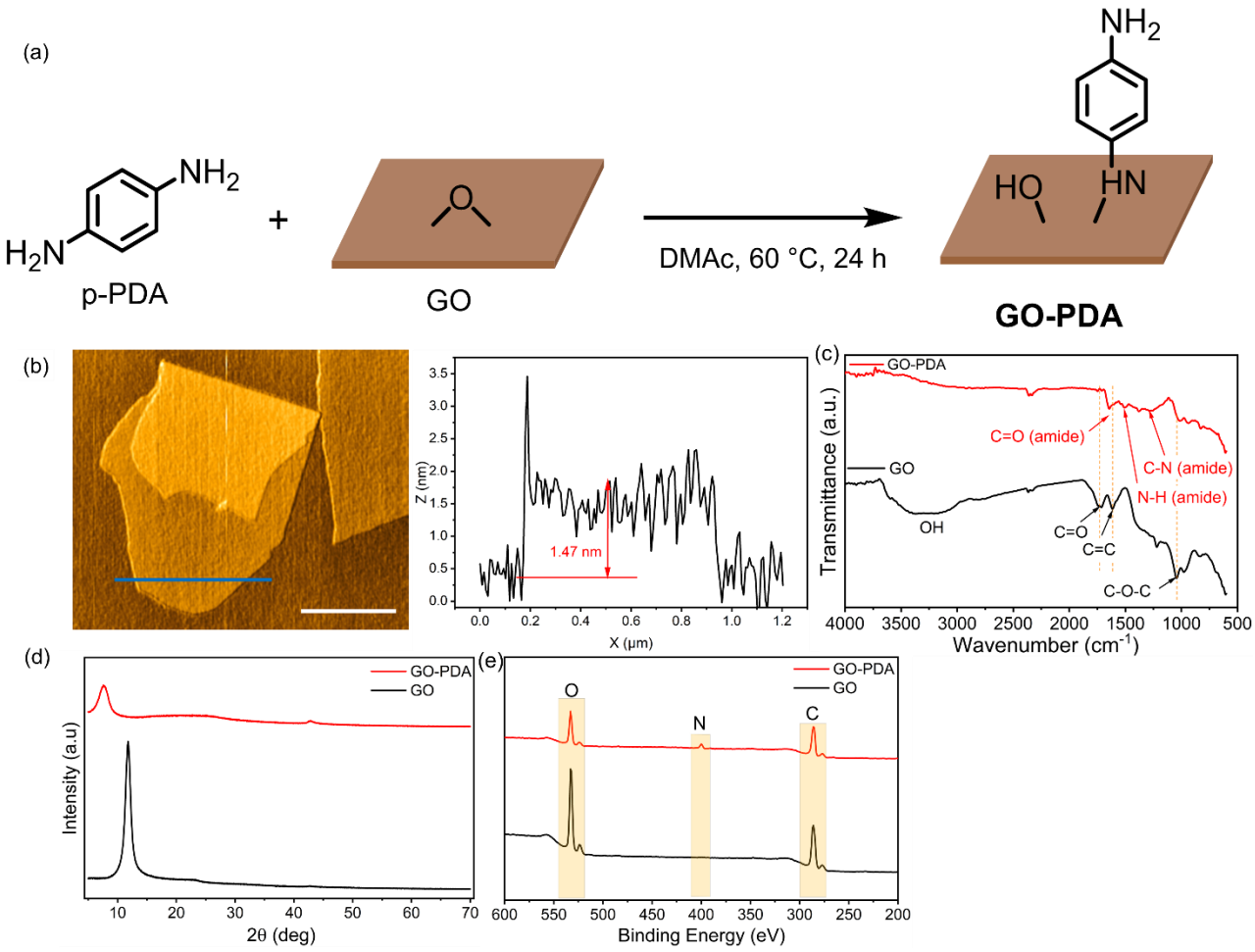

Fig. 2 (a)Schematic illustration of the formation mechanism of GO-PDA, (b) AFM images of GO-PDA, (c) FTIR analysis of GO and GO-PDA, (d) XRD analysis of GO and GO-PDA, (e) XPS analysis of GO and GO-PDA.

Next, Polyimide nanowall structures (**PI**) were synthesized by *in-situ* polymerization on GO-PDA. GO was homogeneously dispersed in different polyamic acid (PAA) solutions. In this process, we used four different types of molecules p-PDA, 4,4´-diaminodiphenyl ether (ODA), 3,3´,4,4´-Benzophenonetetracarboxylic dianhydride (BTDA), and 4,4'-Biphthalic Anhydride (BPDA). We mixed these in four different ways, forming p-PDA/BTDA, PDA/BPDA ODA/BTDA, and

ODA/BPDA. Then, the mixtures were heated in an autoclave at 180 °C. As a result, only the p-PDA/BTDA mixture successfully produced the PI nanowall structures no GO (**PI-GO**) (Fig. 3a), whereas the other combinations had smooth surfaces (Fig. 3b-d). Thus, in this study, we used p-PDA and BTDA to create the **PI**.

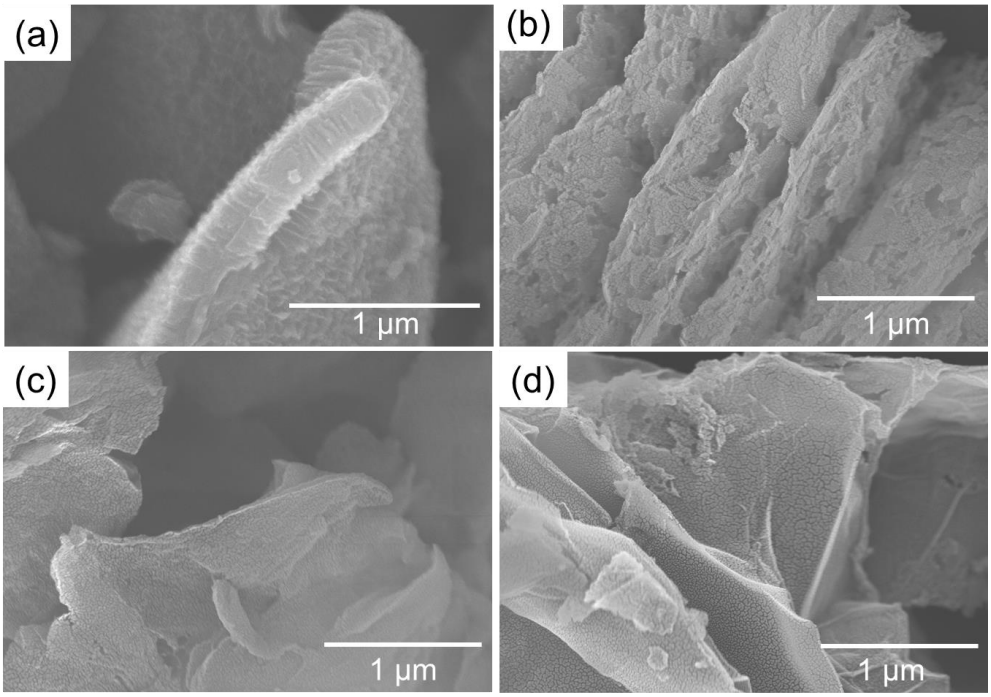

Fig. 3 SEM images of PI-GO prepare by different type of PAA (a) p-PDA/BTDA, (b) ODA/BPDA, (c) p-PDA/BPDA, (d) ODA/BTDA. For all samples, Au ion sputtering was carried out before SEM measurements.

After experimenting with different amounts of GO. We found that morphology of the **PI-GO** was affected by the amount of GO, as shown in Fig. 3. In the case of 0.5 wt%-GO, **PI-GO** combined with polyimide (**PI**) was formed, suggesting that the excess PAA became **PI** outside GO (Fig. 4a). When the concentration of GO was increased to 1 wt%, **PI** selectively arrayed on GO surface and no **PI** was observed (Fig. 4b). However, when the concentration of GO increased to 2 wt%, nano structure was not observed, indicating that the **PI** did not grow on GO surface because PI could only cover the GO surface (Fig. 4c). Therefore, the optimal concentration of GO was determined to be 1 wt%.

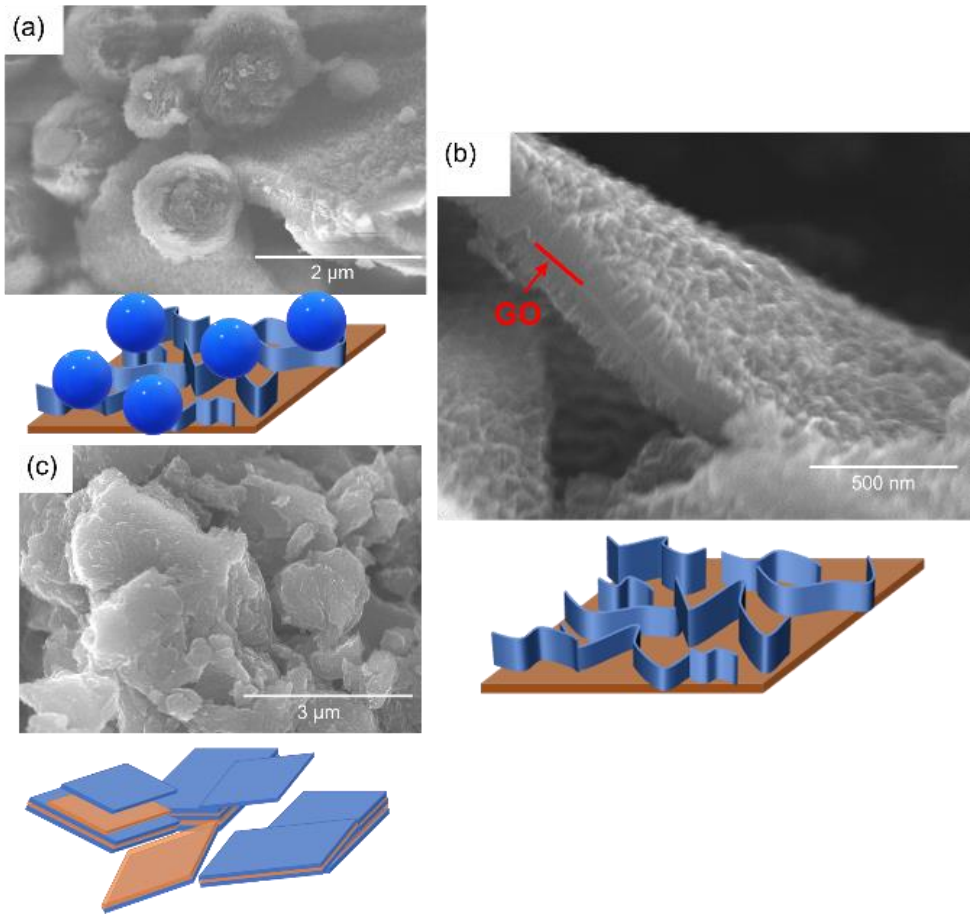

Fig. 4 SEM images of **PI-GO** samples obtained at different concentrations: (a) 0.5 wt%, (b) 1 wt%, and (c) 2 wt%.

To further investigate the formation process of PI nanowalls on GO, **PI-GO** samples were taken out at different reaction times during the imidization process. As shown in Fig. 5a, after 1h of reaction (**PI-GO 1h**), the surface of GO began to be slightly rough, but no nanowall structures was observed. When the reaction time increased to 3 h (**PI-GO 3 h**), many PI nanowall structures grew clearly on the surface of GO (Fig. 5b). After increasing the reaction time to 5 h (**PI-GO 5h**), the morphologies did not significantly change (Fig. 5c and d).

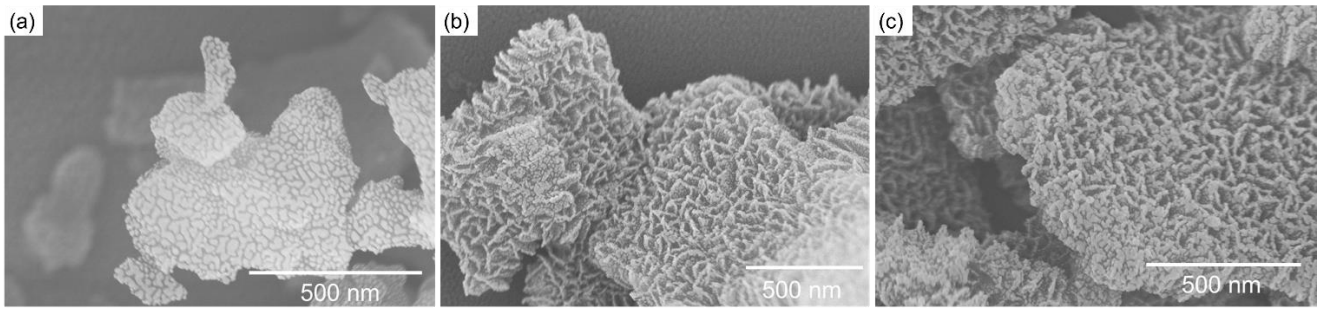

Fig. 5 SEM images of **PI-GO** samples obtained at different reaction times: (a) 1h, (b) 3 h, and (c) 5 h. For all samples, Au ion sputtering was carried out before SEM measurements.

Based on the above experimental results, we illustrate the formation process of PI-GO nanocomposites (Fig. 6). When GO-PDA is added to the PAA solution, the surface of GO-PDA is coated with PAA via covalent bond formation between epoxide and amine groups on GO-PDA and the terminal amino groups on PAA, and/or via the π–π interactions between aromatic domains of GO-PDA and PAA.[44,45] Under autoclave treatment, PI nanowalls slowly grow on the surface of GO-PDA (Fig. 6).

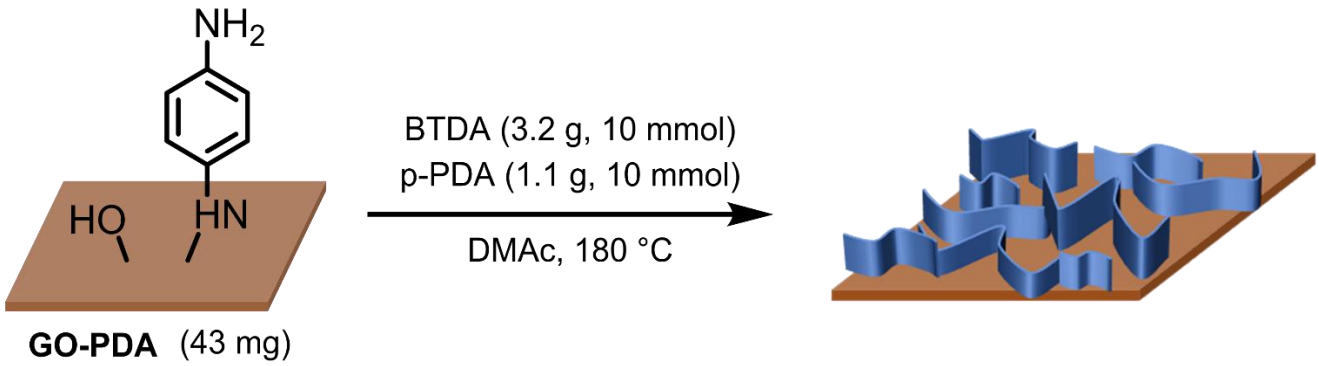

Fig. 6 Schematic illustration of the formation mechanism of **PI-GO**.

II.2 Structural Characterization of PI-GO

The **PI** and **PI-GO** are characterized by FT-IR, as shown in Fig. 6a. First, a PAA film prepared by drying PAA solution was measured (Fig. 6(i)); the peak of C=O (amide group) was observed at 1605 cm^{-1}. The C=O (imide groups) of **PI** (Fig. 6(ii)) were observed at 1778 and 1716 cm^{-1}, proving the formation of PI structure through the autoclave treatment.[46,47] We carried out the shorter autoclave treatment of 1h, 3 h and 5 h (**PI-GO 1h, PI-GO 3h** and **PI-**

GO 5h), to elucidate the initial state. For the reaction time of 1h, the C=O flexions (amide and imide groups) were observed at 1605, 1778, and 1716 cm^{-1} (Fig. 7(iii)). It had been demonstrated that a reaction time of 1h was inadequate to complete imidization of PAA to PI. Furthmore, the remaining FTIR spectra showed similar patterns, indicating that the molecular structure of the PI generated under different reaction times are identical (Fig. 7(iii)-(v)).

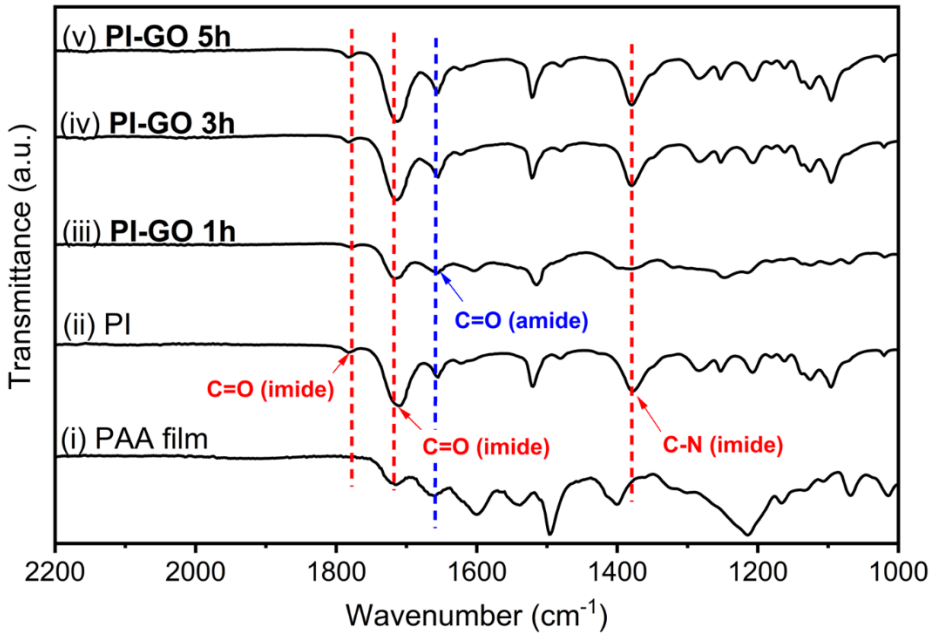

Fig. 7 FT-IR spectra of (a) PAA film, **PI**, and **PI-GO** prepared under different reaction times.

To further confirm the structure of **PI-GO**, XRD was employed, as shown in Fig. 8. No peak for GO was observed for **PI-GO**, indicating that the grown PI nanowalls on the surface of GO prevent GO from being stacked. Six peaks at 2θ = 10.1°, 15.4°, 18.8°, 22.5°, 27.4° and 28.4° for **PI-GO** are identical to the peaks of **PI** (Fig. 8(i)-(iv)).[48,49] Therefore, both PI have the same molecular structure. Furthermore, the broadness of peaks for all **PI-GO** samples remains unchanged, suggesting the crystallinity of PI did not change over time.

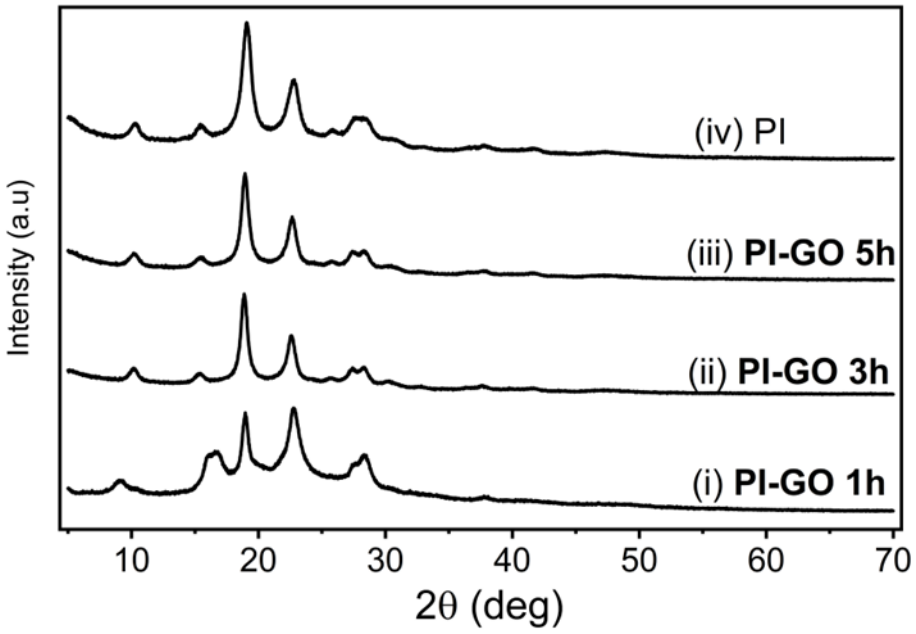

Fig. 8 XRD patterns of **PI** and **PI-GO**

Next, we heated **PI-GO** at 500 °C and 900 °C for 1h under a nitrogen atmosphere to increase the electric conductivity. Hereafter, the **PI-GO** heated at 500 °C and 900 °C are referred to as **PI-GO 500**, and **PI-GO 900**, respectively. After heating at 500 °C for 1h, the imide groups were still observed at around 1778 and 1716 cm^{-1}, and the C-N stretch peak (1376 cm^{-1}) became wider and weaker (Fig. 9iii and Fig. 7v), indicating that only a part of **PI-GO** was carbonized after heating at 500 °C.[38–40]

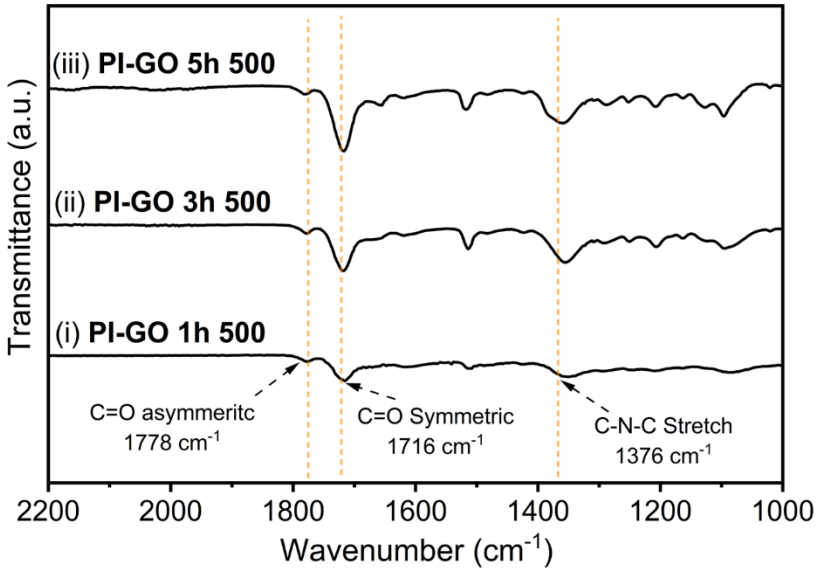

Fig. 9 FT-IR spectra of different reaction of **PI-GO 500**

According to the TGA (Fig. 10), the weight of **PI-GO** drops sharply after 500 °C-550 °C, at which the PI nanowalls start to carbonize. This proves that the complete carbonization of PI was not achieved at 500 °C. XRD also confirmed the partial carbonization of PI after heating at 500 °C; similar peaks with **PI-GO** were observed (Fig. 11a(i-iii)).

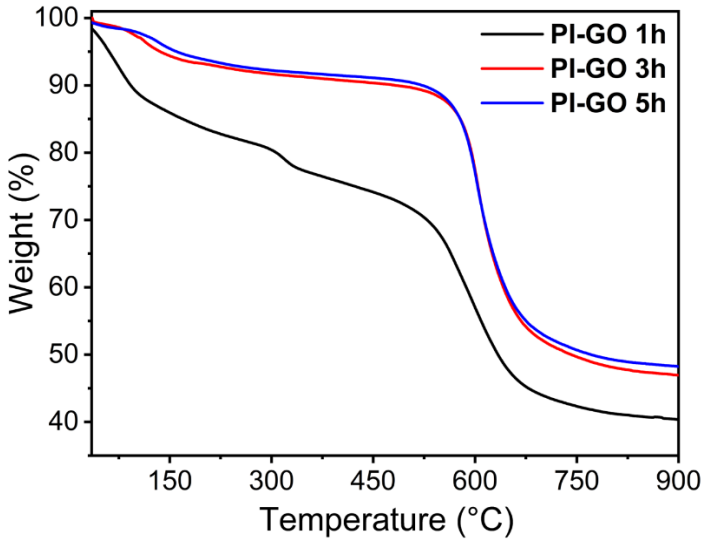

Fig. 10 TGA curves of different reaction times of **PI-GO**.

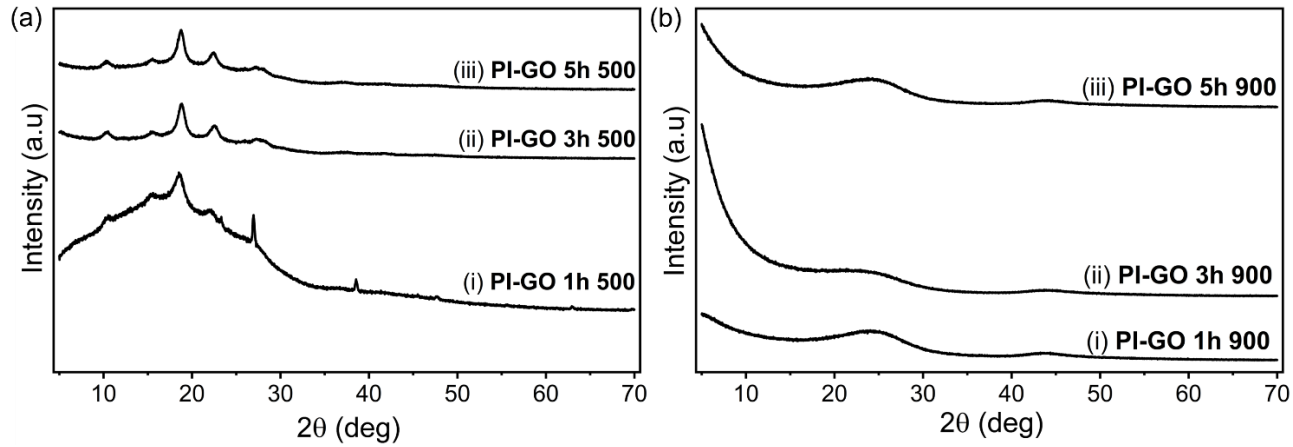

Fig. 11 XRD patterns of (a) **PI-GO 500**, (b) and **PI-GO 900**.

When the heating temperature was increased to 900 °C, the **PI-GO** was converted to amorphous material, as shown in Fig. 11b(i-iii).[50,51]

However, SEM images (Fig. 12a, b, and c) show that the nanowall structures was not destroyed after 900 °C treatment. The degree of carbonization was confirmed by Raman spectroscopy and XPS.

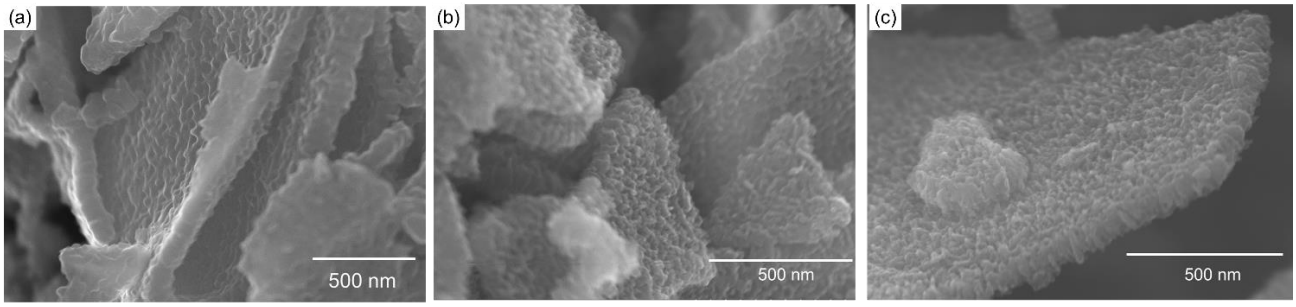

Fig. 12 SEM images a of **PI-GO 900** samples: (a) **PI-GO 1h 900**, (b) **PI-GO 3 h 900**, and (c) **PI-GO 5h 900**.

In Raman spectroscopy (Fig. 13), the G band and D band can be clearly observed; all the samples show I_D/I_G (where I_D and I_G are the D-band and G-band Raman intensities) values close to 1.0 (Fig. 13(i)-(iii)), thus all the products have similar defective structures.[52,53] According to XPS analysis (Fig. 14), the sp^2 carbon, sp^3 carbon, C=O, and π–π∗ transition peaks were observed, whereas the N 1s peak was not present,[54,55] suggesting PI was converted to amorphous carbon after 900 °C treatment.

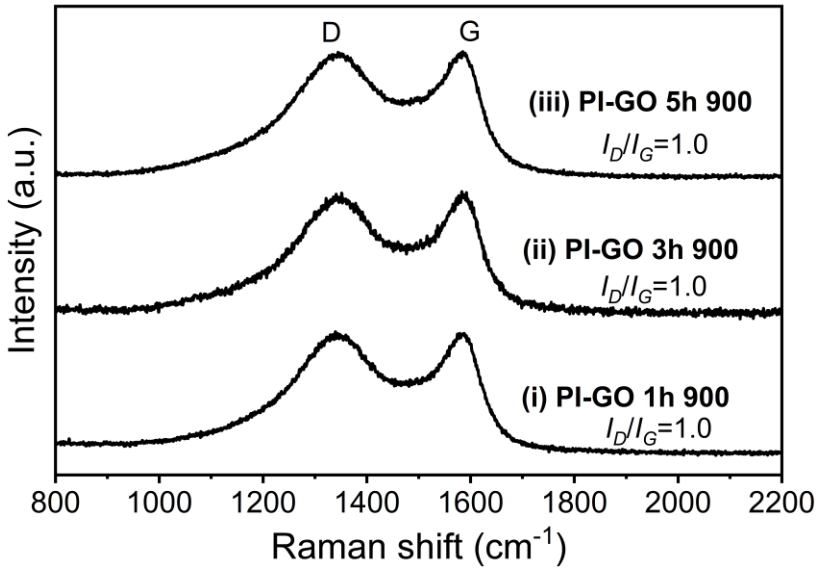

Fig. 13 Raman spectra of **PI-GO 900** samples. All spectra were normalized to the G-band intensity.

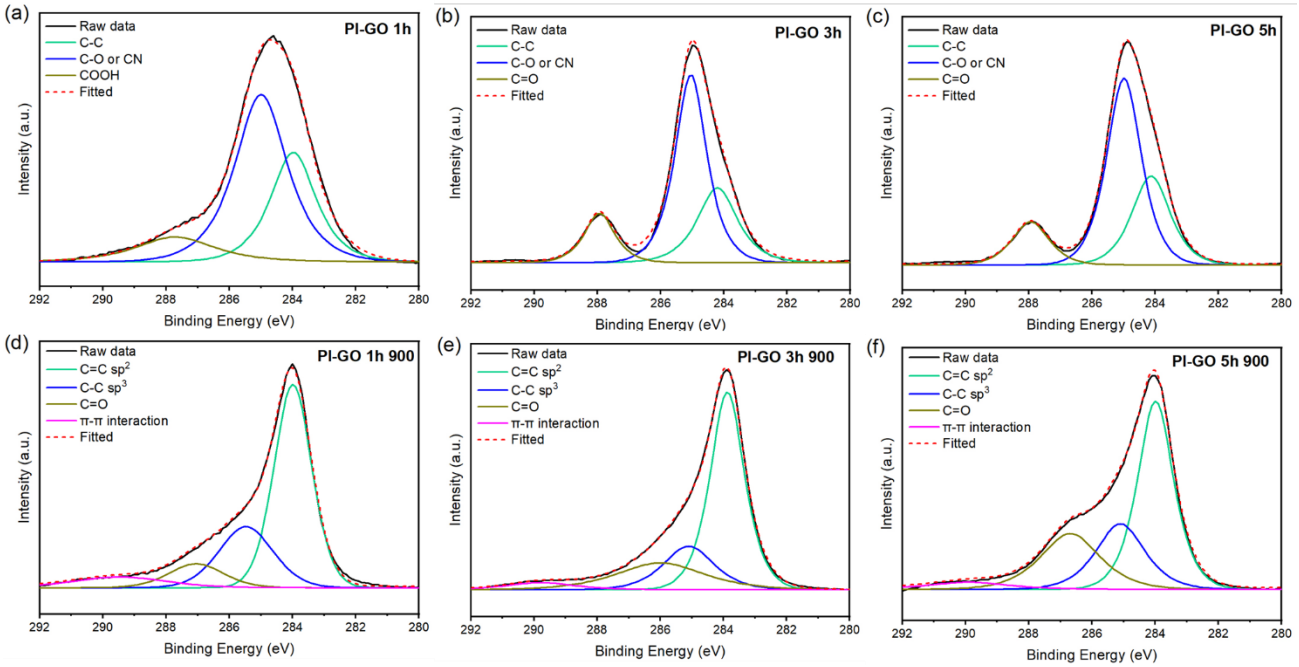

Fig. 14 XPS analysis of **PI-GO** and **PI-GO 900** (a) **PI-GO 1h**, (b) **PI-GO 3 h**, (c) **PI-GO 5h**, (d) **PI-GO 1h 900**, (d) **PI-GO 3 h 900**, (d) **PI-GO 5h 900**.

II.3 Li-ion battery performance

We successfully prepared PI nanoarray structures on GO. Next, we fabricated LIBs using them. **PI**, and **PI-GO** samples were designed as active materials in the anode electrode in LIBs. After assembling the coin cells, LIBs performances were evaluated based on capacity as a function of charging rate at 1 C (372 mA g^{-1}), 2 C, 5 C, 10 C, 20 C, 50 C, 100 C, and 1 C (with 5 cycles each, total 40 cycles). First, we examined the performance of the batteries that used graphite, GO, and **PI** as the active material in the anode electrodes. At a charge rate of 1 C, the capacity of the battery using **PI** reached 567 mAh g^{-1} at the first cycle, which is approximately triple of GO and double of graphite); however, the capacity performance of **PI** suddenly decreased to the same level of graphite (Table. 1 Entry 1-3, and Fig. 15a). This means that **PI** is unstable under charging and discharging conditions. According to previous literature, the nanowall structures improved capacity performance and stability.[20,21] Hence, we measured LIB performance for **PI-GO** to elucidate the effect of nanowalls. In order to understand the

performance correlation between reaction time and LIBs, we prepared a comparison between **PI-GO** and **PI** for 3h, and 5h, respectively. According to Entry 3-6 in Table 1, the best performance of **PI-GO** was achieved at a reaction time of 5 h in the un-sintered condition. At a charge rate of 372 mA g^{-1} (1 C), the capacity reached 393 mAh g^{-1} (Table. 1 Entry 3 and 5) even after 40 cycles, which was 29% higher than that using **PI**. The Coulombic efficiency was maintained at 96 % after 40 charging and discharging cycles (Fig. 15b).

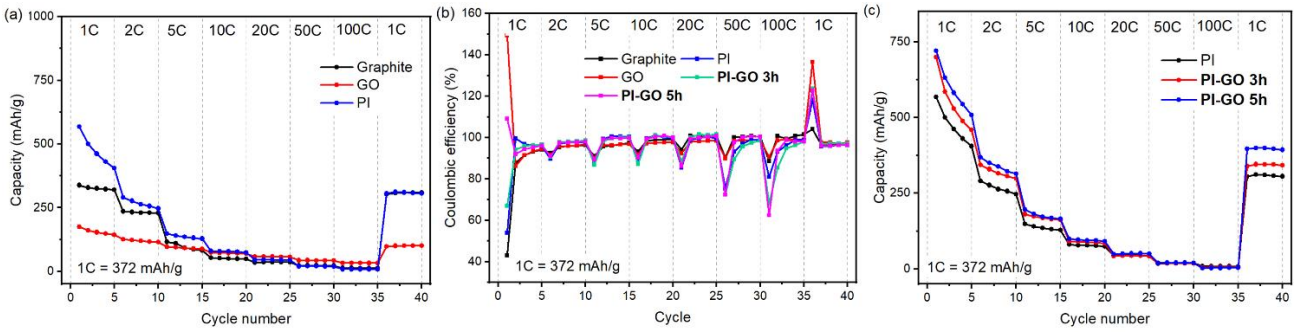

Fig. 15 (a) LIBs capacity performance at different current rate (1C = 372 mA g^{-1}): Graphite, GO, **PI**, (b) Different polyimide synthesis time of **PI-GO**. Coulombic efficiency curve of Graphite, GO and **PI-GO** in different charge-discharge current rates (1C = 372 mA g^{-1}). (c) LIBs capacity performance PI, and **PI-GO**.

According to the BET surface area (Entry 4 and 5 in Table. 1), **PI-GO 5h** showed the largest specific surface area. Therefore, nanoarray structure on GO is preferrable for LIBs and reaction time affects the performance. Although after 40 cycles performance is better than that of graphite, the capacity rapidly decreased in the first 5 discharge cycles, which is the same phenomenon as the batteries using only **PI** (Fig. 15c).

Both need to be charged and discharged several times before they can be stabilized. Due to the nanowall structures, the Li-ions can migrate into the interior more effectively, which is why the capacity performance is greater than that of **PI**. (Fig. 16).

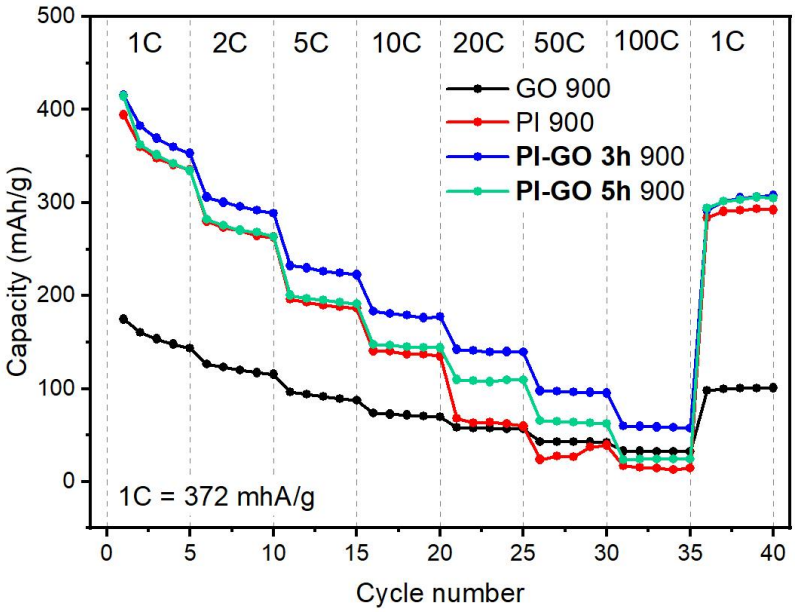

Fig. 16 LIBs capacity performance at different current rate (1C = 372 mA g^{-1}): **GO 900**, **PI 900**, **PI-GO 3 h 900**, **PI-GO 5h 900**.

Therefore, the above results demonstrate that PI nanowalls are more effective in allowing Li-ions to move within the material, which in turn improves the capacity and stability of LIBs.

Table 1. LIBs capacity performance of active material.[1]

Entry	Sample	Capacity (mAh g^{-1})		Specific surface area (m^2 g^{-1})[2]
		@ 1C	@ 10C	
1	GO	101	58	-[3]
2	Graphite	308	48	-[3]
3	**PI**	305	74	76
4	**PI-GO 3 h**	341	97	191
5	**PI-GO 5h**	393	91	215
6	**GO 900**	89	70	-[3]
7	**PI 900**	292	74	379
8	**PI-GO 3 h 900**	307	177	732
9	**PI-GO 5h 900**	305	152	431

[1] Capacities were evaluated by assembling, CR2032 coin cell (see, experimental section). 1C= 372 mA/g.

[2] Specific surface area was measured by BET method in arelative pressure range of 0.05–0.30 for comparison.

[3]-: Unmeasurable.

To investigate the effect of electrical conductivity on LIBs performance, we measured LIB's performance using **PI-GO** sintered at 900 °C. **PI-GO 5h 900** has the best capacity performance (Entry 8 and 9 in Table. 1). The capacity reached 305 mAh g^{-1}, which is 4 % and 242 % higher than **PI** and GO sintered at 900 °C (**PI 900** and **GO 900**), respectively. This proves that sintering at 900 °C at which slight carbonization occurred, enhance the capacity performance of LIBs. In recent years, with the rapid development of electronic products, the demand for fast charging has become increasingly prominent. Interestingly, at a high current of 10 C charge-discharge, **PI-GO 5h 900** achieved a capacity of 155 mAh g^{-1} (Fig. 16). This indicates that **PI** can effectively accommodate and release Li-ions to maintain capacity. Compared with **PI-GO 900**, **PI-GO** showed only 91 mAh g^{-1}(in 10 C), although **PI-GO 900** has a very large specific surface area and small pore (Entry 7 to 9 in Table). The capacity is reduced despite the high degree of the carbonization of PI nanowalls on the GO surface. These results indicate that incorporating a small amount of nitrogen element in the active material effectively enhance the capacity performance of lithium batteries [56,57]

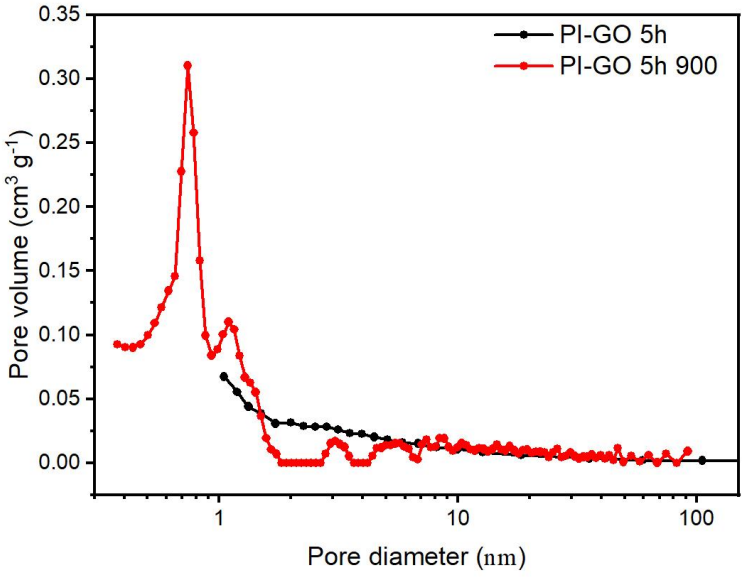

Fig. 17 The pore size distributions of **PI-GO 5h**, and **PI-GO 5h 900**. The **PI-GO** was analyzed using Barrett-Joyner-Halenda model. The **PI-GO 5h 900** was analyzed using Non-localized density functional theory model.

PI-GO 900 has nitrogen atoms originated from PI structure, which was 2.8% (Fig. 18). This value, 305 mAh g^{-1}, is 4% and 241% higher compared to **PI** and GO sintered at 900 °C (**PI 900** and **GO 900**), which is further evidence that the nanowall structures can be more effective in allowing Li-ions to move internally even after strong carbonization.

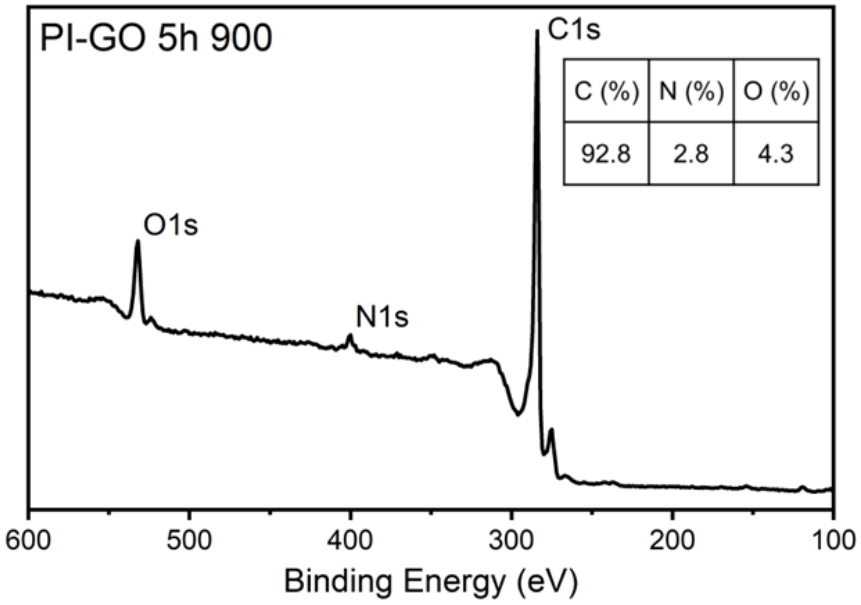

Fig. 18 XPS analysis of **PI-GO 5h 900**.

Finally, we tested the stability of the material by performing 500 cycles of high current 10 C charge and discharge. As shown in Table 2, the capacity of **PI** and **PI-GO** can be maintained at 63 mAh g^{-1} and 72 mAh g^{-1}, which are 30% and 49% higher than that of graphite under high current conditions, respectively (Table 2 Entry 1 and 2). These show that the **PI** and **PI** stabilized the internal movement of Li-ions even under high currents. The capacity of **PI 900** and **PI-GO 900** were maintained at 74 mAh g^{-1} and 171 mAh g^{-1} (Table 2, Entry 3 and 4). The capacity of **PI-GO 900** is larger than that of **PI 900** due to the nanowall structures, which allows the Li-ions to move around more easily under high currents. Moreover, the Coulombic efficiency was maintained around 100% (Table 2 Entry 4). These results showed **PI-GO** remains stable under high currents and has great potential for future applications in fast charging devices.

Table 2. LIBs capacity performance and Coulombic efficiency of **PI**, **PI-GO**, **PI-900**, and **PI-GO 5h 900** after 500 cycles.[1]

Entry	Sample	Capacity (mAh g^{-1})	Coulombic efficiency (%)
1	PI	63	100
2	PI-GO 5h	72	100
3	PI 900	74	94
4	PI-GO 5h 900	171	100

[1] Capacities were evaluated by assembling, CR2032 coin cell (see, experimental section) at 10 C = 3.72 A g^{-1}.

III. CONCLUSIONS

In summary, the PI nanowall structures (**PI**) were successfully and finely aligned on GO nanosheets by *in situ* polymerization, and the **PI** was not destroyed after 900 °C treatment. The shape of the **PI** could be adjusted by adjusting the reaction time in the autoclave due to the different generation processes. The best capacity performance of the Li-ion battery was achieved when the reaction time was 5 h and the sintering temperature was 900 °C (**PI-GO 5h 900**). A charge rate of 372 mA g^{-1} (1 C) was achieved at 305 mAh g^{-1} (4% and 242% higher than **PI** and GO, respectively) and 152 mA g^{-1} at high current (10 C). This is attributed to the **PI** and the small amount of N atoms in PI. After charged and discharged at high currents for 500 cycles, there was excellent capacity performance and stability. This is attributable to the **PI**.

In this research, we introduce the simple process nanowall composite materials and application mechanism, which can be used as a guide for designing new composite materials and energy storage components at the nano-node scale.

IV. EXPERIMENTAL SECTION

IV.1 Materials

4,4'-Biphthalic anhydride (BPDA, purity 98.0+%), 4,4'-diaminodiphenyl ether (ODA, purity 99.0+%), p-phenylenediamine (p-PDA, purity 97.0+%), 3,3',4,4'-benzophenonetetracarboxylic dianhydride (BTDA, purity 96.0+%), dimethylacetamide (DMAc, purity 98.0+%), sulfuric acid (H_2SO_4, purity 95.0+%), and potassium permanganate ($KMnO_4$, purity 99.3+%) were purchased from FUJIFILM Wako Pure Chemical Corporation, Osaka, Japan. Graphene oxide (GO) was prepared according to Hummers' method with a slight modification.[58,59]

IV.2 Characterization instruments

Fourier transform infrared spectroscopy (FT-IR) spectra of the samples were recorded on a IRTracer-100 (Shimadzu, Japan) in the wavenumber range of 400 to 4000 cm^{-1}. X-ray diffraction (XRD) measurements were performed on AERIS equipped with single crystalline silicon (Panalytical, Netherlands). X-ray photoelectron spectroscopy (XPS) was carried out on a JPS-9030 (JEOL, Japan) with a pass energy of 20 eV. The scanning electron microscope (SEM) and scanning transmission electron microscopy (STEM) measurement were performed with SU9000 (Hitachi Limited, Japan) with an accelerating voltage of 10-30 kV. Thermal gravimetric analyses (TGA) were measured from room temperature to 900 °C at a heating rate of 10 °C min^{-1} under nitrogen (N_2) on a DTG-60AH (Shimadzu, Japan). Raman spectroscopy was measured using an NRS-3100 (JASCO Corporation, Japan) with a 532 nm laser and confocal lens. BET surface areas a were measured using a BELSORP MAX II surface area (Microtrac MRB, USA). The **PI-GO**, **PI-GO 500** pore size distribution (PSD) curves were analyzed using Barrett-Joyner-Halenda model. However, the PSD was computed by the Non-localized density functional theory model,[60,61] because **PI-GO 900** has many mesoporous from the N_2 adsorption/desorption isotherm of **PI-GO** (Fig. 19a-c).

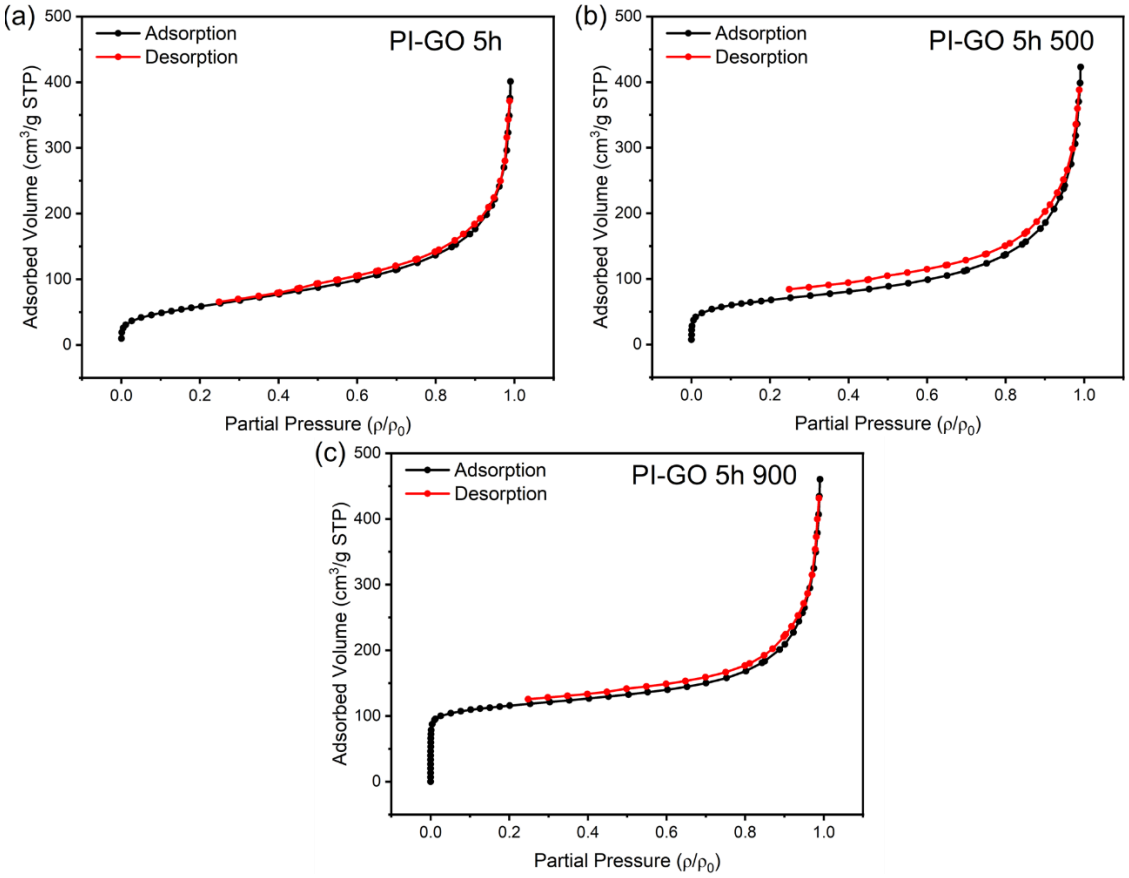

Fig. 19 N_2 adsorption/desorption isotherms of **PI-GO 5h** (a) **PI-GO 5h**, (b) **PI-GO 5h 500**, (c) **PI-GO 5h 900**.

IV.3 Preparation of polyimide

p-PDA (1.08g, 10mmol) was dispersed in DMAc (20 mL) by sonication for 10 min (on ice bath). Then, BTDA (3.2 g, 10 mmol) was added to the solution. Then, it was sonicated for 10 min, and kept at -20 °C as a stock suspension of polyamidic acid (PAA).

The polyimide (PI) samples were synthesized in a polyvinylidene difluoride (PVDF) container by heating at 180 °C for 12 h in an autoclave. After cooling down to room temperature, the precipitates were collected by centrifugation and washed with ethanol and deionized (DI) water 3 times to remove remaining DMAc. Finally, the yellow-colored PI powder was obtained after vacuum drying overnight at 50 °C.[48,62] From the SEM image, it can be observed that the spherical shape and the surface is very wrinkled (Fig. 20a). Furthermore, the structure was not damaged after ball milling for 10min 2000rpm in ethanol (Fig. 20b).

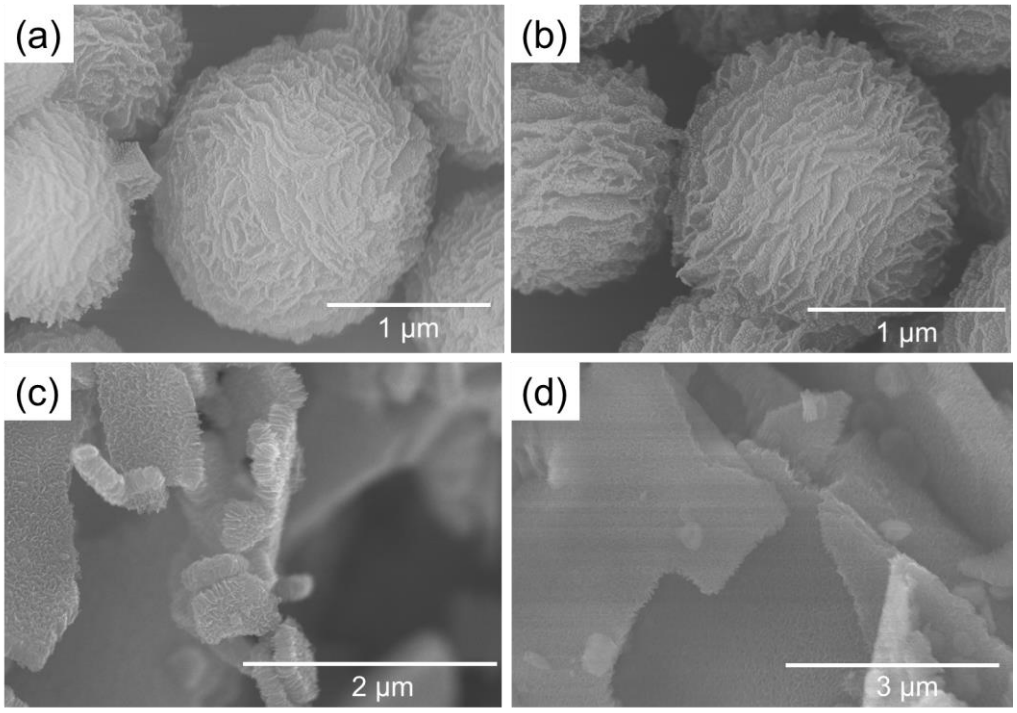

Fig. 20 SEM images of **PI** and **PI-GO** (a) **PI**, (b) **PI** after ball milling, (c) **PI-GO**, and (d) **PI-GO** after ball milling.

IV.4 Preparation of PI carbon material

The synthesized **PI** powder was heated at 300 °C for 1h (room temperature to 300 °C for 2 h) and then the temperature increased 5 °C/min to a temperature of 500 °C or 900 °C for 1h under nitrogen. The produced powders were called **PI 500** and **PI 900**, respectively.

IV.5 Preparation of PI nanowall structures on GO (PI-GO)

p-PDA (1.08 g, 10 mmol) was dispersed in DMAc (20 mL) by sonication for 10 min (in ice bath). Then, BTDA (3.2 g, 10 mmol) was added to the solution. The mixed suspension was sonicated for 10 min. After that, we obtained a homogeneously dispersed PAA solution. Afterwards, 1 wt% of GO was added to the dispersion and sonicated for 10 min, and kept at -20 °C as a stock solution of PAA-GO.

The **PI-GO** was prepared in a polyvinylidene difluoride (PVDF) container, which was located inside an autoclave at 180 °C for 3 h, 5 h and 12 h. After cooling down to room temperature, the precipitates were collected by centrifugation and washed with ethanol and deionized (DI) water 3 times for each solution to remove any remaining DMAc. Finally, the brown colored **PI-GO** powder was obtained

after vacuum drying the material overnight at 50 °C. From the SEM image, it can be observed that the structure was not damaged after ball milling for 10min 2000rpm in ethanol (Fig. 20c-d).

Hereafter, we will call the yielded **PI-GO** as **PI-GO xh** where **x** indicates the duration time of the treatment, respectively.

IV.6 Preparation of Carbonization of PI nanowalls array structures

The carbonization of **PI-GO** was produced by heating **PI-GO** at 300 °C for 1 h (room temperature to 300 °C for 2 h) and then the temperature increased at a ratio of 5 °C/min until temperatures of 500 °C or 900 °C were reached and were kept for 1 h under nitrogen, which was defined as **PI-GO 500**, and **PI-GO 900**, respectively. According to the XPS analysis (Fig 21), the PI on the surface of PI-GO 500 is not completely carbonized. carbonized.

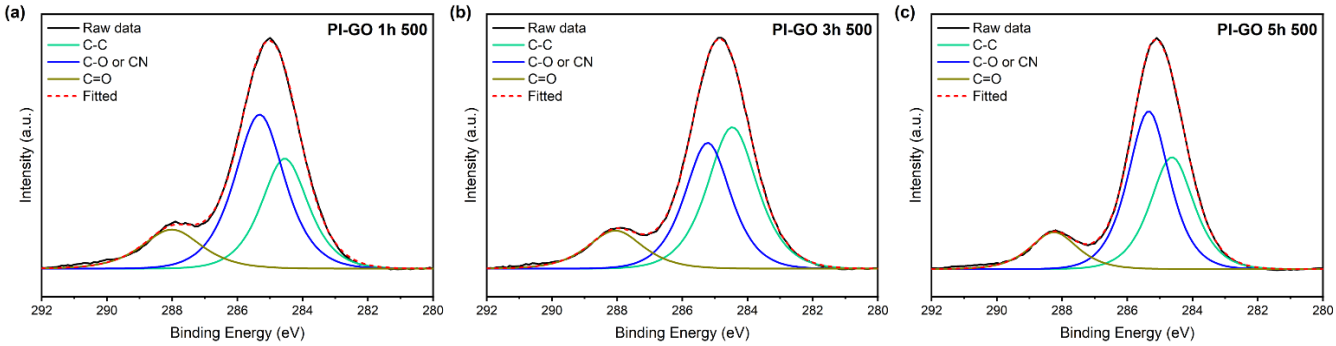

Fig. 21 XPS analysis of **PI-GO 500** (a) **PI-GO 1h 500**, (b) **PI-GO 3h 500**, (c) **PI-GO 5h 500**.

IV.7 Li-ion battery anode sheets preparation

The working electrodes consist of an active material (Graphite, GO, **PI**, **PI-GO**), the conductive material (Acetylene black), and the binder (Polyvinylidene fluoride) in a weight ratio of 7:2:1 by using N-Methyl-2-pyrrolidone (NMP) as a solvent and a copper foil as the current collector. The active material was at first mixed with conductive material and NMP and ball milling for 10 min at 2000 RPM to obtain a homogeneous mud and then added the binder to the mud mixture. The newly synthesized mud (active material, conductive material, binder) was spread on a copper foil by using a doctor blade (100 µm thickness). The sheet was dried under vacuum at room temperature for 1-2 days

and after, it was warmed at 120 °C for 30 min. Finally, the sheets were roll pressed and punched in a diameter of 15.95 mm.

IV.8 Coin cells assembling

The CR2032 coin cells were assembled in an argon-filled glove box using metallic lithium as the counter electrode with a diameter of 17.65 mm, Whatman 1823-257 as a separator and 100 µL of electrolyte. The electrolyte consisted in 1 ML^{-1} $LiPF_6$ dissolved in a mixture of ethylene carbonate (EC) and diethyl carbonate (DEC) (v/v, 3/7).[63]

IV.9 Battery cycling

The charge and discharge cycling tests were performed using a battery tester (580 Battery Cycler Scribner Associates Incorporated) with a voltage window of 0.01 V and 3 V. Each cell was subjected to discharge-charge cycles at different current rates (each rate for 5 cycles, total 40 cycles): 1 C, 2 C, 5 C, 10 C, 20 C, 50 C, 100 C, and 1C for stability.[63] All currents were calculated using 372 mA g^{-1} as a theoretical specific capacity (the ideal capacity of graphite).

REFERENCES

1. Li, M., Lu, J., Chen, Z. & Amine, K. 30 Years of Lithium-Ion Batteries. *Advanced Materials* **30**, 1800561 (2018).
2. Su, X. *et al.* Silicon-Based Nanomaterials for Lithium-Ion Batteries: A Review. *Adv Energy Mater* **4**, 1300882 (2014).
3. Bruce, P. G., Scrosati, B. & Tarascon, J.-M. Nanomaterials for Rechargeable Lithium Batteries. *Angewandte Chemie International Edition* **47**, 2930–2946 (2008).
4. Kim, H. & Cho, J. Superior Lithium Electroactive Mesoporous Si@Carbon Core−Shell Nanowires for Lithium Battery Anode Material. *Nano Lett* **8**, 3688–3691 (2008).
5. Wu, H. *et al.* Stable cycling of double-walled silicon nanotube battery anodes through solid-electrolyte interphase control. *Nat. Nanotech*, **7**, 310–315, (2012).
6. Poizot, P., Laruelle, S., Grugeon, S., Dupont, L. & Tarascon, J. Nano-sized transition-metaloxidesas. *Nature* vol. 407 496 Preprint at (2000).
7. Zhao, Y. *et al.* Recent Developments and Understanding of Novel Mixed Transition-Metal Oxides as Anodes in Lithium Ion Batteries. *Adv Energy Mater* **6**, 1502175 (2016).
8. Liu, Q. *et al.* Recent Progress of Layered Transition Metal Oxide Cathodes for Sodium-Ion Batteries. *Small* **15**, 1805381 (2019).
9. Li, Q. *et al.* Extra storage capacity in transition metal oxide lithium-ion batteries revealed by in situ magnetometry. *Nat Mater* **20**, 76–83 (2021).
10. Compton, O. C. & Nguyen, S. T. Graphene Oxide, Highly Reduced Graphene Oxide, and Graphene: Versatile Building Blocks for Carbon-Based Materials. *Small* **6**, 711–723 (2010).
11. Xu, J., Wang, K., Zu, S.-Z., Han, B.-H. & Wei, Z. Hierarchical Nanocomposites of Polyaniline Nanowire Arrays on Graphene Oxide Sheets with Synergistic Effect for Energy Storage. *ACS Nano* **4**, 5019–5026 (2010).
12. Alf, M. E. *et al.* Chemical vapor deposition of conformal, functional, and responsive polymer films. *Advanced Materials* **22**, 1993–2027 (2010).
13. Thangala, J. *et al.* Large-Scale, Hot-Filament-Assisted Synthesis of Tungsten Oxide and Related Transition Metal Oxide Nanowires. *Small* **3**, 890–896 (2007).
14. Jiao, F., Shaju, K. M. & Bruce, P. G. Synthesis of Nanowire and Mesoporous Low-Temperature LiCoO2 by a Post-Templating Reaction. *Angewandte Chemie* **117**, 6708–6711 (2005).
15. Xia, X. *et al.* High-Quality Metal Oxide Core/Shell Nanowire Arrays on Conductive Substrates for Electrochemical Energy Storage. *ACS Nano* **6**, 5531–5538 (2012).
16. Dupont, L. *et al.* Mesoporous Cr2O3 as negative electrode in lithium batteries: TEM study of the texture effect on the polymeric layer formation. *J. Power Sources*, **175**, 502–509, (2008).
17. Nam, K. T. *et al.* Virus-Enabled Synthesis and Assembly of Nanowires for Lithium Ion Battery Electrodes. *Science*, **312**, 885–888 (2006).

18. Wu, H., Xu, M., Wang, Y. & Zheng, G. Branched Co3O4/Fe2O3 nanowires as high capacity lithium-ion battery anodes. *Nano Res*, **6**, 167–173, (2013).
19. Moncada, A. *et al.* High-performance of PbO2 nanowire electrodes for lead-acid battery. *J Power Sources* **256**, 72–79 (2014).
20. Lei, D. *et al.* α-Fe2O3 nanowall arrays: hydrothermal preparation, growth mechanism and excellent rate performances for lithium ion batteries. *Nanoscale* **4**, 3422 (2012).
21. Bhardwaj, M. *et al.* CuCo 2 O 4 nanowall morphology as Li-ion battery anode: Enhancing electrochemical performance through stoichiometry control. *Mater Res Bull* **90**, 303–310 (2017).
22. Li, X. *et al.* Vertically aligned polyaniline nanowire arrays for lithium-ion battery. *Colloid Polym Sci* **296**, 1395–1400 (2018).
23. Yang, L. *et al.* Hierarchical MoS 2 /Polyaniline Nanowires with Excellent Electrochemical Performance for Lithium-Ion Batteries. *Advanced Materials* **25**, 1180–1184 (2013).
24. Arzac, A., Leal, G. P., Fajgar, R. & Tomovska, R. Comparison of the Emulsion Mixing and In Situ Polymerization Techniques for Synthesis of Water-Borne Reduced Graphene Oxide/Polymer Composites: Advantages and Drawbacks. *Particle & Particle Systems Characterization* **31**, 143–151 (2014).
25. Dikin, D. A. *et al.* Preparation and characterization of graphene oxide paper. *Nature* **448**, 457–460 (2007).
26. Yoo, B. M., Shin, H. J., Yoon, H. W. & Park, H. B. Graphene and graphene oxide and their uses in barrier polymers. *J Appl Polym Sci* **131**, 39628 (2014).
27. Paredes, J. I., Villar-Rodil, S., Martínez-Alonso, A. & Tascón, J. M. D. Graphene Oxide Dispersions in Organic Solvents. *Langmuir* **24**, 10560–10564 (2008).
28. Qian, Z. S. *et al.* A universal fluorescence sensing strategy based on biocompatible graphene quantum dots and graphene oxide for the detection of DNA. *Nanoscale* **6**, 5671–5674 (2014).
29. Konios, D., Stylianakis, M. M., Stratakis, E. & Kymakis, E. Dispersion behaviour of graphene oxide and reduced graphene oxide. *J Colloid Interface Sci* **430**, 108–112 (2014).
30. Liu, Y., Li, Q., Ma, K., Yang, G. & Wang, C. Graphene Oxide Wrapped CuV 2 O 6 Nanobelts as High-Capacity and Long-Life Cathode Materials of Aqueous Zinc-Ion Batteries. *ACS Nano* **13**, 12081–12089 (2019).
31. Cao, Y. *et al.* Lithium vanadate nanowires@reduced graphene oxide nanocomposites on titanium foil with super high capacities for lithium-ion batteries. *J. Colloid Interface Sci*, **498,** 210–216 (2017).
32. Liu, Z. *et al.* Carbon-coated Si nanoparticles/reduced graphene oxide multilayer anchored to nanostructured current collector as lithium-ion battery anode. *Appl Surf Sci* **396**, 41–47 (2017).
33. Zhao, C., Gao, H., Chen, C. & Wu, H. Reduction of graphene oxide in Li-ion batteries. *J Mater Chem A Mater* **3**, 18360–18364 (2015).
34. Qiu, J. *et al.* Photocatalytic Synthesis of TiO 2 and Reduced Graphene Oxide Nanocomposite for Lithium Ion Battery. *ACS Appl Mater Interfaces* **4**, 3636–3642 (2012).

35. Bernards, D. A. & Desai, T. A. Nanoscale porosity in polymer films: fabrication and therapeutic applications. *Soft Matter* **6**, 1621 (2010).
36. Agag, T., Koga, T. & Takeichi, T. Studies on thermal and mechanical properties of polyimide-clay nanocomposites. *Polymer*, **42**, 3399–3408 (2001).
37. Ogieglo, W., Wormeester, H., Eichhorn, K. J., Wessling, M. & Benes, N. E. In situ ellipsometry studies on swelling of thin polymer films: A review. *Prog Polym Sci* **42**, 42–78 (2015).
38. Niu, Y. *et al.* Catalytic and enhanced effects of silicon carbide nanoparticles on carbonization and graphitization of polyimide films. *RSC Adv.* **4**, 42569–42576 (2014).
39. Kato, T., Yamada, Y., Nishikawa, Y., Ishikawa, H. & Sato, S. Carbonization mechanisms of polyimide: Methodology to analyze carbon materials with nitrogen, oxygen, pentagons, and heptagons. *Carbon*, **178**, 58–80 (2021).
40. Inagaki, M. *et al.* Carbonization of polyimide film "Kapton". *Carbon*, **27**, 253–257 (1989).
41. Sircar, S. Basic research needs for design of adsorptive gas separation processes. *Ind Eng Chem Res* **45**, 5435–5448 (2006).
42. Jordan, T., Wang, Y. & Spiro, T. G. *Comment on 'Vibrational Assignments of Trans-N-Methylacetamide and Some of Its Deuterated Isotopomers from Band Decomposition of IR, Visible, and Resonance Raman Spectra'. J. Phys. Chem. A*, **101** (1997).
43. Yang, Y. *et al.* Preparation of Nanoscrolls by Rolling up Graphene Oxide–Polydopamine–Au Sheets using Lyophilization Method. *Chem Asian J* **11**, 1821–1827 (2016).
44. Wang, J., Jin, X., Wu, H. & Guo, S. Polyimide reinforced with hybrid graphene oxide @ carbon nanotube: Toward high strength, toughness, electrical conductivity. *Carbon*, **123**, 502–513 (2017).
45. Xiao, M. *et al.* The effect of doping graphene oxide on the structure and property of polyimide-based graphite fibre. *RSC Adv* **7**, 56602–56610 (2017).
46. Wang, D., Yu, J., Duan, G., Liu, K. & Hou, H. Electrospun polyimide nonwovens with enhanced mechanical and thermal properties by addition of trace plasticizer. *J. Mater. Sci*, **55**, 5667–5679 (2020).
47. Jeong, K.-M. *et al.* Effects of crosslinking agents on the physical properties of polyimide/amino-functionalized graphene oxide hybrid films. *Polym Int* **67**, 588–597 (2018).
48. Peng, H. *et al.* Formation of nitrogen-doped holey carbon nanosheets via self-generated template assisted carbonization of polyimide nanoflowers for supercapacitor. *J Power Sources* **482**, 228993 (2021).
49. Kotov, N. A., Dékány, I. & Fendler, J. H. Ultrathin graphite oxide-polyelectrolyte composites prepared by self-assembly: Transition between conductive and non-conductive states. *Advanced Materials* **8**, 637–641 (1996).
50. Liu, X. Y. *et al.* Preparation of a carbon-based solid acid catalyst by sulfonating activated carbon in a chemical reduction process. *Molecules*, **15**, 7188–7196 (2010).

51. Villagómez-Salas, S., Manikandan, P., Acuña Guzmán, S. F. & Pol, V. G. Amorphous Carbon Chips Li-Ion Battery Anodes Produced through Polyethylene Waste Upcycling. *ACS Omega* **3**, 17520–17527 (2018).
52. Schwan, J., Ulrich, S., Batori, V., Ehrhardt, H. & Silva, S. R. P. Raman spectroscopy on amorphous carbon films. *J.Appl.Phys* , **80**, 440–447 (1996).
53. Björkman, Å. Thermische Klärschlammbehandlung. *Schweizerische Zeitschrift für Hydrologie*, **31**, 632–645 (1969).
54. Bai, M. *et al.* NaCl and oxalic acid–assisted solvothermal exfoliation of edge-oxidized graphite to produce organic graphene dispersion for transparent conductive film application. *Journal of Nanoparticle Research* **21**, 145 (2019).
55. Blyth, R. I. R. *et al.* XPS studies of graphite electrode materials for lithium ion batteries. *Appl. Surf. Sci*, **167**, 99–106 (2000).
56. Yamaguchi, S. *et al.* Nitrogen Dissociation via Reaction with Lithium Alloys. *ACS Omega* **2**, 1081–1088 (2017).
57. Zhao, Y. *et al.* Boron and nitrogen double-doped carbon flower prepared by in-situ copolymerization as anode materials for lithium-ion batteries. *J Appl Polym Sci* **140**, (2023).
58. Hummers, W. S. & Offeman, R. E. Preparation of Graphitic Oxide. *J Am Chem Soc* **80**, 1339–1339 (1958).
59. Morimoto, N. *et al.* Real-Time, in Situ Monitoring of the Oxidation of Graphite: Lessons Learned. *Chemistry of Materials* **29**, 2150–2156 (2017).
60. Gor, G. Yu., Thommes, M., Cychosz, K. A. & Neimark, A. V. Quenched solid density functional theory method for characterization of mesoporous carbons by nitrogen adsorption. *Carbon*, **50**, 1583–1590 (2012).
61. Kupgan, G., Liyana-Arachchi, T. P. & Colina, C. M. NLDFT Pore Size Distribution in Amorphous Microporous Materials. *Langmuir* **33**, 11138–11145 (2017).
62. Xu, Z. *et al.* Nitrogen-Doped Porous Carbon Superstructures Derived from Hierarchical Assembly of Polyimide Nanosheets. *Advanced Materials* **28**, 1981–1987 (2016).
63. Campéon, B. D. L. *et al.* Non-destructive, uniform, and scalable electrochemical functionalization and exfoliation of graphite. *Carbon*, **158**, 356–363 (2020).

CHAPTER 6

CONCLUSION AND FUTURE PROSPECTS

Finally, this thesis reports my research during my PhD course at Okayama University. The purpose of this research was to develop 2D material for the fabrication and application of PI composites. In order to design the research in an original way, we referred to many scientific literatures related to 2D materials with PI composites and summarized them briefly in the introductory chapter of this thesis.

Several challenges hindering the application development of 2D materials with PI composite were identified. Cost, Toxicity, Reliability, Expandability.

In the following section, several research projects are reported to solve the above problems.

1. The ratio of complex 2D material to enhance the mechanical properties of PI composite films.
2. Optimization of the total amount of functional groups of 2D materials to improve the mechanical properties of PI composite films.
3. Expanding PI composites to the anode of LIBs by simple and rapid fabrication of 3D nanocarbon frameworks.

The first project (Fig. 1) presented in chapter 2, demonstrating a method for optimizing the proportions of multiple 2D materials, effectively enhancing the mechanical properties of polyimide (PI) composite films. Typically, PI composite films are reinforced using a single type of two-dimensional material to improve their physical characteristics. However, relying solely on a single type of two-dimensional material gradually falls short of meeting commercial demands for enhanced physical properties. To overcome this limitation, we utilized graphene oxide (GO) and hexagonal boron nitride (h-BN) and calculated the optimal ratio based on their interactions, considering factors such as shape, size, and thickness. Practical experiments confirmed the reliability and scalability of this approach.

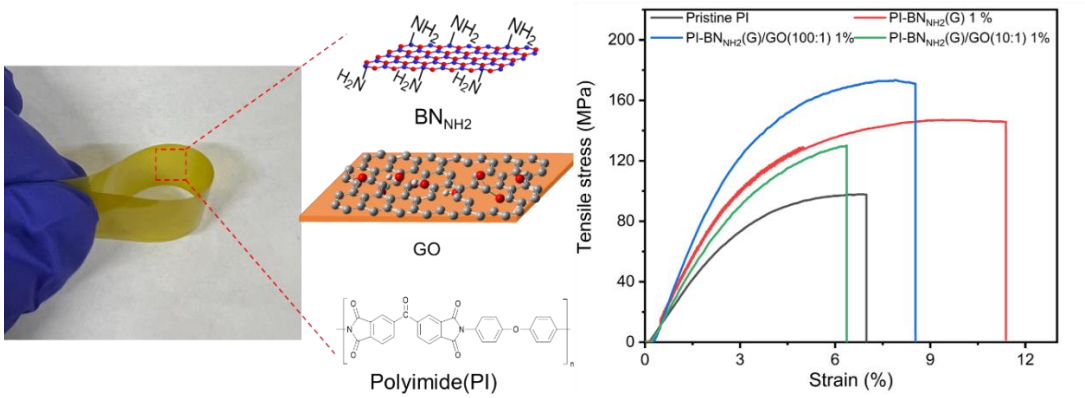

Fig. 1 The first project: Synergic effect of multiple 2D materials on the mechanical properties of polyimide composite films

The second project (Fig. 2) presented in chapter 4 illustrates the effective control of the total surface functional groups of two-dimensional materials, enabling precise control of the physical properties of PI composite films. Many studies have chemically modified two-dimensional materials and blended them with PI to enhance the physical properties of composite films. However, the influence of the total functional groups on the physical properties of PI composite films has not been thoroughly explored. This research effectively controlled the total surface functional groups of h-BN using a ball-milling method, extending the controllable application of PI composite films in terms of mechanical properties.

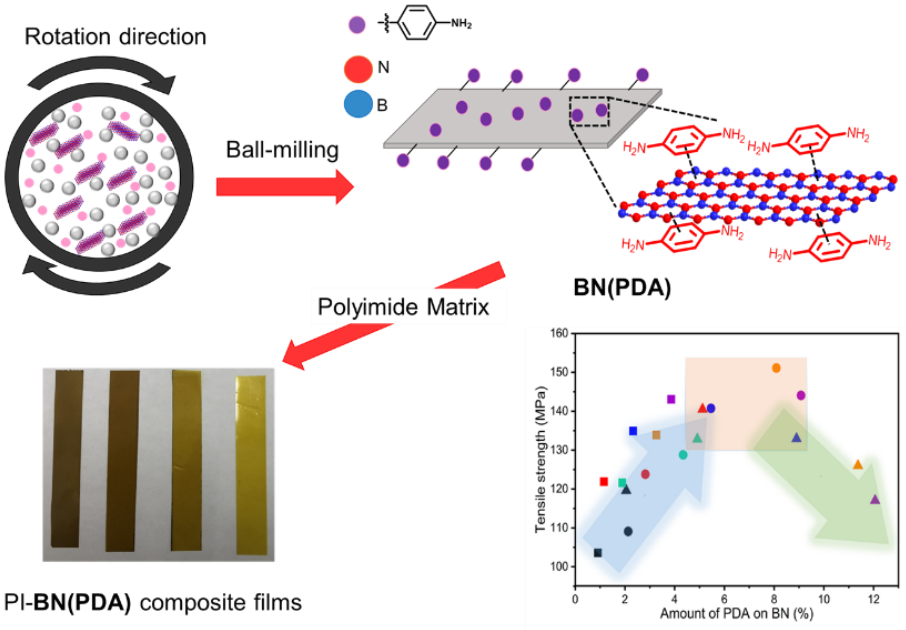

Fig. 2 The second project: Effect of the total amount of functional groups of boron nitride on the mechanical properties of polyimide composite film

The third project (Fig. 3) presented in chapter 5 we designed a simple and fast method to prepare three-dimensional (3D) nanocarbon materials. Previous studies have shown that fabricating 3D carbon materials is cumbersome, expensive, and limited in quantity. In this study, we devised a straightforward approach to create PI nanowall structures on the GO surface and then heated to produce 3D nanocarbon structures. The results demonstrated that the 3D nanocarbon materials prepared using this method exhibit excellent performance in LIBs.

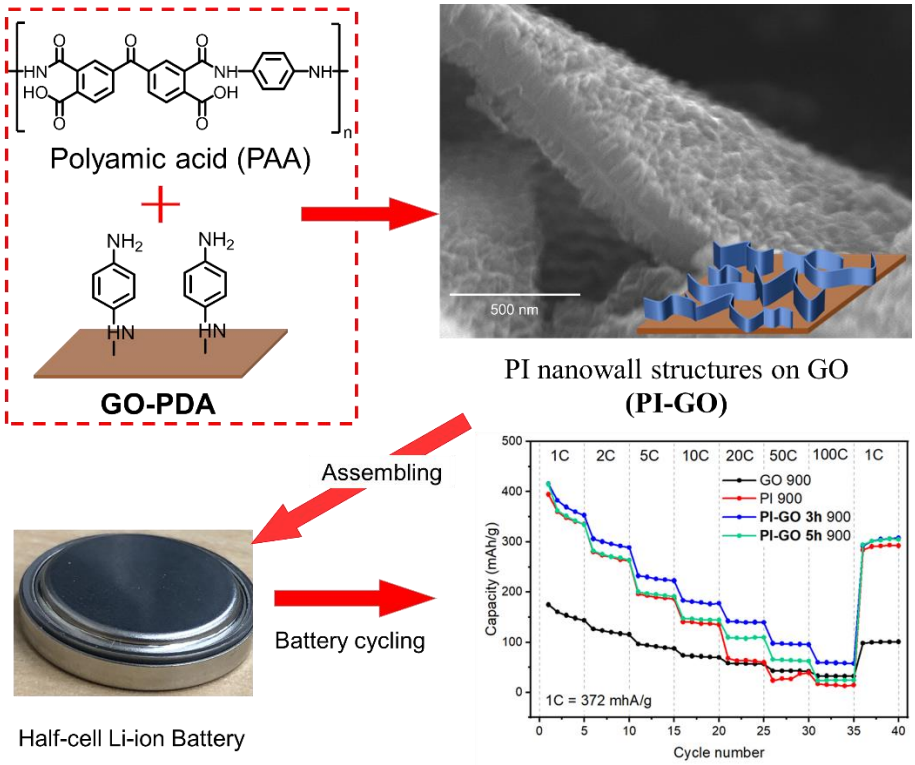

Fig. 3 The third project: 3D carbon nanostructure development and LIBs performance investigation.

From the discussion above, it is evident that the primary advantage of 2D materials lies in their ability to effectively enhance the physical properties and patterns of PI composite materials through various preparation methods. To achieve the expansion and controllability of PI composite applications, it is essential to understand the activity and structure of 2D material, requiring more precise calculations and theoretical analyses. I hope that the above research projects will be helpful for the development of 2D materials and PI composites applications.

LIST OF PUBLICATIONS

(1) Synergic effect of graphene oxide and boron nitride on the mechanical properties of polyimide composite films

Yi Kai Cheng, Benoît Denis Louis Campéon, Seiji Obata, and Yuta Nishina

Nanoscale Adv., 2022, **4**, 2339

(2) Ball mill enhances the functionalization of boron nitride: The application for polyimide fillers

Yi Kai Cheng, Seiji Obata, and Yuta Nishina

FlatChem, 2023, **39**, 100489

(3) Vertically grown carbon nanowalls on graphene oxide: synthesis and Li-ion battery application

Yi Kai Cheng, Seiji Obata, and Yuta Nishina

ACS Applied Materials & Interfaces, **submitted**

ACKNOWLEDGEMENTS

In my PhD research I am very grateful to Prof. Yuta Nishina for giving me a lot of freedom in my research, and for teaching me how to design my research from a chemical and materials perspective, and then step by step to explore the application aspects. Without Prof. Nishina's help, I would not be where I am now.

I would like to thank Associate Professor Seiji Obata for his continuous guidance on the principles of measurement equipment and the purpose of research during my PhD program. This has enabled me to understand more about materials and research.

I would also like to thank Prof. Mitsuhiro Okayasu for guiding me in the proper use of tensile testing of thin film materials and theoretical knowledge.

I would also like to thank Dr. Benoît Denis Louis Campéon for teaching me about the polyimide process and many other aspects of carbon materials research.

I would like to thank the jurors for taking the time to review my research and for the interesting comments they made during the defense.

I would also like to thank the members of the lab for making the lab feel like another safe haven. Dr Matusmura, Dr kommada, Dr Pilar, Dr Isra, Tamagawa, Dr Zhou, Dr nagakawa, Dr, Takahashi, Dr Zou, Mr Hiramatus , Mr Okura, Mr Ishihara, Kimura, Shimada, Komoda, Akada, Dr Shiba, Dr Razu, Takada, Asanama, Mr Yamama, Nagano, Maram, Nusrat, Kubo, Iguchi, Shibahara.

Lastly, I would like to thank my family for their full support so that I could come to Japan to study for my PhD without any worries. I hope that my brother in Taiwan will also be able to complete your PhD degree successfully.